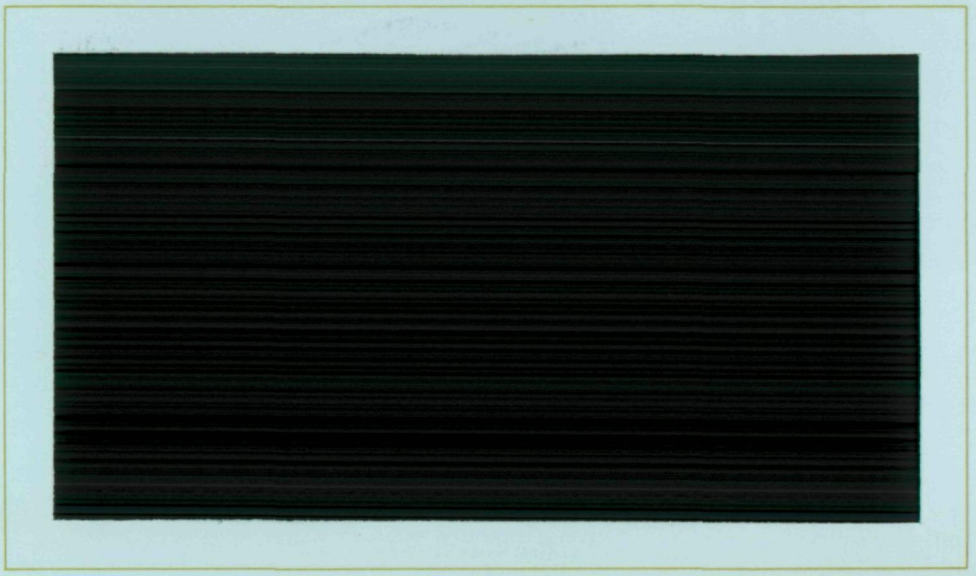

EARTH ENERGY EXPERIMENT (E^3) PROJECT

NASA CONTRACT NAS 1-11871

drexel university

DEPARTMENT OF PHYSICS
AND ATMOSPHERIC SCIENCE

NASA CR - 145129

TECHNIQUES FOR OBTAINING REGIONAL RADIATION BUDGETS FROM SATELLITE RADIOMETER OBSERVATIONS

By José F. Pina and
Frederick B. House

Final Report
Phase IV and Phase V

Prepared under Contract No. NAS1-11871 by
Department of Physics and Atmospheric Science
Drexel University
Philadelphia, Pennsylvania 19104

for

NATIONAL AERONAUTICS AND SPACE ADMINISTRATION

December, 1976

NASA

PREFACE

The present report contains results of an investigation of critical problems related to the interpretation of observations by satellite radiometers for the purpose of monitoring the long-term earth energy budget (EEB). This work was performed under Langley Research Center Contract No. NAS1-11871 for the National Aeronautics and Space Administration.

This research study, performed by Drexel University, is one part of a much larger effort by several institutions, including Colorado State University, The University of Wisconsin, Virginia Polytechnic Institute and State University, Link Temco Vought, National Oceanic and Atmospheric Administration, NASA Goddard Space Flight Center, as well as cognizant personnel at NASA Langley Research Center. This team is studying the Earth Radiation Budget Satellite System (ERBSS) for performing long-term measurements over geographical regions, zonal belts, hemispheres, and the entire earth for periods of 10 to 30 years.

This document is the Ph.D. dissertation of Dr. José F. Pina who has been associated with the ERBSS problem for several years at Drexel University. His thesis concerns the development of techniques for obtaining regional radiation budgets from observation by wide-angle, broad-band radiometers on satellites.

The current investigation was performed during the twenty one month period 1 January 1975 through 30 September 1976. This period includes Phase IV and a portion of Phase V efforts of the subject contract above. The expressed purpose of these efforts are outlined in the statements of work as follows:

Phase IV Effort

1. Determine potential methods of inverting wide-field of view observations to enhance the spatial resolution of the measurements.

2. Develop quantitative criteria for determining accuracy of data retrived by methods in (1).

3. Develop a computer program for dividing a spherical earth into area increments that is adequate for determining matrix elements, required by all inversion methods in (1).

4. Conduct a study to determine the optimum method of inverting EEB observations, using criteria in (2) and matrices in (3).

5. Incorporate a limb-darkening model in the inversion method (4) for optimal estimation of radiant emittance distributions of the earth-atmospheric system.

6. Incorporate a bi-directional reflectance model in the inversion method (4) for optimal estimation of albedo distribution of the earth-atmospheric system.

Phase V Effort

4. Extend the analysis of the matrix inversion technique to include the inverting of wide-field of view, shortwave radiation measurements to enhance their spatial resolution over a spherical earth.

The bulk of the thesis addresses the six items in the Phase IV effort. Chapter 5 specifically concerns Item 4 of the Phase V effort.

Other reports under this Contract that are related to the overall ERBSS effort are: "An Investigation of ESSA VII Radiation Data for Use in Long-term Earth Energy Experiments," published as NASA CR-132623; "Our Contaminated Atmosphere - The Danger of Climate Change," published as NASA CR-132625; "Steady-state Solution to the Conduction Problem of a Spherical Balloon Radiometers," published as NASA CR-132624, and "Techniques for Computing Regional Radiant Emittances of the Earth - Atmosphere System from Observations by Wide-angle Satellite Radiometers," published as NASA CR-145011.

Gratitude is extended to several NASA/LaRC personnel for their encouragement, interest, stimulating discussions and suggestions provided during the present investigation. Among these scientific personnel are included: Messrs. Jack Cooper (Technical monitor), Charles Woerner, George Sweet, Bill Weaver, Dr. Louis Smith who served on Dr. Pina's Thesis and Defense Committees and other members of the LaRC team.

Frederick B. House, Project Director
Associate Professor of Physics and
Atmospheric Science

Techniques for Obtaining Regional Radiation Budgets from Satellite Radiometer Observations

A Thesis

Submitted to the Faculty

of

Drexel University

by

José Fermín Pina

in partial fulfillment of the

requirements for the degree

of

Doctor of Philosophy

June 1977

ACKNOWLEDGEMENTS

I would like to express my gratitude to NASA/Langley Research Center for the financial support provided to accomplish this investigation. I am grateful to the faculty of the Department of Physics and Atmospheric Science at Drexel University and to the chairman, Dr. William W. Eidson, for their guidance during my graduate studies. I am indebted to Dr. Frederick B. House who posed the problem undertaken in this research and who diligently questioned all the assumptions and fundamental ideas included in the techniques developed. I would like to thank Dr. Teck-Kah Lim and Dr. G. Louis Smith for allowing me the use of their computer programs for determining matrix eigenvalues. I wish also to express my gratitude to Dr. G. L. Smith, and Messrs. G. E. Sweet, C. V. Woerner, R. A. Babcock, J. E. Cooper, G. R. Young, and W. L. Weaver of NASA/Langley Research Center for enlightening discussions of several subjects related to this investigation. My thanks also go to Messrs. W. B. Huston and H. V. Soule of OAO Corporation for drawing the figure in Appendix A. I am grateful to Mrs. Nelda D. Payton, Miss Bonnie S. Zibulsky, and Miss Josephine Hayes for their cooperation in the typing of the draft of this thesis. Finally, I am most grateful to my wife, Madeline, for the invaluable discussions, moral support, and helpful suggestions which she provided while working on her own Ph.D. dissertation.

TABLE OF CONTENTS

LIST OF TABLES

LIST OF ILLUSTRATIONS

ABSTRACT

TECHNIQUES FOR OBTAINING REGIONAL RADIATION BUDGETS FROM SATELLITE RADIOMETER OBSERVATIONS

AUTHOR: José Fermín Pina

SUPERVISOR: Frederick B. House

(Associate Professor)

Two methods have been developed for obtaining regional radiation budgets from wide field of view satellite radiometer measurements. The two fundamental assumptions of these methods are: (a) the earth-atmosphere system can be divided into regions having homogeneous emitting and reflecting characteristics; (b) the angular functions which describe the emitted longwave and reflected shortwave radiation fields are available from previous or simultaneous observations.

In order to carry out the numerical integrations required in the two techniques, a scheme was developed which divides the earth-atmosphere system into 2060 elemental areas. The regions previously described are then defined in terms of these elemental areas which are fixed in size and position as the satellite moves.

One of the methods, termed the instantaneous technique, yields values of the radiant emittance (We) and the radiant reflectance (Wr)

which the regions have during the time interval of a single satellite pass. In this technique, the number of observations matches the number of regions under study and a unique solution is obtained using matrix inversion. The other method (termed the best fit technique), yields time averages of We and Wr for large time intervals (e.g., months, seasons). The number of observations in this technique is much greater than the number of regions considered, and an approximate solution is obtained by the method of least squares.

The inverse matrix obtained in the instantaneous technique is in general unstable due to insufficient coverage of all regions studied by the field of view of the radiometer. This instability results in large magnification of Gaussian instrumental errors. A matrix stabilization technique was developed which diminished the errors in the result by about a factor of ten in several cases. Furthermore, a prediction scheme based solely on the structure of the configuration factor matrix was developed which successfully predicts the regions that will have acceptable results. The average values of We and Wr obtained with the best fit technique were found acceptable for all regions.

Both of the techniques developed isolate in space the problem of determining the regional values of We and Wr, that is, only data derived from the regions themselves are used in the determinations of these quantities. Furthermore, application of these techniques is independent of the ellipticity of the satellite orbit.

Even though the instantaneous technique presupposes that the regions observed have fairly homogeneous emitting and reflecting

characteristics, several cases where a region was split into two subregions with different We values were successfully handled without taking the extra power measurement required for matching the new number of regions. Furthermore, an evaluation parameter was derived which indicates those cases when the split region has too large a difference between the We values of its two subregions. In these cases, the extra observation required to match the new number of regions must be included in order to obtain an accurate solution.

CHAPTER I. INTRODUCTION

Motivation

The imbalance between the solar radiation absorbed and the terrestrial radiation emitted by different regions of the earth-atmosphere (E-A) system constitutes the thermal driving force primarily responsible for the atmospheric and oceanic circulations. The spatial variation of this imbalance is also responsible for zonal and regional climates.

The radiation imbalance of a region can be expressed in terms of the quantity Q known as the net radiation or radiation balance. It is defined as the difference between the radiation absorbed and emitted by a region at the top of the atmosphere. Mathematically, it is defined as

$$Q = Hs(1-A) - We \tag{1-1}$$

where Hs is the irradiance due to direct (incoming) solar energy, A is the albedo which represents the fraction of Hs that is reflected, and We is the radiant emittance due to terrestrial radiation. By using the radiant reflectance $Wr = AHs$ which represents the amount of Hs reflected, Eq.(1-1) is written in terms of the fluxes Hs, Wr, and We, as

$$Q = Hs - Wr - We \tag{1-2}$$

or

$$Q = H_o \cos \zeta - Wr - We \tag{1-3}$$

where H_o is the solar irradiance for zero solar zenith angle, and ζ is the solar zenith angle.

The gradient of Q is the primary cause for the existing climate zones and energy transports described above. Observations indicate that the magnitude of Q averaged over all longitudes and seasons is positive in the equatorial regions, negative in the polar regions, and zero at approximately lat 40^{o} of either hemisphere. Regional variations of Q within given latitudinal zones can also be significant, especially in the tropical zones. The possible relationship of these variations to meteorological phenomena is of practical importance.

The power intercepted by a satellite radiometer due to emitted long-wave radiation (LWR) and reflected short-wave radiation (SWR) are denoted by Pe and Pr, respectively. The reflected SWR lies in the spectral interval between 0.2 and 5μ, while the emitted LWR is between 5 and 100μ (Kondratyev, 1969). The radiometers are able to discriminate between these two types of radiation by the use of special coatings and/or filters. Interpretation of these radiometer data constitutes the fundamental problem in obtaining the fluxes We and Wr.

It is essentially this problem of data interpretation which was pursued in this investigation and techniques for determining regional values of We and Wr were developed. From these values, Q can be calculated by using Eq.(1-2), once Hs has been determined.

There is not much difficulty in determining the value of Hs of a region. This is easily calculated from the following equation.

$$Hs = H_o \overline{\cos \zeta} \tag{1-4}$$

where $\overline{\cos \zeta}$ is the weighted average of cos ζ within the given region, and H_o is the solar irradiance at the satellite. It is preferable

to measure H_o as often as needed rather than to treat the solar constant as actually being a constant. It is clear then that the value of Hs in Eq.(1-2) is easily obtained and hence, it is unnecessary to develop a computational technique in this thesis for determining this quantity.

The determination of We in Eq.(1-2) however, is more problematic than that of Hs. The angular dependence of the radiation emitted by a region must be known in order to deduce the value of We from observations of that region by satellite radiometers. One way of determining this angular dependence is to measure the radiance N simultaneously from every possible direction in space. From a practical point of view, this is an impossible task. An alternative approach to this problem is to describe the angular distribution of N with an angular function previously obtained or determined simultaneously with a scanning narrow field of view (NFOV) radiometer.

The determination of the reflected SWR flux in Eq.(1-2) poses an even more complex problem than that of We. One has to contend here with two angular dependences: that due to the sun's position and that due to the satellite's position.

The angular distribution of the radiance Nr (of the reflected SWR) of a region must be known for each position of the sun for which an observation is made. The value of Wr for each of these sun positions can then be calculated. However, measuring Nr from all possible angles for each position of the sun is an insurmountable observational problem. Nevertheless, as in the case of We, an alternative approach is to use an angular model based on previous observations or on measurements made simultaneously with scanning, narrow FOV radiometers.

In the past, techniques for computing We and Wr have been obtained by making simplifying assumptions concerning the characteristics of the radiation field. The area within the field of view (FOV) has been assumed to emit LWR isotropically, and to reflect the solar SWR diffusively. In addition, both radiation fields We and Wr have been assumed to be homogeneous throughout the FOV. The method by which these homogeneous values of We and Wr have been calculated in the past will be illustrated for the case of LWR.

The isotropic radiance N^{iso} is related to the corresponding value of We by

$$We = \pi N^{iso} \tag{1-5}$$

The power Pe intercepted by a horizontal flat plate radiometer (of unit cross-sectional area) due to LWR emitted by the E-A system is given by

$$Pe = \int_0^{2\pi} d\psi \int_0^{\alpha_{max}} N'(\alpha,\psi') \sin\alpha \cos\alpha \, d\alpha \tag{1-6}$$

where α and ψ' are the nadir and azimuthal angles, respectively, N' is the radiance when expressed in terms of α and ψ', and α_{max} is the maximum value that α can attain. For the case of a spherical radiometer, the cos α factor reduces to one. By the assumptions made above, N' is isotropic and homogeneous over the entire FOV and hence, independent of α and ψ'. Then, Eq.(1-6) results in

$$Pe = \pi N^{iso} \sin^2 \alpha_{max} = We \sin^2 \alpha_{max} \tag{1-7}$$

Similarly, Pr is given by

$$Pr = Wr \sin^2 \alpha_{max} \tag{1-8}$$

Although the above values of We and Wr are assumed to be the same for all points within the FOV, researchers assigned them only to the subsatellite points (SSP). Subsequently, maps of We and Wr were constructed by joining with isopleths those points having equal values. Similarly, the solar irradiance Hs is assumed to be the same throughout the FOV and equal to the weighted average of the actual values of Hs throughout the FOV. This average value is then assigned only to the SSP as in the case of We and Wr. Then, the Q value of each SSP is computed from the corresponding values of Hs, Wr, and We. Maps of Q have also been constructed by joining with isopleths points having equal values of Q.

The above procedure leads to inaccuracies in the determination of regional values of Q. Two main difficulties have been pointed out: (a) the value of Q of a given region is determined by including the radiation contributed by neighboring regions, (b) the angular distribution of N and Nr are completely neglected.

Considerable effort has been directed for some time at finding improved methods for determining the individual radiation budgets of regions observed by wide field of view (WFOV) radiometers. The emitting and reflecting characteristics of adjacent regions may be significantly different due to variations in topography, temperature, and cloud coverage. It is almost impossible to view only one region totally while excluding all others during a single observation. Hence, practically all observations by WFOV radiometers include several portions of regions that may have significantly different Q values. Therefore, it is important to develop techniques which yield the flux values of We

and Wr for the different homogeneous regions within the FOV. Then, the corresponding Q values of these regions can be easily calculated by use of Eq.(1-2).

The need for the types of techniques just described provided the main motivation for undertaking the present investigation during which two such techniques were developed. These two techniques provide a more accurate solution to the problem of determining the regional fluxes We and Wr.

Outline of problem solution and results

This section presents an outline of the methods developed for obtaining regional radiation budgets from WFOV radiometer measurements. These methods include: (a) a technique for determining the instantaneous values of We and Wr, (b) a best fit technique for obtaining time averages of these fluxes. In addition, a matrix stabilization scheme and a data quality prediction technique were developed in order to supplement the instantaneous technique.

The instantaneous and best fit techniques will be described while applying them to the case of determining the flux We.

Eq.(1-6) gives the LWR power Pe that a horizontal flat plate radiometer intercepts. This equation is solved numerically by dividing the E-A system into a finite number of elemental areas. Each region of the E-A system having approximately homogeneous emitting and reflecting characteristics is defined in terms of these elemental areas. Then, by adding up the power increments contributed by those elemental areas of a region k which are within the FOV of the jth observation, the power P_{jk} is obtained. This is the power contributed by the kth region to the jth observation. Then, the total power P_j intercepted by the jth observation is the sum of the contributions of all the K regions within the FOV, that is,

$$P_j = \sum_{k=1}^{K} P_{jk} \tag{1-9}$$

which is the power represented by Pe in Eq. (1-6).

The power P_{jk} contributed by the kth region can be represented by $F_{jk}\ We_k$ where F_{jk} is the configuration factor of the kth region

and jth observation, and We_k is the value that We has in the kth region. Then, Eq.(1-9) results in

$$P_j = \sum_{k=1}^{K} F_{jk} \, We_k \tag{1-10}$$

The configuration factor F_{jk} represents the fraction of the LWR flux emitted by the kth region which is intercepted by the radiometer in the jth observation. This factor includes any function used to describe the angular distribution of N, such as a limb darkening function (LDF). In this investigation, a LDF model and an isotropic radiation model were used.

There is an Eq.(1-10) for each observation made of the K regions under study, and the essential difference between the two techniques developed lies in the number of observations or equations used to solve the problem.

In the instantaneous technique, the number of observations J matches the number of regions K investigated and a unique solution is obtained. In the best fit technique J>>K, that is, the system is overdetermined and an approximate solution is found by the method of least squares.

The results that the instantaneous technique yield are obtained from data collected during a single pass of the satellite. This is the reason for naming this technique instantaneous. The results of the best fit technique are time averages obtained from data collected during many satellite passes.

There are J=K equations of the form of Eq.(1-10) in the instantaneous technique. These equations can be written in matrix form as

$$F \{We\} = \{P\} \tag{1-11}$$

where F is the K x K configuration factor matrix of elements F_{jk}, and {We} and {P} are the column matrices made up of the We and P values.

By inverting F and operating with the resulting inverse matrix F^{-1} on {P} one obtains {We'}, that is,

$$F^{-1}\{P\} = \{We'\} \tag{1-12}$$

If there are no instrumental errors included in the power measurements P (that is, if the P values are exact),{We'} = {We} and the problem has been solved. Unfortunately, the situation is not this simple;the powers P' usually include systematic as well as Gaussian random uncertainties δP. Furthermore, in general the satellite positions are such that insufficiently large portions of all regions are observed. The latter causes F^{-1} to be unstable and the random errors δP appearing in the power measurements $P' = P + \delta P$ are in some cases highly magnified making some of the results entirely unreliable.

It was possible, however, to develop a technique for stabilizing the inverse matrix F^{-1}. This technique consists in removing the smallest elements of the original ill-conditioned matrix F and adding them to the diagonal elements in the corresponding rows. This technique renders well-conditioned the original matrix F. Magnification of the δP errors was dramatically reduced. Nevertheless, as explained previously, since sufficiently large sections of some of the regions were not observed, the solutions for these regions still contained significant errors.

It became necessary to develop a technique based solely on the structure of the new well-conditioned configuration factor matrix

F_{wc} to predict which regions would have reliable data and which would not. Each column of the matrix F_{wc} corresponds to a different region. The ratio of the diagonal element of each column of F_{wc} to the average shape factor of the total FOV is multiplied by the sum of the elements in the corresponding column. The result is a prediction parameter that should be greater than a predetermined value in order for the data of the corresponding region to be acceptable. Otherwise, the solution for the region is considered unreliable.

By selecting a set of satellite positions such that their FOV's include sufficiently large portions of all regions under study, it was shown that even when the powers include instrumental errors, all of the results are acceptable. Hence, under these circumstances, there is no need to apply either the matrix stabilization technique or the data quality prediction technique.

As stated previously, in the best fit technique the number of observations J is much greater than the number of regions K, resulting in J equations of the form of Eq.(1-10), and hence the system can be considered overdetermined. The method of least squares is used to find an approximate solution. The results obtained with this technique represent time averages of the We values existing during the time interval (e.g., month, season) that the measurements were taken. All of the results obtained with this technique are found acceptable even when changes of scene (i.e., changes of the regional values of We) are introduced after each satellite pass.

Application of the instantaneous and best fit techniques to the case of reflected SWR is slightly more complex than that of the

emitted LWR. The reason is that the radiance N in the LWR case depends on the angular position of the satellite only, while the radiance Nr in the case of reflected SWR depends on the angular position of the sun as well as on the angular position of the satellite.

The definition of a region is also more complex in the case of reflected SWR than in the case of LWR. In the latter, a region is defined as an area having a uniform value of We - the radiant emittance. In the reflected SWR case, the radiant reflectance $Wr(\zeta)$ can not be used for defining a region since this quantity is dependent upon the zenith angle of the sun. This angle varies within a region due to the curvature of the earth. Nevertheless, by selecting a particular sun zenith angle ζ_o, the homogeneous reflecting characteristics of a region can be represented by a uniform value of $Wr(\zeta_o)$. Arbitrarily, the value $\zeta_o = 0$ was chosen, and a region was defined as an area having a uniform value of Wr(0). This definition is very similar to that used in the LWR case. This means that all the techniques previously applied to the case of obtaining We are also applicable to the case of obtaining Wr(0), and an equation similar to Eq.(1-10) is obtained for each observation, namely

$$P_j = \sum_{k=1}^{K} F_{jk} \, Wro_k \qquad (1\text{-}13)$$

where Wro = Wr(0) is used in order to simplify the notation.

The factor F_{jk} in Eq.(1-10) includes an angular function which depends only on the position of the satellite, while the angular function in the F_{jk} factor of Eq.(1-13) depends on the angular positions of the sun and the satellite. A bidirectional reflec-

tance model and a diffuse reflection model were used in this investigation.

The results obtained in the case of Wro with the instantaneous and best fit techniques, as well as with the stabilization and prediction techniques were almost identical to those obtained in the case of We.

Once the values of Wro were obtained, the average values of $Wr(\zeta)$ for each region are calculated from the following equation.

$$\langle Wr(\zeta)\rangle_k = Wro_k \langle R_1(\zeta) \cos \zeta \rangle_k \qquad (1\text{-}14)$$

where $\langle Wr(\zeta)\rangle_k$ is the spatial average of $Wr(\zeta)$ for the kth region, Wro_k is the value of Wro determined previously for the kth region, and the last factor is the average of $R_1(\zeta) \cos \zeta$ for the kth region. The parameter $R_1(\zeta)$ is given by

$$R_1(\zeta) = \frac{r(\zeta)}{r(0)} \qquad (1\text{-}15)$$

where $r(\zeta)$ is the directional reflectance for ζ solar zenith angle, and $r(0)$ is the value of the same function at $\zeta=0$.

Since the position of the sun affects the results in the case of $Wr(\zeta)$, then the average values of $Wr(\zeta)$ obtained with the best fit technique are dependent on the times at which the observations are made. For example, if the observations considered in the determination of the $\langle Wr(\zeta)\rangle$'s are all taken at approximately the same local time, then the results will be representative of the conditions at that local time. If on the other hand, the observations selected were made at all possible daylight local times, then the results represent an average condition for all the sun positions included.

Some of the results obtained can be summarized in terms of rms's of the δWe" and δWr" errors computed for those regions found acceptable according to the prediction technique developed. These errors are the results of systematic, Gaussian random, and combinations of both of these uncertainties. It is assumed in this discussion that the correct angular distribution function is used during data interpretation, and that the regions are fairly homogeneous as required. It was found that the rms's of the errors in the LWR case were all below 5 W/m^2, while those in the case of reflected SWR were below 7 W/m^2.

Furthermore, the instantaneous technique produces acceptable results in many cases where a region is split into two subregions of almost equal size and having different values of We. Of course, in these cases, one of the fundamental assumptions of the instantaneous technique is not met, namely, that the number of observations J must be equal to the number of regions K. This condition is required in order to have a unique solution. It was found that the values of We in the two subregions can differ by as much as $\Delta We = 10\ W/m^2$ with a resulting δWe" error below 6 W/m^2. Moreover, in two cases, the difference ΔWe between the two subregions was as much as 50 W/m^2 and the results obtained were: (a) -13.3 and 15.7 W/m^2 for the sphere and plate, respectively, in one case; (b) 18.7 and 20.0 W/m^2 for the sphere and plate, respectively, in the other case. The results in the first case are still considered acceptable (the acceptable limit is understood to be 15 W/m^2, as is explained later), while those in the second case are not. An evaluation parameter (derived for this purpose) is used to detect unacceptable

results in the instantaneous technique. These findings also apply to the case of Wr(0) for SWR flux since the treatments of We and Wr(0) are almost identical as explained later.

The results obtained with the best fit technique were all acceptable. Even those regions exhibiting the worst results had errors in the fluxes which were below 12 W/m^2 in both cases, LWR and SWR.

All of the results discussed above are presented in detail in Chapter 4 for the case of LWR, and in Chapter 5 for the SWR case.

On the basis of the excellent results obtained with the two techniques developed, it can be concluded that these techniques represent dependable methods for obtaining the instantaneous as well as time averaged values of Q for regions smaller than the FOV of low spatial resolution radiometers.

CHAPTER II. HISTORICAL BACKGROUND

The continuous evolution of satellite technology has provided the scientific community with more advanced satellite systems which are larger, more reliable, have longer life expectancies, larger power sources, as well as better data storage and telemetry systems. The radiometers on board these satellites have also become more versatile and sophisticated. In the meantime, the atmospheric scientist has been endeavoring to develop improved methods of data interpretation and to determine the effects that satellite orbits and the angular dependence of radiation may have on this data interpretation.

This chapter presents some historical developments which are pertinent to the vital problem of determining the net radiation of the E-A system. The chapter is divided into four sections: (1) satellite radiometers, (2) data interpretation, (3) optimum satellite orbits, (4) angular dependence of radiation.

Satellite radiometers

H. Wexler of the U. S. Weather Bureau (Van Allen, 1958) suggested the first experiment intended to measure the radiation budget of the E-A system from an artificial satellite. This experiment was one of four chosen for the earth satellite program of the International Geophysical Year (IGY).

Suomi (in collaboration with Parent) of the University of Wisconsin proposed the use of specially coated titanium spheres (about the size of ping pong balls) to accomplish the above task (Van Allen, 1958). Spherical sensors were selected because of their omni-directional characteristics which make the measurements independent of the orientation

of the satellite.

The net radiation of the E-A system depends on the magnitude of the three radiation fluxes Hs, Wr, and We in Eq.(1-2). These fluxes can be measured by using spherical radiation sensors attached to the radio antennas of the satellite (Suomi, 1958).

Two of the satellites of the IGY program carried instruments designed for radiation measurements (Ruttenberg, Ed., 1959). Instrumentation for observing cloud cover using an infrared detector was developed by the U. S. Army Signal Engineering and Development Laboratories, and carried on board Vanguard II (1959 Alpha), launched February 17, 1959. Explorer VII (1959 Iota), launched October 13, 1959, carried six sensors developed at the University of Wisconsin for measuring the radiation budget of the earth.

The radiometers on Explorer VII used to measure the three flux components of the radiation budget (Hs, Wr, and We) consisted of silver bolometers designed as hemispherical shells (Suomi, 1961). These hemispherical shells were mounted on insulating posts attached to plane mirrors. Such a mirror- hemisphere combination is partially equivalent to the spherical sensors originally proposed by Suomi as previously mentioned. Two of the hemispheres were painted black to absorb equally the three radiation fluxes mentioned above. A third hemisphere was coated white to make it more sensitive to LWR than to SWR. The fourth hemisphere had a gold metal coating to make it respond more to SWR than to LWR. A black sphere was used to determine deterioration of the mirror surfaces by comparison with the black hemispherical detectors. In addition, a small Tabor-coated hemisphere was protected with a shade from direct sunlight and used to measure the reflected sunlight when the

satellite's axis pointed toward the earth.

All of the radiometers described so far fall in the class known as WFOV radiometers, or as low spatial resolution (LSR) radiometers. There is essentially one significant difference between a spherical radiometer and a hemispherical one mounted on a mirror. The former, regardless of its orientation, detects radiation impinging on it from a 4π steradians solid angle, while the latter detects that radiation which would fall on a sphere only from the 2π steradians solid angle on the side of the mirror. Hence, the hemisphere-mirror combination has the advantage of not being contaminated by radiation emitted by the carrying spacecraft.

The above WFOV or LSR radiometers are of the utmost importance in the discussion of the techniques developed in the present investigation for We and Wr. These techniques were designed primarily for interpreting data gathered by WFOV radiometers in order to obtain the above fluxes. However, it should be pointed out that they are also applicable to restricted field of view (RFOV) and NFOV radiometers.

The Explorer VII radiometers were analyzed using a theoretical model developed by Littan (1961). The heating and cooling trends obtained from this model agreed satisfactorily with empirical data obtained from Explorer VII.

The TIROS I (Television and InfraRed Observation Satellite) satellite launched April 1, 1960, was the first of a new generation of satellites which initiated weather observation on a much larger scale, routinely collecting previously unavailable information (Hubert and Lehr, 1967). Some of the TIROS satellites carried radiometers to measure the fluxes of LWR and SWR as discussed below.

TIROS II was launched in November, 1960. It carried two television

cameras and two radiometers. A radiation budget measurement was conducted with the low resolution radiometer (Hanel and Wark, 1961). The other radiometer on board TIROS II was a scanning type of medium resolution. The spatial resolution of this radiometer was about a 40 mile square area centered at the nadir point. The FOV of the LSR radiometer previously mentioned was a circle, centered at the nadir point, having a diameter of approximately 450 miles (Bandeen, et al., 1961). The altitudes of TIROS II at perigee and apogee were, respectively, 385.6 and 454.5 statute miles.

As will be discussed later, data collected by TIROS II, III, IV, and VII were used by several investigators for studying the characteristics of the radiation fluxes emitted and reflected by the E-A system.

The first Nimbus satellite, launched on August 28, 1964, functioned successfully for 27 days. At this time, a failure in the mechanism that rotated its solar paddles terminated its operation (Hubert and Lehr, 1967). This satellite had on board an advanced vidicon camera system (AVCS), an automatic picture transmission (APT) camera, and a high resolution infrared radiometer (HRIR). The FOV of this radiometer is about six miles.

The Nimbus satellite's camera and radiation detectors always are directed toward the earth as the satellite travels in a retrograde orbit of about 100° inclination (Hubert and Lehr, 1967).

Nimbus II, launched May 15, 1966, provided almost continuous global observations of meteorological phenomena (Nordberg, et al., 1966). Its almost polar sun synchronous orbit had an inclination of 100.3°. This satellite had a HRIR with an angular FOV of 7.8 x 7.8 milliradians. It also carried a Medium Resolution Infrared Radiometer (MRIR) with an

angular FOV of 50 x 50 milliradians. This is equivalent to an area of approximately 60 x 60 km^2 at the satellite subpoint.

The Nimbus II satellite provided for the first time data on the emitted LWR and reflected SWR by the polar regions (Raschke, et al., 1967). Some of the analysis results of the data gathered by this satellite will be discussed later.

The Nimbus III satellite, launched April 14, 1969, included a five-channel MRIR experiment which consisted of a cross-track scanning unit of the type carried on Nimbus II. For the first time, it became possible to make estimates of the annual global radiation budget on the basis of measurements by scanning radiometers (Raschke, et al., 1973).

Nimbus III also carried the first Satellite Infrared Spectrometer (SIRS-A) with a FOV of 200-km square in order to measure the spectra of the radiances in seven spectral channels (Winston, et al., 1972).

The ESSA III, V, VII, and IX satellites carried WFOV flat plate radiometers, as well as RFOV conical shaped radiometers. One sensor of each type was coated black to absorb radiation of all wavelengths, and one of each type was coated white to absorb preferentially the LWR.

The Earth Radiation Budget (ERB) experiment on board Nimbus 6 consists of a set of 22 optical channel instruments (Smith, et al., 1975). Ten channels detect direct solar SWR; four WFOV channels look at the earth. There are eight NFOV channels that measure radiation in different spectral intervals. Four of these channels yield the angular distribution of the LWR emitted by the E-A system, and four measure the solar SWR reflected by the E-A system. The FOV of each scanning channel is approximately 500-km square (Jacobowitz, et al., 1975).

Data interpretation

Interpretation of the data collected by satellite radiometers in order to determine the fluxes emitted and reflected by the E-A system represents one of the most challenging problems in satellite radiometry. The following descriptions of methods investigated and/or used to accomplish this data interpretation illustrate the considerable effort and time invested by several investigators in this field in order to develop improved techniques.

One of the earliest techniques used for computing We and Wr from WFOV radiometer data is based on the assumption that these two radiation fields are isotropic and homogeneous throughout the FOV (Suomi, 1958; House, 1965; Suomi, et al., 1967; Vonder Haar, 1968; and House, Sweet, et al., 1973). This technique has been successfully applied to the study of the global radiation budget and seasonal variations across latitudinal zones. However, the assumptions made will lead to inaccurate values of Q for the radiation budget of regions for the following reasons: (a) the values of We and Wr of a given region are determined by including contributions from neighboring regions, (b) the angular distributions of N and Nr are neglected. Nevertheless, the technique represents, perhaps, the simplest way of interpreting satellite radiometer data. Some of the early applications of this technique are mentioned below.

TIROS IV carried a radiation balance experiment of the University of Wisconsin design consisting of two WFOV radiometers (House, 1965). The surface of one sensor was black and the other was anodized aluminum to make it "white." House used the black sensor to show that it is possible to determine the radiation budget of the E-A system by using

data from only the black radiometer.

Vonder Haar (1968) described the energy budget of the E-A system from data collected for more than 40 months by sensors carried on board Explorer VII, TIROS IV, TIROS VII, and experimental satellites. These sensors were WFOV flat plate and hemispherical radiometers and medium resolution scanning radiometers. Vonder Haar generated maps of the components of the radiation budget which exhibit features of the atmospheric circulation system persistent in each season and hence, should be incorporated into any numerical models intended to simulate atmospheric conditions.

L. Holloway (1957) demonstrated that there would be unavoidable smoothing of data collected by WFOV satellite radiometers. He discussed methods for desmoothing, that is, reversing part of the smoothing effects and hence restoring some of the spatial fluctuations that had been filtered out of the data. Further investigations in desmoothing of satellite radiometer data were carried out by F. B. House (1970, 1972).

Theoretical estimates of the effects introduced when the anisotropy of the radiation fields are taken into consideration was covered in detail by Bignell (1961). He showed that the anisotropy factor C ranges between 0.98 and 1.02 for LWR, and between 0.9 and 1.1 for SWR. This factor is equal to one for isotropic radiation.

Two techniques were developed for obtaining the radiation fluxes We and Wr (Pina and House, 1975a). In both of these techniques, the E-A system is divided into regions which have homogeneous emitting and reflecting characteristics. One of these techniques is termed instantaneous for it yields the values that We and Wr have at the instant the

satellite makes a pass over the regions observed. The number of observations, which are made during a single satellite pass, matches the number of regions under study. The other technique is termed the best fit. In this technique, the number of observations (taken during several passes of the satellite) is much larger than the number of regions observed. An approximate solution is obtained by the method of least squares. A preliminary application of the instantaneous technique to a hypothetical flat E-A system yielded excellent results.

Campbell, et al. (1975) assumed an axisymmetric radiation field and divided the E-A system into zonal or latitudinal bands. The resulting system of linear simultaneous equations was solved using matrix inversion techniques.

The above zonal problem was approached by Smith and Green (1975a), that is, the radiation field was considered to depend on latitude but not on longitude. In addition, it was assumed that all measurements are taken at a constant altitude, that the angular characteristics of the radiation are a function of the zenith angle only (not of the azimuthal angle), and that this function is the same for the entire globe. Based on these assumptions, it was determined that the eigenfunctions of the measurement operator are Legendre polynomials which form a complete set. Hence, the power measurement and the radiation flux can be expanded in terms of these polynomials in order to obtain the desired results. It was concluded by Smith and Green that the assumptions made are reasonable for emitted LWR but not for reflected SWR.

Parameter estimation techniques were employed by Smith, et al. (1975b) to find a solution to the problem of determining the fluxes

We and Wr. Estimates of the zonal values of these fluxes were obtained by use of the Gauss-Markov theorem. It was established that the spatial resolution possible with WFOV data is limited due to limitations in the accuracy of the results imposed by the smallest eigenvalue of the integral operator. It was concluded that with some additional work, the estimation technique formulated for the zonal case could be extended to the regional case.

Pina and House (1975b) applied the instantaneous technique to a spherical E-A system in order to obtain the instantaneous values of We and Wr. The best fit technique was also applied to this system in order to calculate time-averaged values of We. These two techniques had been partially developed previously and successfully applied to a flat E-A system (Pina and House, 1975a). In all instances, the regional values of We and Wr obtained were satisfactory.

It should be pointed out that both of these techniques are independent of the shape of the orbit, i.e., circular or elliptical orbits are treated in exactly the same manner. However the altitude of the satellite must be known at the time of each measurement.

Smith and Green (1976a) treated the regional case of determining the E-A radiation fluxes. Some of the assumptions on which their investigation was based are that the angular dependence of the radiances measured is a function of the zenith angle of the radiometer making the observation, and that the satellite orbit is circular. One important conclusion reached in this investigation is that the accuracy of the results is dependent upon the resolution. A similar analysis which included data gathered with RFOV radiometers was also conducted (Smith and Green, 1976b).

Optimum satellite orbits

A fundamental question regarding the energy of the E-A system is the following (Suomi, 1961). Does the E-A system possess a self-regulating mechanism which restores the equilibrium of the global radiation budget whenever departures from this state occur? The answer to this question could not be provided, for instance, by the experiment on board Explorer VII, since observations of the whole earth were not obtained and, according to Suomi, the orbit was not adequate for that purpose. Then, the following question is pertinent. What is the optimum orbit required in order to sample all areas of the E-A system equally? That is, what orbit is required for all areas to have equal sampling weights?

House (1961) studied the above sampling problem by assuming WFOV spherical radiometers of high thermal capacity. He determined that a combination of two orbits of specific orbital parameters would fulfill the equal weighting requirement for determining the fluctuations in the radiation balance of the entire E-A system.

Harrison, et al., (1976) analyzed satellite systems with different orbital altitudes and inclinations and with radiometers of different fields of view. Flight simulations of these satellites were conducted over an E-A system radiation model. It was determined that several satellites having orbits of varying degrees of inclination are required to obtain adequate coverage of the E-A system. This is necessary in order to obtain regional, zonal, and global monthly mean flux values with the desired degree of accuracy.

Angular dependence of radiation

The angular distribution of the E-A system was investigated during a geophysical rocket flight on August 27, 1958 (Liventsov, et al., 1966). The rocket probe reached an altitude of about 450 km. The angular and altitude dependence of the earth's radiation was determined without difficulty. It was found that the intensity of the radiation diminishes toward the earth's limb.

Data from TIROS III over the Sahara desert was used to investigate limb darkening effects (Larsen, et al., 1963). The limb darkening values measured were found to be significant and to exceed the theoretical values obtained by using model atmospheres. This fact provided one of the motivations to include in the present investigation a study of how the results obtained are affected when an observed radiation field is erroneously assumed to be isotropic during data interpretation.

The data from TIROS IV was used to study the angular variation of solar radiation that was reflected from low stratiform clouds. The anisotropy of the reflected radiation was expressed in terms of two parameters: (a) the specular angle ω, (b) the backscattering angle ψ_o. It was concluded that the albedo is dependent on these two parameters, especially the specular angle.

The anisotropy of the SWR reflected from clouds was also investigated by Ruff, et al., (1967). It was determined that the anisotropy is more pronounced for large solar zenith angles. One of the main findings was the high intensity values of the reflected radiation for azimuthal angles of about 180° from the sun and for large zenith angles.

The last two investigations represented an additional incentive to include in the present research a study of the effects that the erro-

neous choice of a diffuse reflection model during data interpretation has upon the results.

This chapter has outlined some of the historical developments of satellite radiometry that are important to the subject of the present investigation, namely, the determination of We and Wr for regions smaller than the FOV of LSR radiometers.

CHAPTER III. BASIC CONCEPTS OF SATELLITE RADIOMETRY

This chapter introduces some of the basic concepts, equations, and definitions of satellite radiometry which are pertinent to the development of the techniques presented in the following chapters.

Radiance (emitted) $N(\theta,\psi;\lambda,\phi,t)$. This is the energy emitted per unit normal area, per unit time, per unit solid angle, at time t by an elemental area dA centered at longitude λ, latitude ϕ, in the direction given by the zenith angle θ and the azimuthal angle ψ (refer to Figure 3-1). To simplify the notation, λ and ϕ are omitted so as to write only $N(\theta,\psi,t)$. These angles will also be omitted in the following definitions. The units of N are $W/(m^2 - sr)$.

Radiance (reflected) $Nr(\theta,\psi;\zeta,t)$. The definition of this quantity is similar to that for N except that Nr depends also on the zenith angle of the sun. The units of Nr are $W/(m^2 - sr)$.

Flux. This term describes the radiation crossing a real or imaginary surface per unit area, per unit time from all directions in a hemisphere. The units of flux are W/m^2.

Radiant emittance $We(t)$. This is the instantaneous flux emitted by an elemental area $dA(\lambda,\phi)$ into 2π steradians solid angle. The units of We are W/m^2. N and We are related by the following expression.

$$We(t) = \int_0^{2\pi} d\psi \int_0^{\pi/2} N(\theta,\psi,t) \sin\theta \cos\theta \, d\theta \qquad (3\text{-}1)$$

Radiant reflectance $Wr(\zeta,t)$. This quantity is the flux of solar radiation reflected by an elemental area dA. This definition is

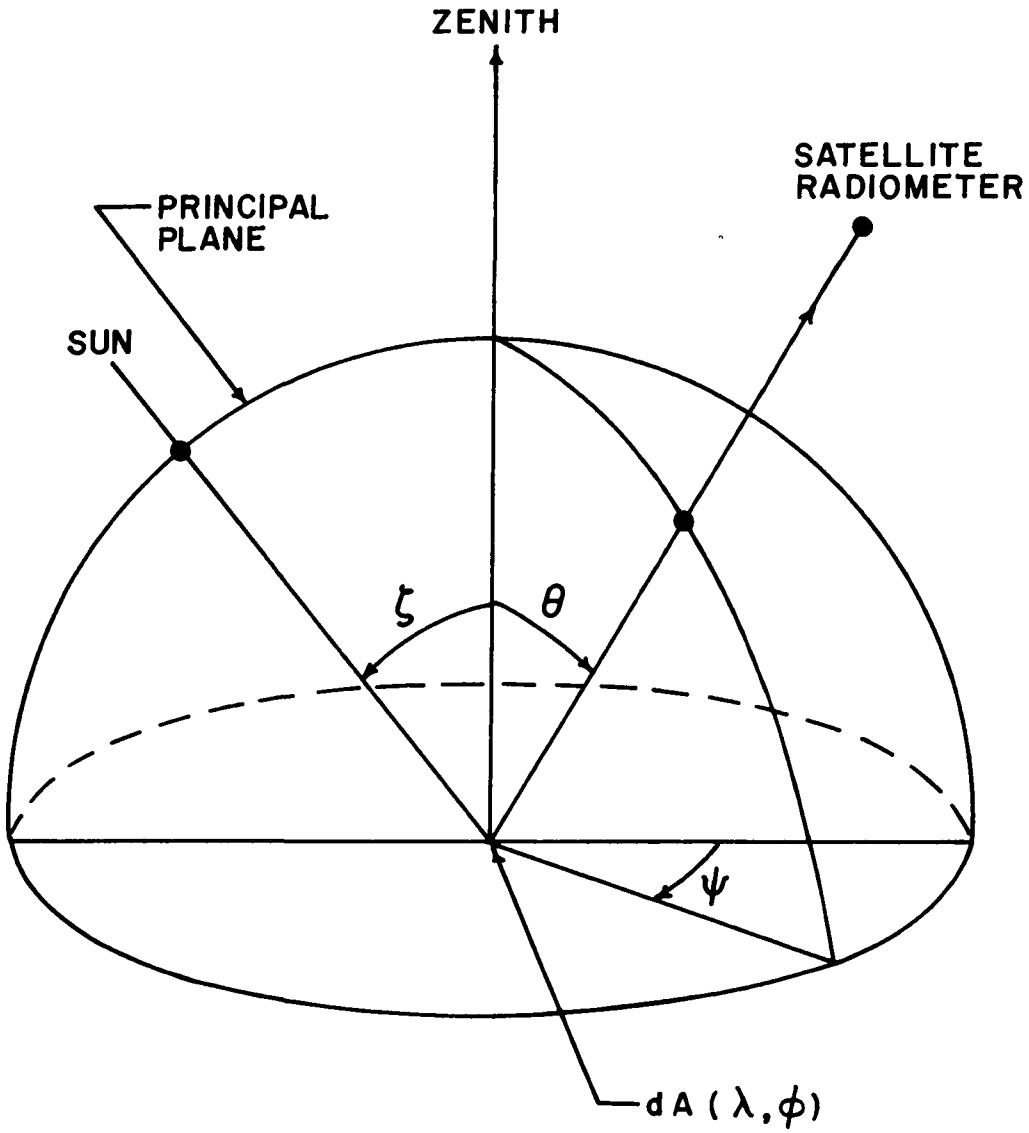

Figure 3-1. Satellite Radiometer Observation of an Elemental Area Centered at Longitude λ and Latitude ϕ.

similar to that of We except for the additional dependence on the sun's zenith angle ζ. The units of Wr are W/m^2. Nr and Wr are related as follows:

$$Wr(\zeta,t) = \int_0^{2\pi} d\psi \int_0^{\pi/2} Nr(\theta,\psi;\zeta,t) \sin\theta \cos\theta \, d\theta \qquad (3\text{-}2)$$

Irradiance H(t). This is the instantaneous flux impinging on a surface from all directions within a 2π steradians solid angle. Hence, We, Wr and H are similar quantities and differ only in the fact that they refer to emitted, reflected, and incident radiation.

Solar irradiance $Hs(\zeta,t)$. This quantity depends upon the solar zenith angle ζ, and is given by

$$Hs(\zeta,t) = H_o \cos\zeta \qquad (3\text{-}3)$$

where H_o is the solar irradiance for zero solar zenith angle.

Shape or configuration factor F. This factor represents that fraction of We (or Wr) originating at dA which is intercepted by a radiometer having a characteristic area A. F is defined by the following expression (Stevenson and Grafton, 1961) which relates F, A, We (or Wr), and the total radiant power P' intercepted by the radiometer

$$P' = F \, A \, We \qquad (3\text{-}4)$$

The characteristic area has the same value $A = \pi a^2$ for both sphere and plate radiometers, where a is the radius of either radiometer.

Dividing Eq.(3-4) through by A, one obtains the radiant power, P, per unit characteristic area of the radiometer.

$$P = F\ We \tag{3-5}$$

LDF - Limb darkening function $f(\theta)$. This quantity gives the angular dependence of $N(\theta,\psi,t)$ when the dependence on the azimuthal angle ψ is assumed negligible. Then, letting the radiance in the zenith direction $N^z(t)$ carry the time dependence, one has

$$N(\theta,\psi,t) = N(\theta,t) = N^z(t)\ f(\theta) \tag{3-6}$$

Substituting this expression in Eq.(3-1) one obtains

$$We(t) = N^z(t) \int_o^{2\pi} d\psi \int_o^{\pi/2} f(\theta)\ \sin\theta\ \cos\theta\ d\theta \tag{3-7}$$

Defining

$$I(f) \equiv \int_o^{\pi/2} f(\theta)\ \sin\theta\ \cos\theta\ d\theta \tag{3-8}$$

results in

$$We(t) = 2\pi\ N^z(t)\ I(f) \tag{3-9}$$

Directional reflectance $r(\zeta,t)$. This is the instantaneous value of the ratio given by

$$r(\zeta,t) = Wr(\zeta,t)/Hs(\zeta,t) \tag{3-10}$$

Albedo $A(\zeta,t)$. The instantaneous albedo is here defined to be identical to the directional reflectance $r(\zeta,t)$ defined above.

Bidirectional reflectance $\rho(\theta,\psi;\zeta,t)$. The instantaneous value of this quantity depends upon ζ, the zenith angle of the sun, as well as on the zenith angle θ and the azimuthal angle ψ of the radio-

meter. It is defined by the following ratio

$$\rho(\theta,\psi;\zeta,t) = Nr(\theta,\psi;\zeta,t)/Hs(\zeta,t) \tag{3-11}$$

Nr and ρ are independent of the angles θ and ψ for the case of diffuse reflection and Eq.(3-11) becomes

$$\rho^{dif}(\zeta,t) = Nr^{dif}(\zeta,t)/Hs(\zeta,t) \tag{3-12}$$

Radiometer power input P'. The LWR power intecepted by a flat plate satellite radiometer positioned at an arbitrary point in space is given by

$$P'_{LWR} = A \int_0^{2\pi} d\psi \int_0^{\alpha_{max}} N'(\alpha,\psi')\sin\alpha\cos\alpha\, d\alpha \tag{3-13}$$

where A is the area of the plate and $N'(\alpha,\psi')$ is the radiance expressed in terms of the nadir angle α and the azimuthal angle ψ'. The maximum value α_{max} of the nadir angle depends on the FOV of the radiometer, (wide or restricted) and on the altitude of the satellite. Eq.(3-13) can be rewritten as,

$$P_{LWR} = P'_{LWR}/A = \int_0^{2\pi} d\psi \int_0^{\alpha_{max}} N'(\alpha,\psi')\sin\alpha\cos\alpha\, d\alpha \tag{3-14}$$

Similarly, the reflected SWR power impinging on the satellite can be expressed as

$$P_{SWR} = \int_0^{2\pi} d\psi \int_0^{\alpha_{max}} N'_r(\alpha,\psi';\zeta)\sin\alpha\cos\alpha\, d\alpha \tag{3-15}$$

where $N'_r(\alpha,\psi';\zeta)$ is the reflected radiance expressed in terms of α, ψ' and ζ. Notice that the t has been left out of both equations and that P_{SWR} depends on the solar zenith angle ζ. The cos α factor in Eqs.(3-14) and (3-15) is equal to one for the case of a spherical radiometer.

Isotropic emission. In this case, the radiance N is independent of angle and Eq.(3-1) becomes

$$We(t) = N^{iso}(t) \int_0^{2\pi} d\psi \int_0^{\pi/2} \sin\theta \cos\theta \, d\theta \tag{3-16}$$

Thus,

$$We(t) = \pi N^{iso}(t).$$

Also, from Eq.(3-8)

$$f^{iso} = 1.0 \text{ and } I^{iso} = 0.5 \tag{3-17}$$

In the above, N^{iso}, f^{iso}, and I^{iso} represent the isotropic values acquired by the quantities N, f, and I, respectively.

Diffuse reflection. The reflected radiance Nr is not dependent on(θ,ψ), the direction of the observation; however, it still is dependent upon the sun's zenith angle ζ. Hence, Eq.(3-2) becomes

$$Wr(\zeta,t) = Nr^{dif}(\zeta,t) \int_0^{2\pi} d\psi \int_0^{\pi/2} \sin\theta \cos\theta \, d\theta \tag{3-18}$$

$$Wr(\zeta,t) = \pi Nr^{dif}(\zeta,t) \tag{3-19}$$

where $Nr^{dif}(\zeta,t)$ is the diffuse reflected radiance.

$R_1(\zeta)$ and $R_2(\theta,\psi,\zeta)$. These two parameters represent time averages of the following ratios.

$$R_1(\zeta) = r(\zeta)/r(0) = \overline{r(\zeta,t)/r(0,t)} \tag{3-20}$$

$$R_2(\theta,\psi,\zeta) = r(\zeta)/\pi\rho(\theta,\psi,\zeta) = \overline{r(\zeta,t)/\pi\rho(\theta,\psi;\zeta,t)} \tag{3-21}$$

where $r(0) = r(\zeta=0)$. Mean curves for these two quantities have been plotted by Raschke, et.al., (1973) and will be used when applying the bidirectional reflectance model to determinations of Wr.

The time average of Wr is from Eq.(3-10)

$$Wr(\zeta) = r(\zeta)\ Hs(\zeta)\ .$$

The time average of Nr for diffuse reflection is from Eq.(3-12)

$$Nr^{dif}(\zeta) = \rho^{dif}(\zeta)\ Hs(\zeta).$$

These time averages are related by Eq.(3-19), that is

$$Wr(\zeta) = \pi Nr^{dif}(\zeta)$$

It follows then that

$$r(\zeta) = \pi\rho^{dif}(\zeta)\ ,$$

and from Eq.(3-21)

$$R_2{}^{dif}(\zeta) = r(\zeta)/\pi\rho^{dif}(\zeta)=1.0\ . \qquad (3\text{-}22)$$

Angle relations. Figure 3-2 serves to define the following angles which are used when determining We: θ, the zenith angle of the satellite as seen from the observed area dA; α, the nadir angle of dA as seen from the satellite; γ, the geocentric angle between the satellite and dA. This figure does not show the solar zenith angle ζ; however, this angle appears in Figure 3-1. Figure 3-2 includes R, the radius of the E-A system; r, the distance from dA to the satellite; and H, the altitude of the satellite above the E-A's surface. The following are important relationships among the quantities defined above and which are used in the following chapters.

$$\theta = \alpha + \gamma \qquad (3\text{-}23)$$

$$R \sin\theta = (R+H) \sin\alpha \qquad (3\text{-}24)$$

$$R \sin\gamma = r \sin\alpha \qquad (3\text{-}25)$$

$$r^2 = R^2 + (R+H)^2 - 2R(R+H) \cos\gamma \qquad (3\text{-}26)$$

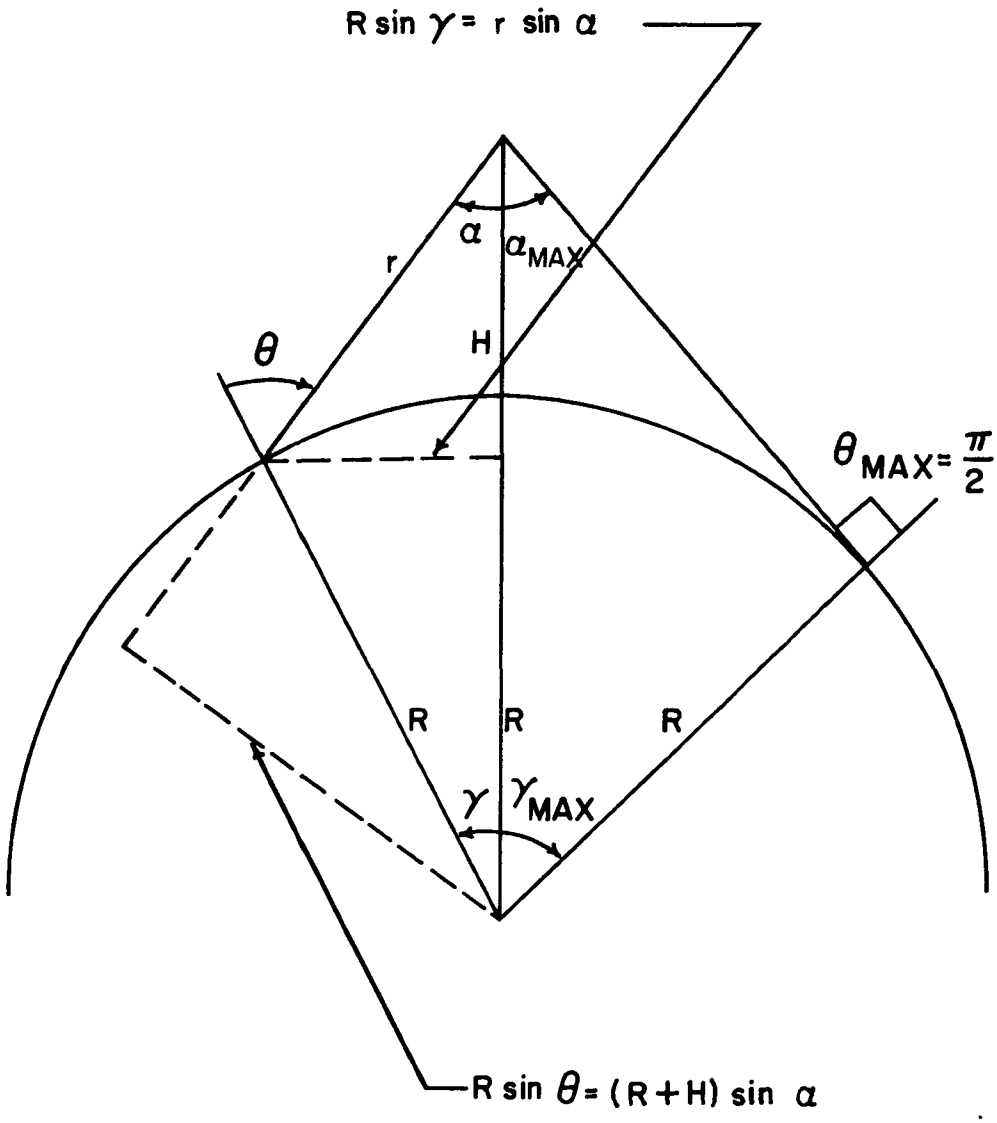

Figure 3-2. Pictorial Definition of Some of the Geometrical Parameters Used in Measuring We and Wr by a WFOV Satellite Radiometer.

CHAPTER IV. TECHNIQUES FOR OBTAINING THE RADIANT EMITTANCE

The instantaneous and best fit techniques for obtaining We are treated in detail in this chapter. The techniques are developed for the terrestrial emitted LWR flux first because this case is somewhat simpler than the reflected solar SWR.

Instantaneous technique

The values of We calculated by this technique are the values that the radiant emittances of the regions observed have during a single pass of the satellite. Because the meausurements are taken in a short time interval, the technique is called instantaneous and will be referred to as such in the subsequent discussion.

In this technique, the number of observations matches the number of unknowns (that is, the number of regions observed). Hence, if a solution exists, it is unique.

A. Technique development

The following development is for a horizontal flat plate satellite radiometer of unit area. The development also applies to the case of a spherical radiometer of unit area, except that the factor cos α is equated to one in all the equations containing it.

The satellite radiometer is assumed to make J=K observations of K regions as depicted in Figure (4-1). The groups of dissimilar arrows shown in this figure portray the fact that the magnitude and angular distribution of the radiance may vary from region to region at the surface of the E-A system. The power intercepted by the radiometer during the jth observation is given by Eq.(1-6) introduced previously

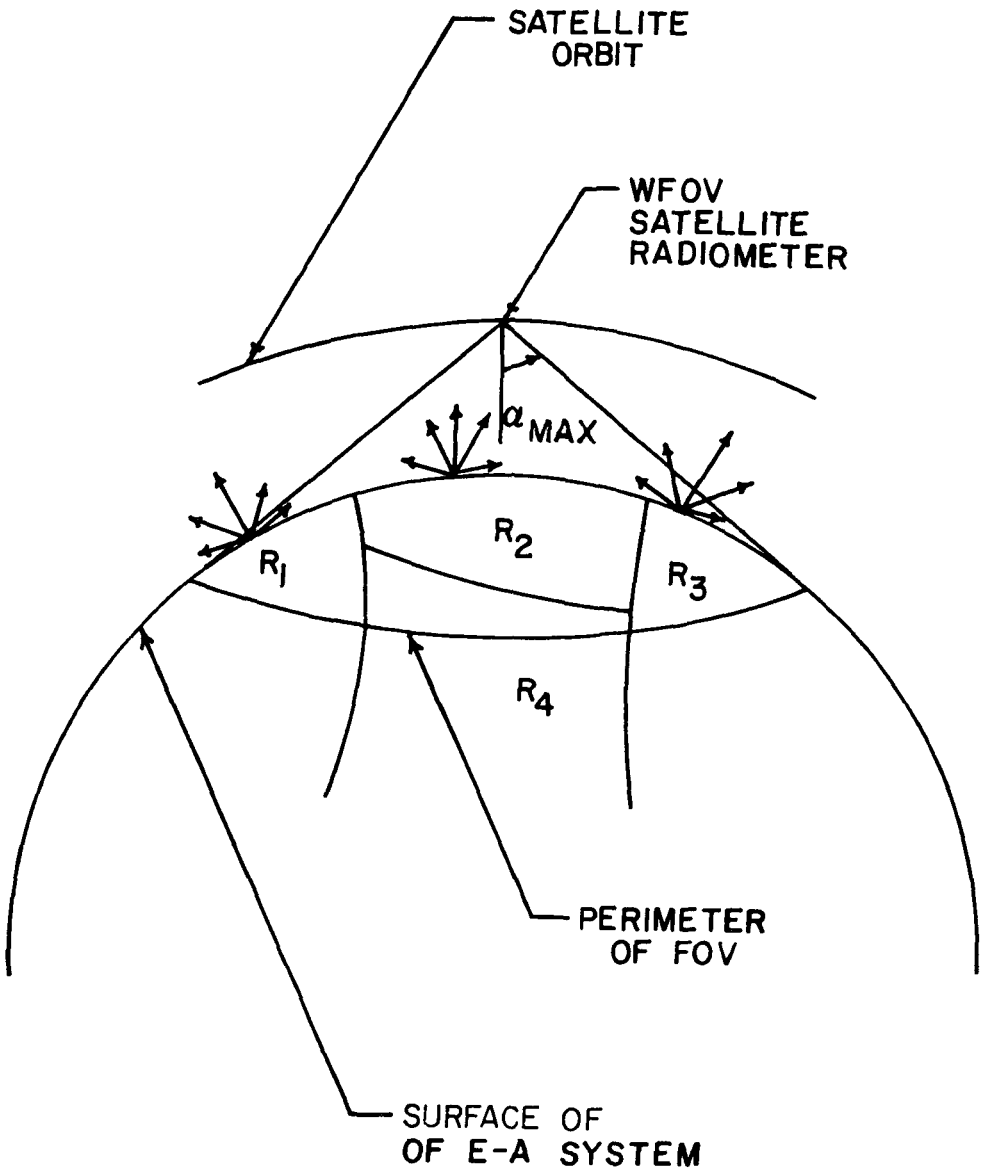

Figure 4-1. Observation of the LWR Emitted by the Several Regions within the FOV of a Low Spatial Resolution Radiometer.

and rewritten here in a slightly different form

$$P_j = \sum_{k=1}^{K} \int_{\psi_k'} d\psi' \int_{\alpha_k} N'(\alpha,\psi',t) \sin\alpha \cos\alpha \, d\alpha \qquad (4\text{-}1)$$

where P_j is the LWR power intercepted by the radiometer during the jth observation, α and ψ' are the nadir and azimuthal angles of the elemental area observed from the satellite, t is the time of the observation, and N' is the radiance when expressed in terms of α and ψ'. α_k and ψ_k' indicate that the pertinent lower and upper limits of integration of each of the regions within the FOV must be included in the expression. The sum is taken over K which is the total number of regions under study. However, those regions that do not appear within the FOV of a given observation will not be included in the corresponding sum.

Consider an elemental area dA within any of the regions observed. The radiance N and the radiant emittance We of dA are related by the following expression.

$$We(t) = \int_0^{2\pi} d\psi \int_0^{\pi/2} N(\theta,\psi,t) \sin\theta \cos\theta \, d\theta \qquad (4\text{-}2)$$

where θ and ψ are the zenith and azimuthal angles of the satellite as seen from dA, and N is the radiance expressed in terms of θ and ψ.

The problem that must be solved is stated as follows. By performing several power measurements P_j, use Eqs.(4-1) and (4-2) to obtain the We values of the regions observed.

The instantaneous technique developed to solve the above problem is described as follows.

1. The E-A system's surface is divided into 2060 equal elemental areas ΔA in order to perform numerically the integrations in Eq.(4-1). A computer program was generated to do this division, rank the elements into a one-dimensional array, and specify the longitudes and latitudes of the boundaries and the centroids of all the ΔA's. These elemental areas remain fixed on the surface of the E-A system as the satellite moves, regardless of the type of satellite orbit (circular or elliptical). Two other schemes were evaluated to perform the numerical integrations but their application was found too cumbersome. Refer to Appendix A for a detailed description of the schemes considered, as well as the procedure followed to accomplish the division into ΔA's according to the technique selected.
2. The surface of the E-A system is divided into regions having homogeneous emitting and reflecting characteristics which are distinct from those of adjacent regions. This division can be made on the basis of topographic differences, and/or on the basis of the results obtained from previous satellite observations. The regions are defined in terms of the elemental areas ΔA. Each region is made up of an integral number of these ΔA's.
3. The dependence of N on the azimuthal angle ψ is assumed negligible and hence can be represented as follows (Raschke, et al., 1973).

$$N(\theta,\psi,t) = N(\theta,t) = N^{z}(t)\ f(\theta) \qquad (4\text{-}3)$$

where $N^{z}(t)$ is the radiance in the zenith direction which carries the time dependence of N, and $f(\theta)$ is the limb darkening function (LDF) which gives the angular distribution of N. Eq.(4-3) serves

to define more precisely the concept of a region. The value of $N^z(t)$ may change with time and varies among adjacent regions, but it is uniform throughout a given region. The LDF $f(\theta)$ may have a different form in each adjacent region. This form is assumed to be uniform throughout a region; however, it is also possible to consider a region as having more than one LDF.

4. The relationship between N and We can now be greatly simplified by substituting Eq.(4-3) into Eq.(4-2) to obtain

$$We(t) = 2\pi\, N^z(t) \int_o^{\pi/2} f(\theta) \sin\theta \cos\theta\, d\theta \tag{4-4}$$

It is convenient to define the integral in this expression as follows

$$I(f) \equiv \int_o^{\pi/2} f(\theta) \sin\theta \cos\theta\, d\theta \tag{4-5}$$

and rewrite Eq.(4-4) as

$$We(t) = 2\pi\, N^z(t)\, I(f) \tag{4-6}$$

from which one has

$$N^z(t) = \frac{We(t)}{2\pi I(f)} \tag{4-7}$$

5. An expression for the power which is contributed by an elemental area ΔA to a radiometer measurement is derived as follows. Let ΔA_{ijk} represent the ith elemental area of the kth region that is within the FOV of the jth observation. ΔP_{ijk} denotes the power increment that this elemental area contributes to the jth observation. Then one writes

$$\Delta P_{ijk} = N_{ijk}\ \Delta A_{ijk} \cos\theta_{ijk}\ \frac{A_s \cos\alpha_{ijk}}{r_{ijk}^2} \tag{4-8}$$

where the subscripts ijk have the same meaning given above for ΔA_{ijk}. N_{ijk} is the radiance at ΔA_{ijk} in the direction of the radiometer, θ_{ijk} is the zenith angle of the radiometer at ΔA_{ijk}, α_{ijk} is the nadir angle of ΔA_{ijk} as seen from the satellite, and r_{ijk} is the distance between ΔA_{ijk} and the radiometer. A_s, the characteristic area of the radiometer, is assumed to be unity as mentioned previously. Since all the elemental areas are equal, it is unnecessary to affix subscripts to ΔA. Hence, Eq.(4-8) becomes

$$\Delta P_{ijk} = N_{ijk} \Delta A \left(\frac{\cos \theta \cos \alpha}{r^2}\right)_{ijk} \tag{4-9}$$

6. The power which a region contributes to an observation is derived from Eq.(4-9), as follows. The value of N_{ijk} in this equation is the same as $N(\theta,\psi,t)$ given by Eq.(4-3) in terms of the zenith radiance N^z and the LDF $f(\theta)$. Hence, substituting Eq.(4-3) into Eq.(4-9) one obtains

$$\Delta P_{ijk} = N_k^z \Delta A \left(\frac{f(\theta) \cos \theta \cos \alpha}{r^2}\right)_{ijk} \tag{4-10}$$

where only the k subscript is affixed to N^z in order to show that the value of N_k^z is uniform throughout the kth region. The subscripts i, j are unnecessary since the value of N_k^z is independent of both the elemental area observed and the position of the observation. From Eq.(4-7) one can write

$$N_k^z = \frac{We_k}{2\pi I(f_k)} \tag{4-11}$$

which when substituted into Eq.(4-10) yields

$$\Delta P_{ijk} = \frac{\Delta A}{2\pi I(f_k)} \left(\frac{f(\theta) \cos\theta \cos\alpha}{r^2}\right)_{ijk} We_k \qquad (4\text{-}12)$$

From Eq.(3-5), which defines the shape factor, ΔP_{ijk} can be written as

$$\Delta P_{ijk} = F_{ijk} We_k \qquad (4\text{-}13)$$

By comparing Eqs.(4-12) and (4-13) one obtains

$$F_{ijk} = \frac{\Delta A}{2\pi I(f_k)} \left(\frac{f(\theta) \cos\theta \cos\alpha}{r^2}\right)_{ijk} \qquad (4\text{-}14)$$

The power increments ΔP contributed by the I elemental areas of the kth region which appear within the FOV of the jth observation are added up and Eq.(4-13) is then used to obtain

$$P_{jk} = \sum_{i=1}^{I} \Delta P_{ijk} = We_k \sum_{i=1}^{I} F_{ijk} = F_{jk} We_k \qquad (4\text{-}15)$$

where P_{jk} is the power contributed by the kth region to the jth observation; F_{jk} is the sum of the shape factors F_{ijk} of the kth region and jth observation.

7. An expression for the total power P_j contributed to the jth observation by all the regions within the FOV of the radiometer is given by Eq.(4-1). Also, by adding the P_{jk}'s of all the K regions under study as given by Eq.(4-15) one obtains a different expression for P_j

$$P_j = \sum_{k=1}^{K} F_{jk} We_k \qquad (4\text{-}16)$$

Clearly, if a particular region (say, region ℓ) does not appear within the FOV of the jth observation, then the corresponding

configuration factor $F_{j\ell}$ is zero and will not appear in Eq.(4-16). From a comparison of Eqs.(4-1) and (4-16) one sees that the double integral appearing in Eq.(4-1) is equivalent to the simple product $F_{jk}\ We_k$ in Eq.(4-16). The expression for F_{jk} is easily obtained from Eqs.(4-14) and (4-15), namely

$$F_{jk} = \sum_{i=1}^{I} \frac{\Delta A}{2\pi I(f_k)} \left(\frac{f(\theta)\ \cos\theta\ \cos\alpha}{r^2}\right)_{ijk} \tag{4-17}$$

8. Since there are K regions observed (i.e., K unknown values of We), then the number J of observations (i.e., J equations of the type of Eq.(4-16)) must be equal to K. The J equations can then be written as follows.

$$\begin{aligned}
P_1 &= F_{11}\ We_1 + F_{12}\ We_2 + \ldots + F_{1K}\ We_K \\
P_2 &= F_{21}\ We_1 + F_{22}\ We_2 + \ldots + F_{2K}\ We_K \\
&\cdot \\
&\cdot \\
&\cdot \\
P_J &= F_{J1}\ We_1 + F_{J2}\ We_2 + \ldots + F_{JK}\ We_K
\end{aligned} \tag{4-18a}$$

These equations can be represented in matrix form as

$$\begin{bmatrix} F_{11} & F_{12} & \cdots & F_{1K} \\ F_{21} & F_{22} & \cdots & F_{2K} \\ \cdot & & & \\ \cdot & & & \\ \cdot & & & \\ F_{J1} & F_{J2} & \cdots & F_{JK} \end{bmatrix} \begin{bmatrix} We_1 \\ We_2 \\ \cdot \\ \cdot \\ \cdot \\ We_K \end{bmatrix} = \begin{bmatrix} P_1 \\ P_2 \\ \cdot \\ \cdot \\ \cdot \\ P_J \end{bmatrix} \tag{4-18b}$$

Symbolically, these matrices can be written as

$$F\{We\} = \{P\} \tag{4-18c}$$

where F is the JxJ (or KxK since J=K) configuration factor matrix. {We} and {P} are the column matrices formed by the We values of the K regions and the P powers of the J observations, respectively.

9. The inverse matrix F^{-1} is obtained from the configuration factor matrix F by the use of available matrix inversion subroutines. It is then tested by computing the products FF^{-1} to ascertain that the identity matrix is obtained. By operating with the inverse matrix F^{-1} on the column matrix {P} which is made up of the J power values measured, the column matrix {We'} is obtained, that is

$$F^{-1}\{P\} = \{We'\} \tag{4-19}$$

If the We' values of the column matrix {We'} obtained by using Eq.(4-19) are the same as, or very close to, the actual We values of the K regions, the problem has been solved by using the procedure outlined above. When the values of P were exact (that is, did not contain observational uncertainties), the values of We' were found to agree with the actual We values to at least six significant decimals. This indicates that the inversion computations do not introduce significant errors (e.g., rounding errors). In this case then, one can write

$$F^{-1}\{P\} = \{We\} \tag{4-20}$$

B. Observational errors

Serious difficulties arise when the power measurements include Gaussian random observational errors δP in addition to the exact power values P. In this case, the We' values obtained for the regions include, in addition to the actual We values, errors δWe which in general are found unacceptable.* In this case, using $\{P'\}=\{P+\delta P\}$ and $\{We'\} = \{We + \delta We\}$, one can write the following expression

$$F^{-1}\{P'\} = F^{-1}\{P+\delta P\} = \{We'\} = \{We + \delta We\} \qquad (4\text{-}21)$$

Subtracting Eq.(4-20) from Eq.(4-21), one obtains

$$F^{-1}\{\delta P\} = \{\delta We\} \qquad (4\text{-}22)$$

It is apparent from Eq.(4-22) that if the δWe errors are much larger than the δP errors, the inverse matrix F^{-1} produces large magnification of the δP errors. An inverse matrix F^{-1} that magnifies significantly the random power errors is here defined to be unstable. The original matrix F is termed an ill-conditioned matrix on the basis of similar definitions made by Faddeev and Faddeeva (1963). If F^{-1} is stable, F is known as a well-conditioned matrix.

If the power errors δP are systematic, no difficulties are encountered. The inverse matrix F^{-1} does not magnify this type of error according to Eq.(4-22). However, if the errors δP are combinations of systematic and Gaussian random errors, F^{-1} magnifies them just as in the case of pure Gaussian random errors.

---

*Acceptability criteria are based on the recommendations made at the 1975 conference of radiation budget investigators in Chicago. The desired and useful accuracy requirements recommended are ± 3 W/m^2 and ± 15 W/m^2 respectively.

The instability of the matrix F^{-1} results from observing only small portions of some of the regions as will be shown. Because of this instability of F^{-1}, the instantaneous technique (as outlined in the above nine steps) is inadequate for those cases where small portions of regions are observed. Unless some sort of stabilization technique is found to stabilize F^{-1}, the instantaneous technique is of no practical use as described so far. When this difficult situation in the development of the instantaneous technique was encountered, a literature search revealed that other investigators had met equations with similar instability problems (Phillips, 1962; Twomey, 1963, 1965, 1966; Fleming and Wark, 1965; and Wark and Fleming, 1966).

C. Matrix stabilization

After considerable effort, a technique was found for stabilizing the inverse of the configuration factor matrix. Essentially, this technique consists in removing any non-diagonal matrix element F_{jk} (jth observation, kth region) whose value is below a pre-determined test value and adding it to the diagonal element F_{jj} in the same row as the element F_{jk}. In doing this, the sum of the elements in the row in question (the jth row) is preserved. This sum, Σ_j, is equal to the configuration factor of the total area within the FOV of the radiometer.

It became apparent that the above matrix parameter Σ_j is a quantity that must be preserved. When non-diagonal elements F_{jk} (whose values were below the pre-determined test value mentioned above) were removed but were not added to the diagonal elements F_{jj} in the same rows as the elements F_{jk}, the sums (Σ_j) of the elements of the pertinent rows were,

therefore, slightly changed. The resulting inverse matrix was even more unstable than the initial one.

After applying the above stabilizing scheme to the original configuration factor matrix F, the new matrix was found to be well-conditioned. The symbol F_{wc} will be used to denote this new matrix and F_{wc}^{-1} its inverse. We" will represent the radiant emittance values obtained with the new stabilized inverse matrix F_{wc}^{-1}. These new radiant emittance values and the errors they contain will be denoted by $We^{(1)}$ and $\delta We'$, respectively, if the powers used are exact (i.e., no uncertainties); and by We" and δWe", respectively, if the power values contain errors. That is

$$F_{wc}^{-1} \{P\} = \{We^{(1)}\} = \{We + \delta We'\} \tag{4-23}$$

$$F_{wc}^{-1} \{P'\} = F_{wc}^{-1} \{P + \delta P\} = \{We"\} = \{We + \delta We"\} \tag{4-24}$$

As shown later, all the new We" values exhibit a significant improvement over their corresponding We' values obtained previously with the unstable matrix. Only in those cases where very small portions of the regions are observed, are their corresponding δWe"'s found unacceptable. However, as will be shown,acceptable results for these regions are obtained from other satellite radiometer observations which include within their FOV's sufficiently large portions of the regions under discussion.

A different way of demonstrating the striking difference between the original ill-conditioned matrix F and the new well-conditioned matrix F_{wc} is by comparison of their condition numbers. The condition number H used here is defined by Faddeev and Faddeeva (1963) as follows.

$$H = \sqrt{\mu_1/\mu_2}$$

where μ_1 and μ_2 are the largest and the smallest eigenvalues of the matrix F^TF , where F^T is the transpose of F. The condition number H_{wc} of the new matrix $F_{wc}^T F_{wc}$ is much smaller than H, the original condition number, which indicates that the new matrix F_{wc} has been rendered well-conditioned (Cohen, et al., 1973).

It should be noted that since the above stabilization scheme changes the structure of the configuration factor matrix, the resulting matrix is not a true representation of the physical situation observed. Furthermore, this structural change of the matrix also causes a new type of error $\delta We'$ to be included in the results, that is, in the values of We" obtained with the new stabilized matrix F_{wc}^{-1} . It will now be shown that neither of the above items introduces a major difficulty.

The removal of a very small matrix element F_{jk} from its jk position and addition of it to the jj diagonal element is equivalent to seeing a little less area of the kth region at the limb, and seeing a little more of the jth area also at the limb during the jth observation. Since the jth and kth regions have different We values, the above modification is also equivalent to a change in the power measurement of the jth observation by an amount ΔP_j given by

$$\Delta P_j = F_{jk}\, We_j - F_{jk}\, We_k = F_{jk}(We_j - We_k) \qquad (4\text{-}25)$$

The test value used as a criterion for deciding if a matrix element must be removed is 0.016 for the plate radiometer and 0.032 for the sphere. Assuming that the difference between the We values of the jth and kth regions is as high as 100 W/m^2, the value of ΔP_j for

the plate could be as high as

$$\Delta P_j \simeq (0.016)(100) = 1.6 \text{ W/m}^2 \qquad (4\text{-}26)$$

which is a negligible error since it only represents about nine tenths of a percent of the average power (about 177 W) measured by a plate at an 800 km altitude. The value of ΔP_j given by Eq.(4-26) is the difference between the actual power measurement and the power that would be measured if the conditions portrayed by the new matrix F_{wc} actually existed. Hence, ΔP_j represents the power error introduced by performing the matrix element translation described above.

However, the new errors $\delta We'$ that are introduced in the results by the stabilized matrix are the main concern. An estimate of these new errors can be obtained by operating with the new stabilized matrix F_{wc}^{-1} on the column matrix {P} made up of error-free power values, as shown in Eq.(4-23). Regions whose results are predicted acceptable, as described below, had $\delta We'$ errors lower than 1.0 W/m^2. The worst $\delta We'$ errors are found only in those cases where very small sections of the pertinent regions are observed, as it is in the case of the $\delta We''$ errors previously mentioned. As indicated before, the results for these cases become acceptable when larger portions of the corresponding regions are observed as will be shown later.

D. Prediction technique

It is of the utmost importance to know which of the We values obtained with the instantaneous technique will be acceptable and which will be unreliable. It is recognized that the best way to insure that the results obtained are accurate is by performing simultaneous independent observations from other spacecraft, aircraft, or

balloons. However, it would be impractical to perform this type of verification for every measurement. A natural question to ask is: can the measurements themselves be used to predict the reliability of the final data?

The answer to the above question is yes. After investigation of several schemes for predicting the quality of the data to be obtained, a simple technique was found which yielded excellent results. This technique consists in evaluating the following prediction parameter (PP) for each of the regions.

$$PP = (S_k \; F_{jj}/\Sigma_j) \times 1000 \qquad (4\text{-}27)$$

where S_k is the sum of the elements in the kth column (kth region), F_{jj} is the diagonal element of the jth column and jth row (jth observation), and Σ_j is the sum of the elements in the jth row. This last sum is the configuration factor of the whole FOV of the jth observation.

A realistic and justifiable criterion was found for determining a cut-off value of PP which may be applied to any region. If the PP of a given region is below this value, the corresponding We is unreliable because of insufficient information. If the PP is above this value, We is considered acceptable. The cut-off value of PP was fixed at 150 for a spherical radiometer, and at 100 for a horizontal plate radiometer. Justification for establishing these particular cut-off values will be presented later.

Once the above prediction scheme is applied, only the results of those regions whose PP values meet the above test need be considered.

Regions whose PP values fall below the required cut-off values are no longer taken into account in the evaluation of the data gathered during the satellite pass under consideration. Future satellite passes which observe larger portions of these regions are necessary for making accurate determinations of their We values.

It is to be noted that one of the important characteristics of the instantaneous technique is that even though the We values obtained for some of the regions are considered totally unreliable, these results do not affect those We values which are predicted acceptable. In other words, the instability of the matrix resulting from observing small sections of some of the regions produces unacceptable errors only for these regions. The errors generated for the remaining regions fall within acceptable limits. Without this characteristic, the instantaneous technique would be totally unreliable, or at least impractical. It would perhaps be impossible to predict to what extent the effects of "bad" regions would influence the results obtained for the "good" regions.

In several instances it has been pointed out that the instability of the configuration factor matrix is the result of not observing sufficiently large portions of all the regions investigated. That is, some of the S_k values of the configuration factor matrix are too small while others are too large. As will be shown, when the satellite positions are so chosen that sufficiently large portions of all regions are observed, the instability of the matrix vanishes. When this is the case, there is no need for stabilizing the inverse of the original matrix, nor is there need for any prediction scheme since all the We values are

found acceptable.

From the above, one can conclude that it was imperative to develop the stabilization and prediction techniques only because not all the geometric configurations of satellite orbits and regions observed guarantee sufficient coverage of the regions under study.

E. Angular distribution function

One would expect errors in the results if the function used to describe the angular distribution of the radiation field during data interpretation does not adequately represent the actual angular distribution. Then one questions how significant these errors are, or how they could be estimated.

Several LDF's which describe the angular distribution of the LWR emitted by areas with different topographical characteristics have been studied (Raschke, et al., 1973). One of the two LDF curves shown for the desert samples by Raschke, et al. exhibits the largest deviations for large zenith angles from the value of unity which all LDF's have for zero zenith angle. A hypothetical LDF was generated based on the above LDF for a desert region by extrapolating this curve to a zenith angle of ninety degrees. This LDF then represents the most notable departure from the isotropic case. These two extreme cases (LDF and isotropic) were used to make estimates of the errors introduced when using an incorrect function to describe the angular distribution of a LWR field

The following procedure was implemented to estimate the effects caused by use of an erroneous angular function. A LWR field was assumed to be described by the LDF generated for this purpose and the

power measurements resulting from a set of simulated satellite observations were calculated. These power measurements were then modified with Gaussian, systematic, and combinations of Gaussian and systematic uncertainties. During the interpretation stage of these modified power measurements, the LWR field was again assumed described by the LDF originally used to calculate the powers. This case will be referred to as LDF/LDF. The δWe" errors obtained for the regions observed were used as a standard for comparison with the results obtained in those cases in which a different angular function was used during interpretation of the data. Two cases were considered: a) LDF/ISO, where the field is described by a LDF and an isotropic field is assumed during data interpretation; b) LDF-ISO/LDF, in which a combination of regions with a LDF field and regions with an isotropic field are observed and a totally isotropic field is assumed during data interpretation. In both cases, the results obtained for those regions that passed the prediction technique test were found acceptable as will be shown later.

F. Homogeneity condition

A basic assumption of the instantaneous technique is that the E-A system's surface can be divided into regions whose We values are fairly uniform within each region. As indicated previously, it is assumed that each region has homogeneous emitting and reflecting characteristics which are different from those of adjacent regions. Therefore, this type of topographic division is assumed to exist whenever the instantaneous technique is applied. As mentioned before, this method requires that the number of observations match the number of regions (i.e., the

number of unknowns), and hence, a unique solution is obtained.

If the physical conditions are such that one of the regions is split into two large subregions having significantly different We values, then, the system has one more unknown, and the number of observations must be correspondingly increased. However, as will be shown, the instantaneous technique can even deal with some of these cases without adding the required extra observation. In the majority of cases, region inhomogeneities can be interpreted as sources of power perturbations which are similar in character to the observational errors (combinations of Gaussian random and systematic) treated previously. This is especially true in those cases where the We gradient within a region is small. However, even when there is a large gradient between two or more small adjacent sections of a region, the instantaneous technique yields acceptable results.

A figure of merit or evaluation parameter (EP) was developed for evaluating the acceptability of the results derived from observations which include regions with varying degrees of inhomogeneity. As will be shown, the difference ΔWe between the two values of We in a given inhomogeneous region was varied to observe the effects upon the results. The evaluation parameter EP defined below was shown to be correlated with the errors in the results so that it could be used to evaluate the acceptability of the results.

The value of EP is determined as follows. One obtains a weighted average $\overline{We}_j$ for the jth observation by dividing the power P_j of this observation by Σ_j, the total configuration factor of the jth observation. The value of $\overline{We}_j$ calculated for the jth observation is assigned to the

region for which k=j (since those regions that pass the prediction scheme test have large diagonal elements) and is identified as We_k. The We_k'' values obtained for those regions whose results are considered acceptable by the prediction scheme are then subtracted from the corresponding $\overline{We}_k$ values, that is

$$\epsilon_k = \overline{We}_k - We_k'' \tag{4-28}$$

The We_k'' values are obtained by operating with the stabilized inverse matrix F_{wc}^{-1} on the column matrix {P'} of perturbed powers according to Eq.(4-24).

The evaluation parameter EP is defined as the rms of these differences ϵ_k obtained for all regions that have passed the prediction technique test. Hence,

$$EP = [\frac{1}{L} \sum_{\ell=1}^{L} \epsilon_\ell^2]^{1/2} \tag{4-29}$$

where L is the number of regions found acceptable according to the prediction scheme test. An illustration will be given later in which the values of these parameters, ϵ_k and EP, are presented in tabular form for comparison with the rms's of the $\delta We''$ errors obtained for ten sets of observations which include uncertainties and/or inhomogeneity errors. It was found that those regions which contribute least to the satellite observations may have a value of $\Delta We = 50\ W/m^2$ and still yield acceptable We_k'' results. On the other hand, regions that make large contributions to the set of observations must have values of ΔWe smaller than $50\ W/m^2$ in order to give accurate results. In those cases in which the value of ΔWe is too large,

the value of the evaluation parameter EP serves to indicate the presence of large power perturbations caused by large region inhomogeneities. This type of situation requires further investigation in order to establish the number of regions which is actually observed in order to match them with an equal number of radiometer observations.

G. Results

An illustration of the use of the instantaneous technique is presented in detail in order to discuss the types of results obtained.

It is assumed that a satellite carrying a spherical and a horizontal plate radiometer circles the earth in an orbit whose inclination is slightly greater than 90^{o}. Six observations are made of six hypothetical regions which have different We values. The LWR field of these regions is described by a LDF which, as described previously, is an extended version of one of the LDF's presented by Raschke, et al., (1973) for a desert area. Figure 4-2 is a schematic representation of these regions and the subsatellite points of the six observations. This figure also shows for each region the identifying number, the equivalent area in square degrees of great circle arc, and the We value. The identifying numbers of the six satellite positions from which the observations are made, as well as the FOV of the 3rd observation are also shown.

The 6x6 configuration factor matrices generated for the sphere and plate radiometers are presented in Figure 4-3. These matrices were constructed from the six observations according to Eqs.(4-17) through (4-18c).

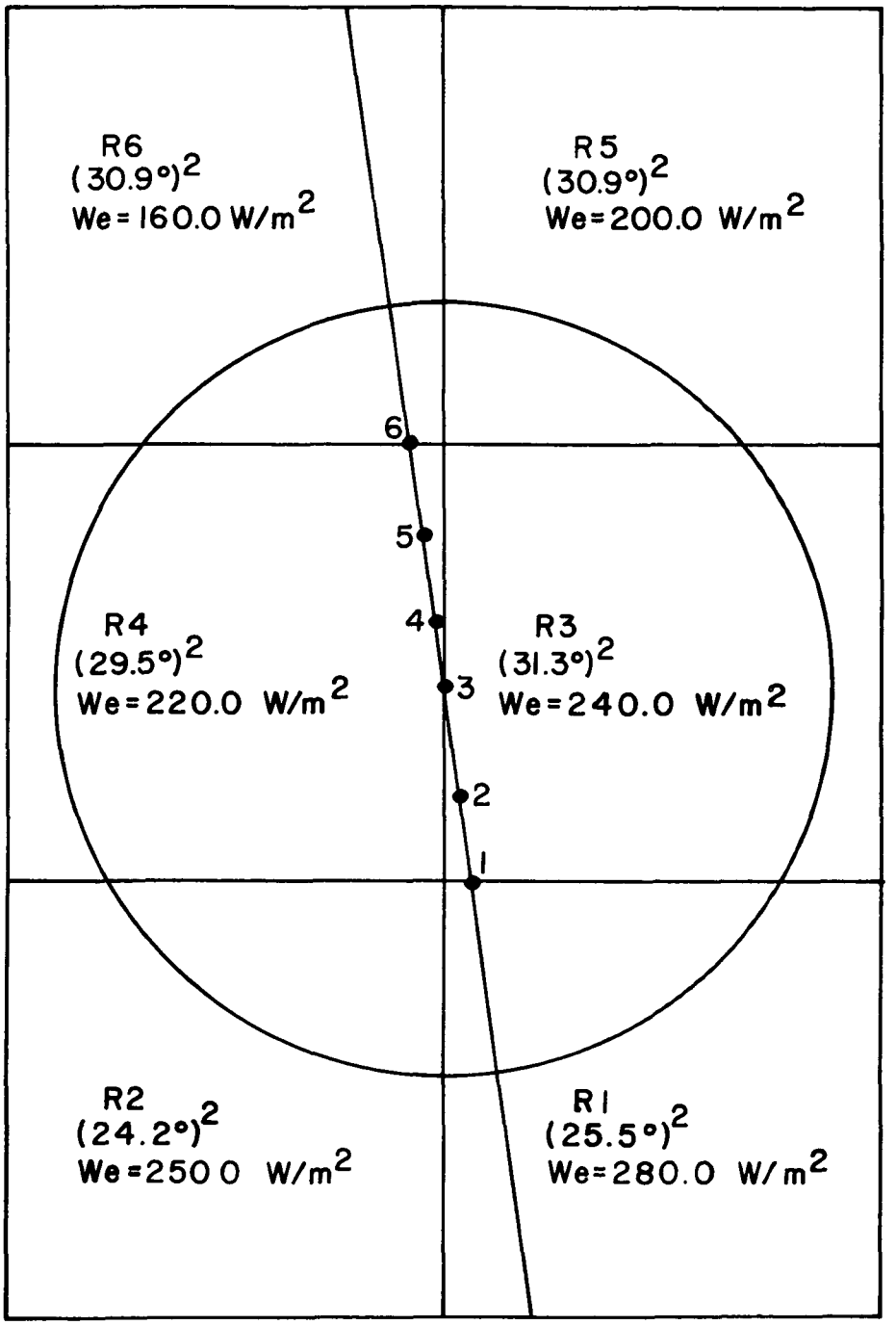

Figure 4-2. Schematic of the Six Regions Observed During a Satellite Pass. The Identifying Numbers and the Equivalent Areas in Degrees of the Regions Are Shown, as well as the Six Subsatellite Points of the Observations. The FOV of the 3rd Observation Is also Shown.

F(J,1)	F(J,2)	F(J,3)	F(J,4)	F(J,5)	F(J,6)
0.212113193	0.065613804	0.631108540	0.156734026	0.000000000	0.000000000
0.047512797	0.026244695	0.731140993	0.258814514	0.000573998	0.000842470
0.009241482	0.007008711	0.680025671	0.356083956	0.005278446	0.008789704
0.000879448	0.000949956	0.510201435	0.487663243	0.021139950	0.044623274
0.000000000	0.000000000	0.286157522	0.528171128	0.056825754	0.194298827
0.000000000	0.000000000	0.107484385	0.265272705	0.107535171	0.586177329

F(J,1)	F(J,2)	F(J,3)	F(J,4)	F(J,5)	F(J,6)
0.142034123	0.038266775	0.507402557	0.102109397	0.000000000	0.000000000
0.025353983	0.013638843	0.579847085	0.169588717	0.000264010	0.000387740
0.004430432	0.003350071	0.533391963	0.243683062	0.002501058	0.004205418
0.000405171	0.000437742	0.387527735	0.366841137	0.010673015	0.023734909
0.000000000	0.000000000	0.202499094	0.427337623	0.031376080	0.128678132
0.000000000	0.000000000	0.066395811	0.188571404	0.062680970	0.473902060

Figure 4-3. Original ill-conditioned configuration factor matrices for a spherical radiometer (above) and a horizontal plate radiometer (below). (LDF included)

Eqs.(4-18c) and (4-20) through (4-24) will be used to generate the results and in order to facilitate references to them, they are rewritten and renumbered here in the same order

$$F\ \{We\} = \{P\} \tag{4-30}$$

$$F^{-1}\ \{P\} = \{We\} \tag{4-31}$$

$$F^{-1}\ \{P'\} = F^{-1}\ \{P + \delta P\} = \{We'\} = \{We + \delta We\} \tag{4-32}$$

$$F^{-1}\ \{\delta P\} = \{\delta We\} \tag{4-33}$$

$$F_{wc}^{-1}\ \{P\} = \{We^{(1)}\} = \{We + \delta We'\} \tag{4-34}$$

$$F_{wc}^{-1}\ \{P'\} = F_{wc}^{-1}\ \{P + \delta P\} = \{We''\} = \{We + \delta We''\} \tag{4-35}$$

The six power measurements made by each radiometer are obtained by operating on the {We} matrix with the matrices F for the sphere and plate according to Eq.(4-30). The resulting power column matrices for both radiometers are presented in Table 4-1.

Table 4-1. Power column matrices {P} obtained for the sphere and plate radiometers.

Observation no.	Power matrix elements P (W) Sphere	Plate
1	261.742680435	193.576929315
2	252.527383060	187.096484378
3	248.346466037	184.875462069
4	241.585706241	179.866778485
5	227.328416581	169.477776668
6	199.451654369	145.781227143

The power matrix elements in Table 4-1 are exact values, that is, they do not contain observational uncertainties. Therefore, when the inverses of the matrices in Figure 4-3 were multiplied with the corresponding power matrices $\{P\}$ of Table 4-1 according to Eq. (4-31), the column matrix $\{We\}$ was obtained. The values of We calculated matched the original We values in Figure 4-2 to at least six decimal places. This type of accuracy indicates that no computational errors are introduced by the subroutine used to carry out the matrix inversions.

The next step was to investigate the effects that observational errors have upon the results. This was done by simulating thirty sets of power measurements by each of the radiometers from the six observation points shown in Figure 4-2.

In order to simulate the power measurements, the exact power values P listed in Table 4-1 were perturbed with the following three types of instrumental errors δP: a) Gaussian random, b) systematic, c) combinations of Gaussian and systematic. The Gaussian random errors had a sigma value of 0.5 W, while the systematic errors ranged from -0.9 to 0.9 W. Ten sets of power measurements were simulated for each of the above three types of errors for each radiometer. The resulting perturbed powers $P' = P + \delta P$ were used to construct the new power column matrices $\{P'\} = \{P + \delta P\}$ for each set of six measurements and for both radiometers. These matrices were operated on by the inverse matrices F^{-1} (which are the inverses of the matrices in Figure 4-3) according to Eq. (4-32).

The resulting δWe errors for each of the six regions for all sets of observations and for both radiometers were used to compute rms's of these errors. These rms's are shown in lines 1, 3, and 5

of Table 4-2 for the sphere, and of Table 4-3 for the plate. From line #3 in these two tables, one sees that the systematic power uncertainties do not produce large δWe errors since the largest error found in this line is 1.4 W/m^2. However, from lines #1 and #5 of the same tables, it is clear that Gaussian random power uncertainties are highly magnified by the inverse matrices F^{-1} of both radiometers.

For example, regions 2 and 5 have rms errors of 158.6 and 269.1 W/m^2, respectively, for the sphere (Table 4-2). The same two regions have rms errors of 215.4 and 293.2 W/m^2, respectively, for the plate (Table 4-3). Only the rms's of the δWe errors of region 3 in these two lines (lines #1 and #5) have rms errors below 15 W/m^2 which is considered the limit of acceptability as discussed previously. Hence, it is concluded that the original matrices F of both radiometers are ill-conditioned.

Application of the stabilization technique to the two original matrices resulted in the two well-conditioned matrices shown in Figure 4-4. The optimum cut-off values found for stabilizing the matrices are 0.032 for the sphere and 0.016 for the plate. Comparisons of the elements of the original matrices in Figure 4-3 with those of the corresponding well-conditioned matrices in Figure 4-4 show that all non-diagonal elements lower than the cut-off values have been translated along their corresponding rows and added to the diagonal elements in those rows.

The two new well-conditioned matrices in Figure 4-4 were inverted and the new inverse matrices F_{wc}^{-1} were multiplied with the power column matrices $\{ P' \}$ according to Eq. (4-35). From the new errors $\delta We''$ obtained per this equation new rms errors were calculated for the six

Table 4-2. Rms's of the δWe and δWe" errors obtained with the original and stabilized inverse matrices of a spherical radiometer. (LDF included)

Power uncertainties	Spread	Matrix	Rms's of δWe and δWe" errors (W/m^2)					
			Region 1	Region 2	Region 3	Region 4	Region 5	Region 6
Gaussian random	σ=0.5 W	Original	36.8	158.4	9.1	17.6	269.2	43.5
Gaussian random	σ=0.5 W	Stabilized	15.2	53.7	1.3	1.3	22.7	4.3
Systematic	-.9 to .9 W	Original	0.5	0.7	0.6	0.6	0.4	0.6
Systematic	-.9 to .9 W	Stabilized	4.9	23.5	0.7	0.6	5.7	0.9
Gaussian random plus Systematic	σ=0.5 W 0.9 W	Original	36.7	158.6	8.9	17.9	269.1	43.7
		Stabilized	14.8	54.1	1.1	1.7	22.7	4.4

Table 4-3. Rms's of the δWe and δWe" errors obtained with the original and stabilized inverse matrices of a horizontal plate satellite radiometer. (LDF included)

Power uncertainties	Spread	Matrix	Rms's of δWe and δWe" errors (W/m^2)					
			Region 1	Region 2	Region 3	Region 4	Region 5	Region 6
Gaussian random	σ=0.5 W	Original	46.8	215.2	6.5	13.9	293.3	34.7
Gaussian random	σ=0.5 W	Stabilized	22.1	88.9	1.4	1.8	42.3	5.7
Systematic	-.9 to .9 W	Original	0.6	1.4	0.8	0.8	0.2	0.8
Systematic	-.9 to .9 W	Stabilized	3.8	21.0	0.7	0.7	5.7	0.7
Gaussian random plus Systematic	σ=0.5 W 0.9 W	Original	46.6	215.4	6.4	14.2	293.2	35.1
		Stabilized	21.8	89.3	1.4	2.3	42.2	5.9

F(J,1)	F(J,2)	F(J,3)	F(J,4)	F(J,5)	F(J,6)
0.212113193	0.065613804	0.631108540	0.156734026	0.000000000	0.000000000
0.047512797	0.027661162	0.731140993	0.258814514	0.000000000	0.000000000
0.000000000	0.000000000	0.710344014	0.356083056	0.000000000	0.000000000
0.000000000	0.000000000	0.510201435	0.510632598	0.000000000	0.044623274
0.000000000	0.000000000	0.286157522	0.528171128	0.056825754	0.194298827
0.000000000	0.000000006	0.107484385	0.265272705	0.107535171	0.586177329

F(J,1)	F(J,2)	F(J,3)	F(J,4)	F(J,5)	F(J,6)
0.142034123	0.038266775	0.507402557	0.102109397	0.000000000	0.000000000
0.025353983	0.014290592	0.579847085	0.169588717	0.000000000	0.000000000
0.000000000	0.000000000	0.547878943	0.243683062	0.000000000	0.000000000
0.000000000	0.000000000	0.387527735	0.378357066	0.000000000	0.023834909
0.000000000	0.000000000	0.202499094	0.427337623	0.031376080	0.128678132
0.000000000	0.000000000	0.066395811	0.188571404	0.062680970	0.473902060

Figure 4-4. Well-conditioned configuration factor matrices for a spherical radiometer (above) and a horizontal plate radiometer (below). (LDF included)

regions and for both radiometers. These new rms's appear in lines 2,4, and 6 of Table 4-2 for the sphere and of Table 4-3 for the plate.

Comparisons of the rms values in line #2 with those in line #1, and those of line #6 with those of line #5, clearly show the dramatic decrease caused by the stabilized matrices in the rms errors derived totally or partially from Gaussian power uncertainties. For example, region 4 went from 17.9 to 1.7 W/m^2 for the sphere (Table 4-2, lines 5 and 6), while this same region decreased from 14.2 to 2.3 W/m^2 for the plate (Table 4-2, lines 5 and 6).

However, it is also noted that the new rms values of regions 3, 4, and 6 are much lower than those of regions 1, 2, and 5 whose rms errors are unacceptable. For instance, regions 1, 2, and 5 have rms values of 21.8, 89.3, and 42.2 W/m^2 in line #6 of Table 4-3; in the same line and table, regions 3, 4, and 6 have rms values of 1.4, 2.3, and 5.9 W/m^2, respectively. The last three values are all acceptable (lower than the acceptable limit of 15 W/m^2), while the rms values of regions 1, 2, and 5 are not.

Comparison of the rms's in lines #3 and #4 of Tables 4-2 and 4-3 show that the stabilized matrices have increased significantly the rms errors of regions 1, 2, and 5. Region 2, for example, went from 0.7 to 23.5 W/m^2 in Table 4-2, while it increased from 1.4 to 21.0 W/m^2 in Table 4-3. However, these increases have no significance since as will be shown later, regions 1, 2, and 5 should be disregarded according to the results of the prediction scheme. On the other hand, the rms errors of regions 3, 4, and 6 (whose results are considered acceptable by the prediction scheme, as will be demonstrated later) are less than 1 W/m^2 in every instance, as can be seen from the rms

values of these regions shown in lines #3 and #4 of Tables 4-2 and 4-3.

Figures 4-5 and 4-6 display the dramatic contrast between the curves of the rms's of the $\delta We''$ errors (derived from combinations of Gaussian and systematic uncertainties) obtained with the unstable and stabilized matrices, versus the regional configuration factor S_k of each region for the sphere and plate, respectively. As defined previously, S_k is the sum of the shape factors contributed by the kth region to all six observations; it is referred to as the regional configuration factor of the kth region. These curves are plots of the data displayed in the last two lines of Tables 4-2 and 4-3 previously discussed.

Another way of showing the significant differences between the original ill-conditioned matrices F and the new well-conditioned matrices F_{wc} is by comparison of their condition numbers defined previously. The values of these parameters are compared in Table 4-4 for both radiometers. As seen from the last column, the condition number values dropped from 1087 to 184 for the sphere, and from 945 to 253 for the plate.

The instantaneous technique was also applied to a LWR field which was assumed to be isotropic. Proceeding in the same manner as in the previous case in which a LWR field described by a LDF was treated, rms's of the $\delta We''$ errors obtained with the unstable and stabilized matrices are computed for the sphere and plate. These rms's are displayed in Table 4-5 for the sphere and in Table 4-6 for the plate. Just as in the case of a LDF radiation field, regions 3, 4, and 6 show acceptable results for the three types of power uncertainties

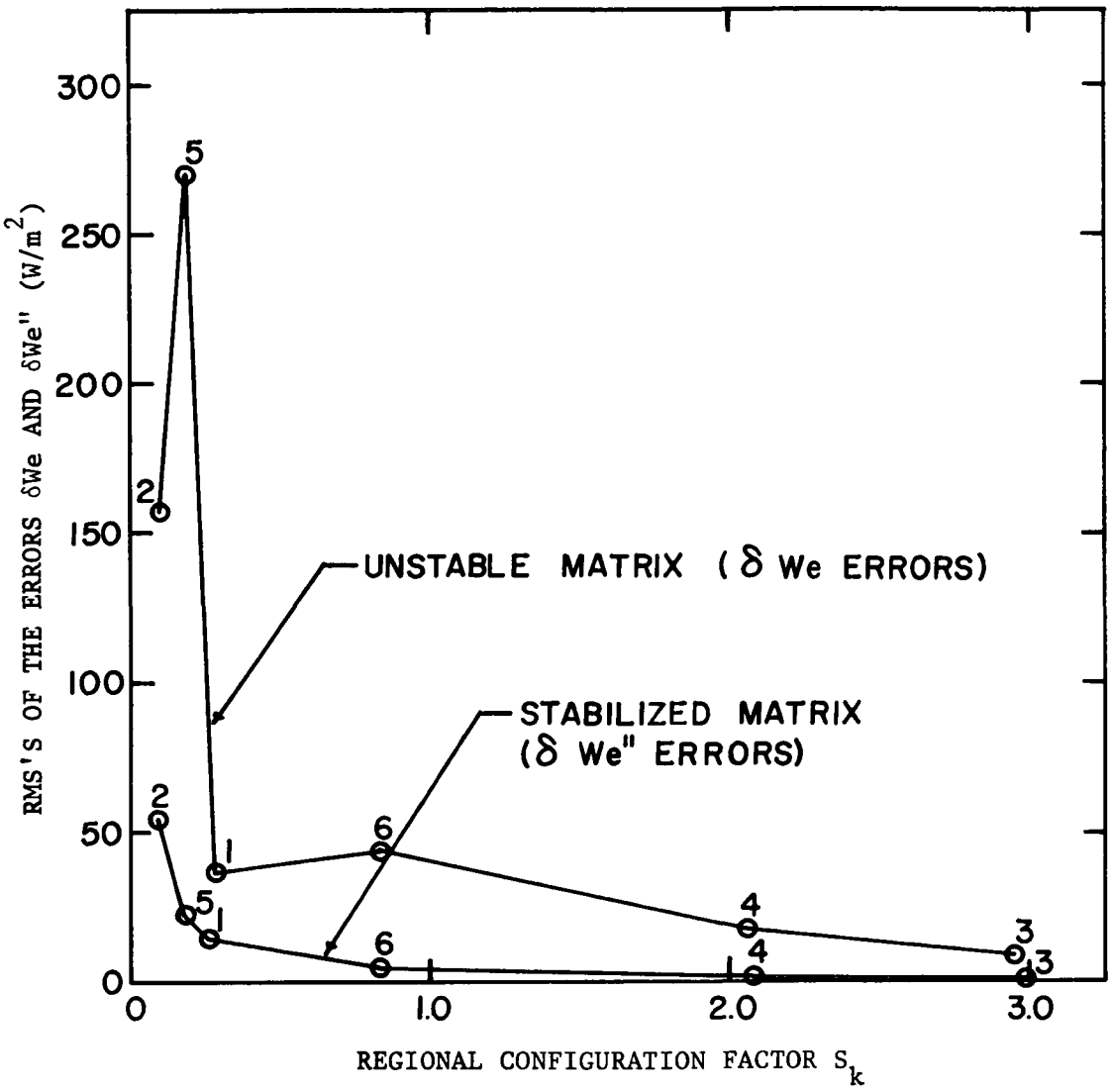

Figure 4-5. Rms's of the Errors δWe and δWe" (Derived from Gaussian and Systematic Uncertainties) for the Six Regions with the Unstable and Stabilized Inverse Matrices of the Spherical Radiometer. (LDF Included)

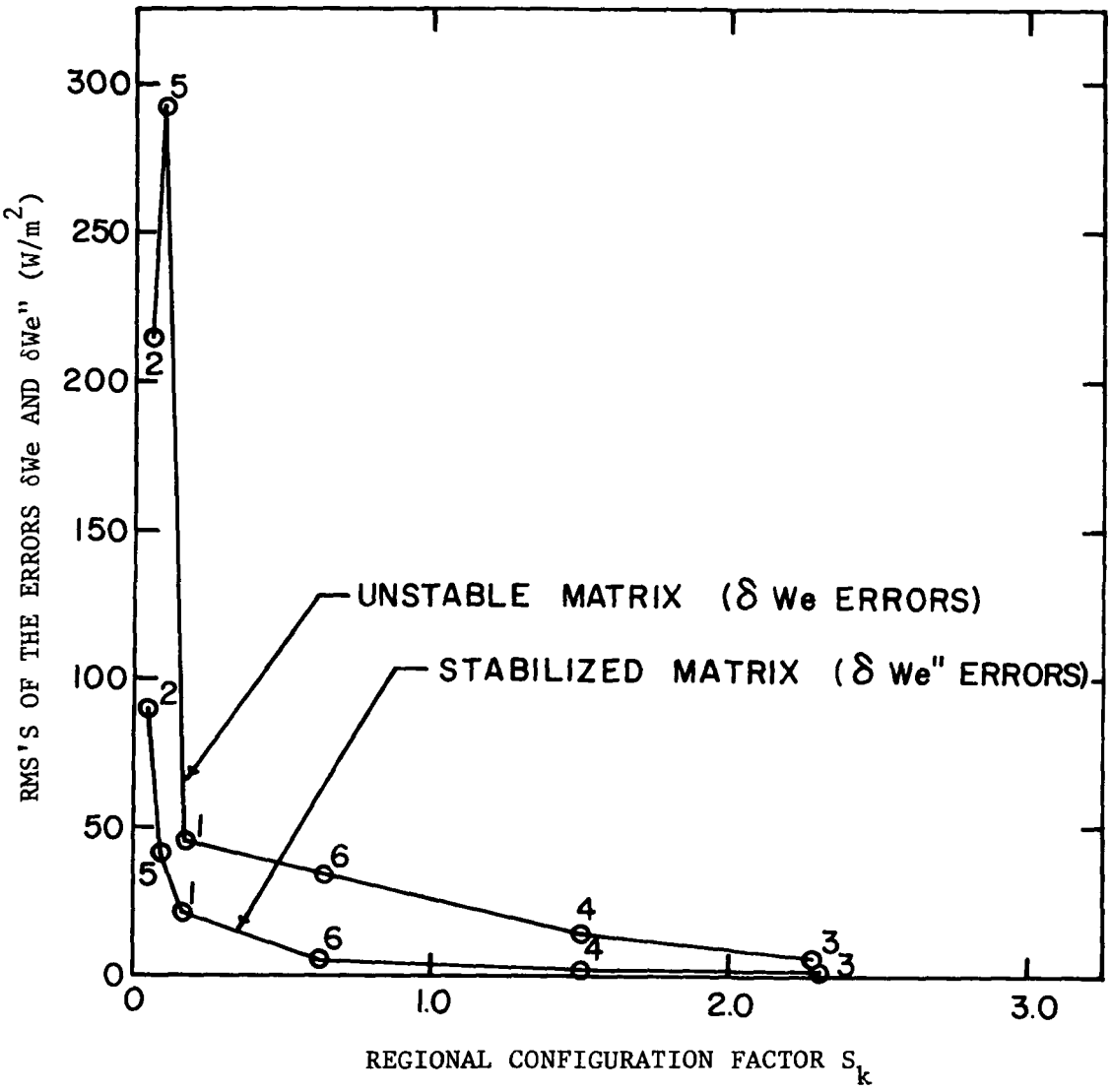

Figure 4-6. Rms's of the Errors δWe and δWe" (Derived from Gaussian and Systematic Uncertainties) for the Six Regions with the Unstable and Stabilized Inverse Matrices of the Horizontal Plate Radiometer. (LDF Included)

Table 4-4. Condition numbers of the original, ill-conditioned and the new, well-conditioned configuration factor matrices for both types of radiometer, spherical and horizontal plate. (LDF included)

Radiometer	Matrix F	Matrix F^TF	Eigenvalues μ of F^TF		Condition number
			μ_{max}	μ_{min}	
Sphere	Original, F	F^TF	2.401393667	0.000002033	1087
Sphere	Well-conditioned, F_{wc}	$F_{wc}^T F_{wc}$	2.452713184	0.000354014	184
Plate	Original, F	F^TF	1.392923372	0.000001559	945
Plate	Well-conditioned, F_{wc}	$F_{wc}^T F_{wc}$	1.412063277	0.000114178	253

Table 4-5. Rms's of the δWe and δWe" errors obtained with the original and stabilized inverse matrices of a spherical radiometer. (Isotropic radiation field)

Power uncertainties	Spread	Matrix	Rms's of δWe and δWe" errors (W/m^2)					
			Region 1	Region 2	Region 3	Region 4	Region 5	Region 6
Gaussian random	σ=0.5 W	Original	38.4	164.1	12.2	23.2	313.8	56.3
Gaussian random	σ=0.5 W	Stabilized	14.4	49.1	1.5	1.3	19.8	4.3
Systematic	-.9 to .9 W	Original	0.6	0.6	0.6	0.6	0.6	0.6
Systematic	-.9 to .9 W	Stabilized	5.2	24.5	0.9	0.7	5.5	0.9
Gaussian random plus systematic	σ=0.5 W 0.9 W	Original	38.2	164.2	12.1	23.4	313.6	56.5
		Stabilized	14.1	49.5	1.1	1.8	19.8	4.4

Table 4-6. Rms's of the δWe and δWe" errors obtained with the original and stabilized inverse matrices of a horizontal plate radiometer. (Isotropic radiation field)

Power uncertainties	Spread	Matrix	Rms's of δWe and δWe" errors (W/m^2)					
			Region 1	Region 2	Region 3	Region 4	Region 5	Region 6
Gaussian random	σ=0.5 W	Original	47.1	211.0	8.2	17.1	316.9	41.9
Gaussian random	σ=0.5 W	Stabilized	20.8	79.2	1.5	1.8	37.2	5.7
Systematic	-.9 to .9 W	Original	0.7	1.1	0.8	0.8	0.5	0.8
Systematic	-.9 to .9 W	Stabilized	4.2	22.3	0.7	0.8	5.4	0.8
Gaussian random plus systematic	σ=0.5 W 0.9 W	Original	47.0	211.3	8.0	17.4	316.7	42.2
		Stabilized	20.5	79.7	1.4	2.3	37.1	5.9

(Gaussian, systematic, and combinations of Gaussian and systematic) and for both radiometers. Figures 4-7 and 4-8 display the curves obtained from the data appearing in the last two rows of Tables 4-5 and 4-6, respectively. These curves are plots of the rms's of $\delta We''$ errors derived from combinations of Gaussian and systematic power uncertainties, versus the value of S_k of each region. Comparison of these curves obtained for an isotropic radiation field with similar curves obtained for a field described by a LDF and displayed in Figures 4-5, and 4-6 show that the stabilization technique produces equally good results in both instances.

The prediction parameter PP was defined by Eq. (4-27) which is here rewritten and renumbered

$$PP = (S_k F_{jj} / \Sigma_j) \times 1000 \qquad (4\text{-}36)$$

Figures 4-9 (sphere) and 4-10 (plate) are curves of the rms errors appearing in the last line of Tables 4-2 and 4-3, respectively, plotted versus the values of PP for the six regions. The rms errors selected are the result of combinations of Gaussian and systematic uncertainties in the power measurements. In both of these figures, regions 3, 4, and 6 show rms values of less than 6 W, while regions 1, 2, and 5 show rms values of about 15 W or greater. The smallest gap in the value of PP between these two groups is at least 300. On the basis of results soon to be presented, cut-off values of 150 for the sphere and 100 for the plate were selected to separate the two groups of regions, those that are predicted acceptable and those that are not. Hence, according to the prediction parameter PP, only the results obtained for regions 3, 4, and 6 are to be considered acceptable. The results for regions 1, 2, and 5 are to be considered

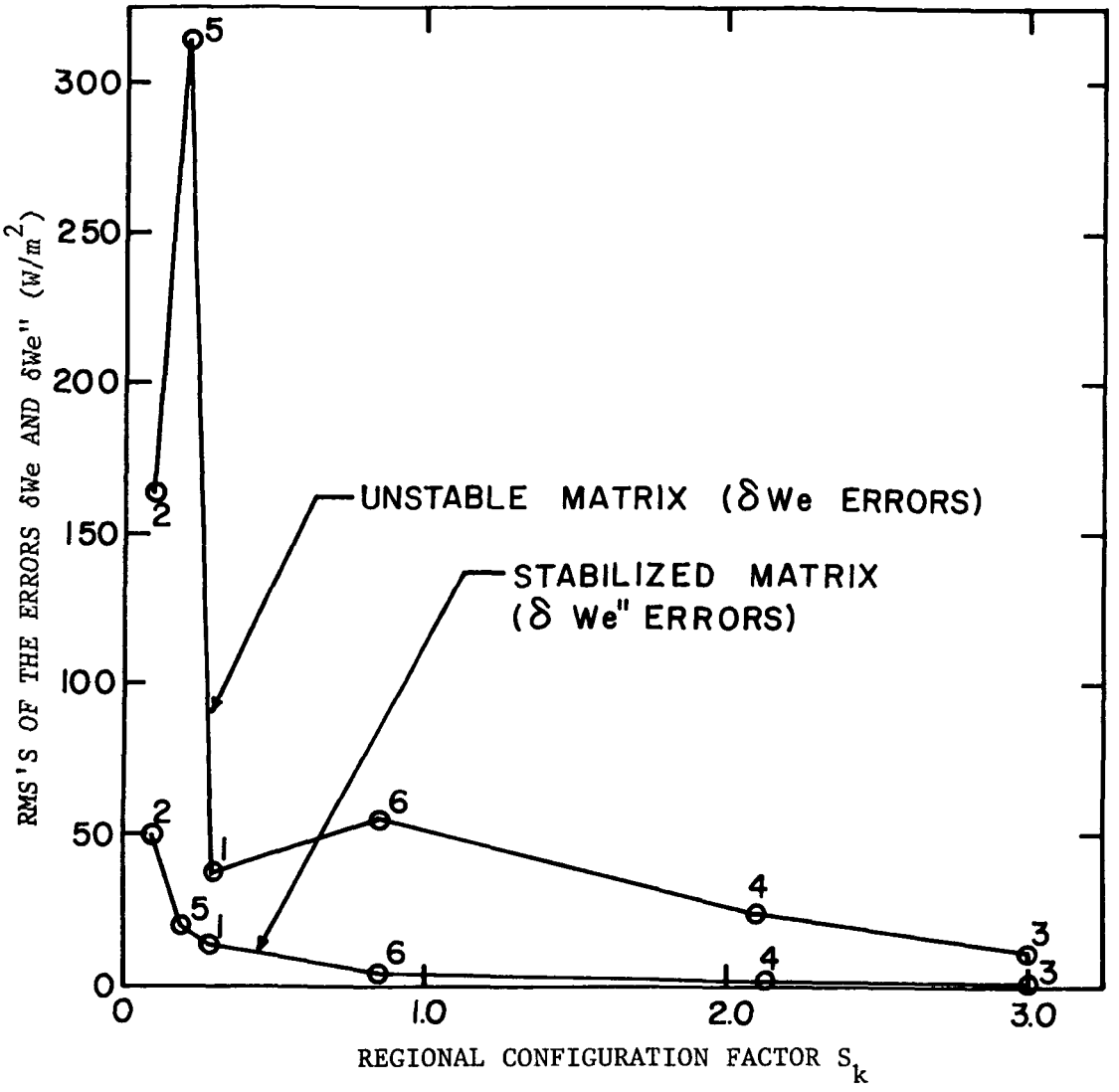

Figure 4-7. Rms's of the Errors δWe and δWe'' (Derived from Combinations of Gaussian and Systematic Uncertainties) Obtained for the Six Regions with the Unstable and Stabilized Inverse Matrices of the Spherical Radiometer. (Isotropic Radiation Field)

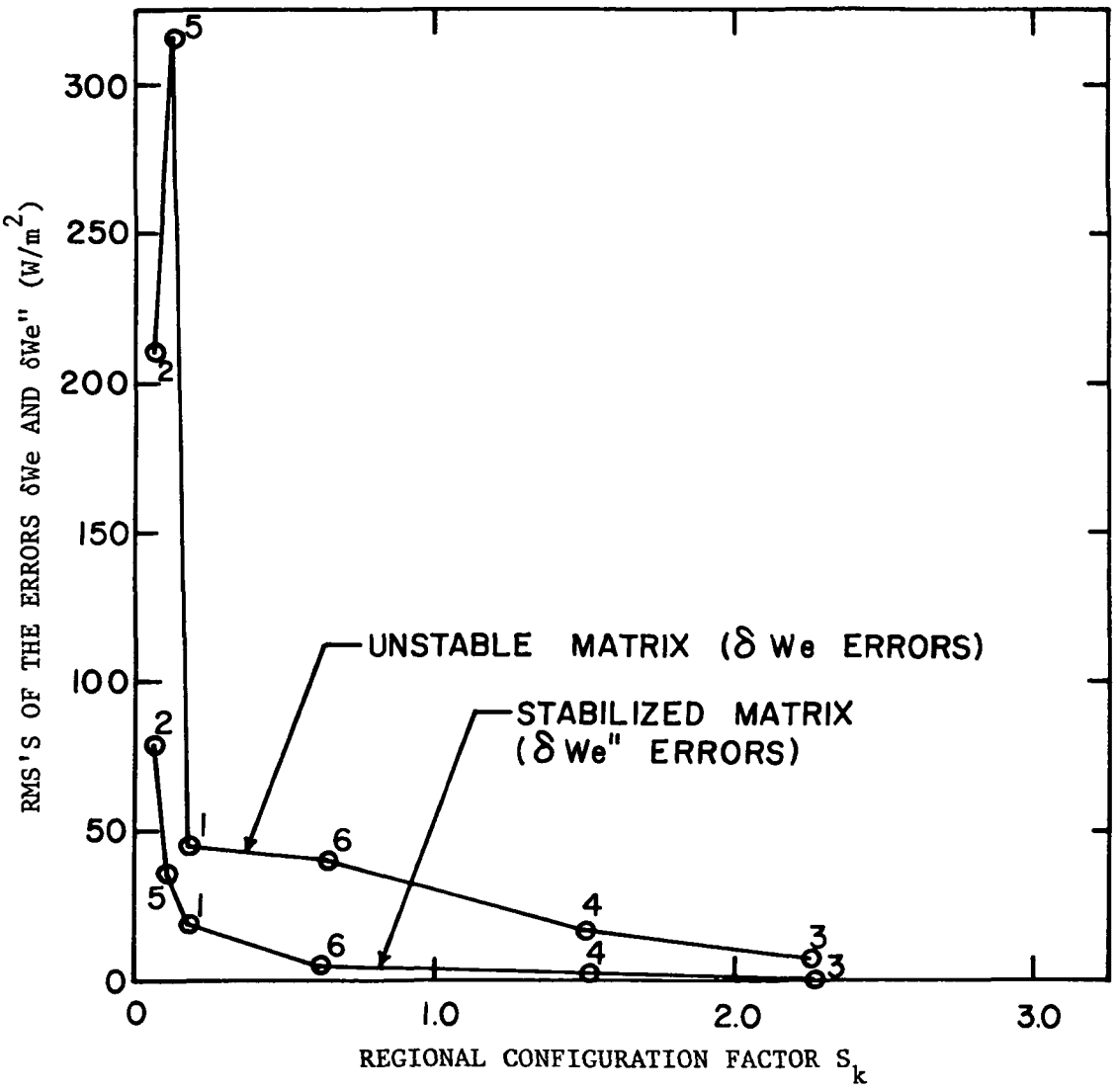

Figure 4-8. Rms's of the Errors δWe and δWe" (Derived from Combinations of Gaussian and Systematic Uncertainties) Obtained for the Six Regions with the Unstable and Stabilized Inverse Matrices of a Horizontal Plate Radiometer. (Isotropic Radiation Field)

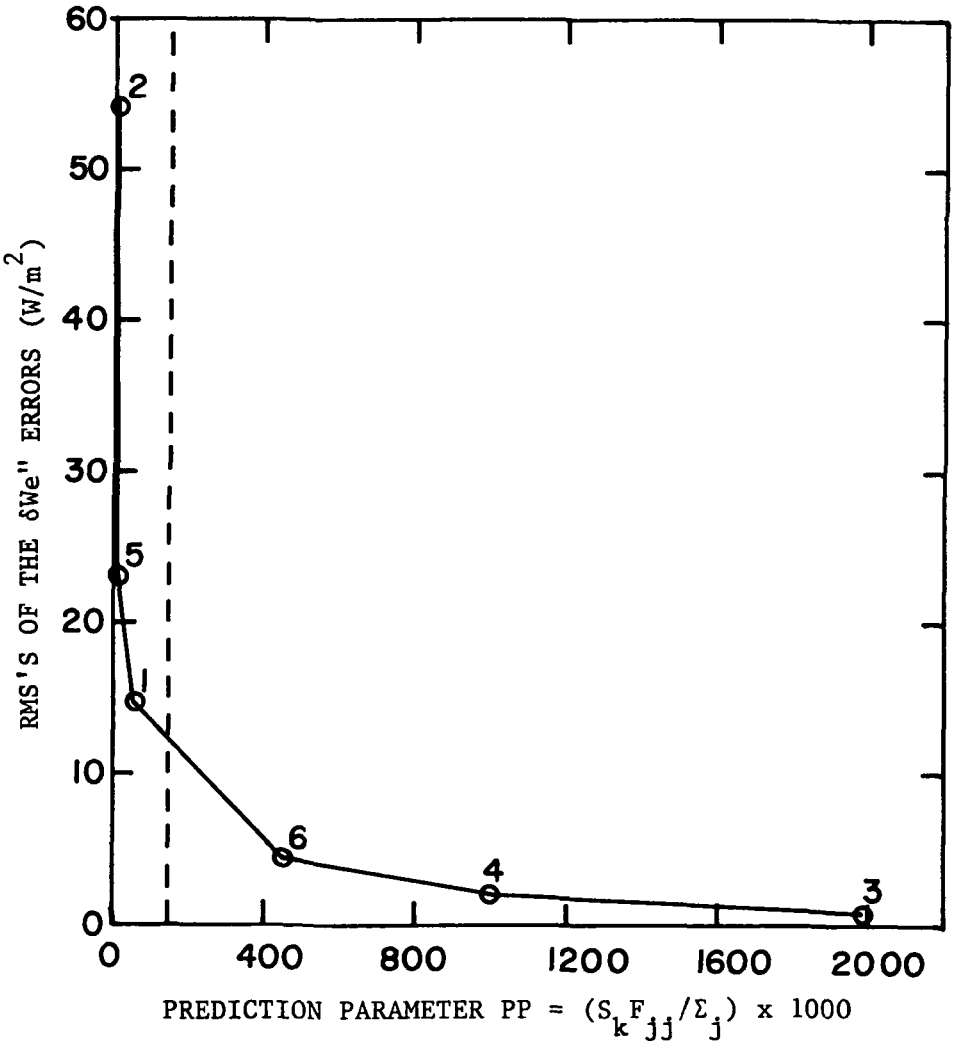

Figure 4-9. Curve Showing the Relationship between the Prediction Parameter and the Rms's of the δWe" Errors Obtained with the Stabilized Inverse Matrix of a Spherical Radiometer. (LDF Included)

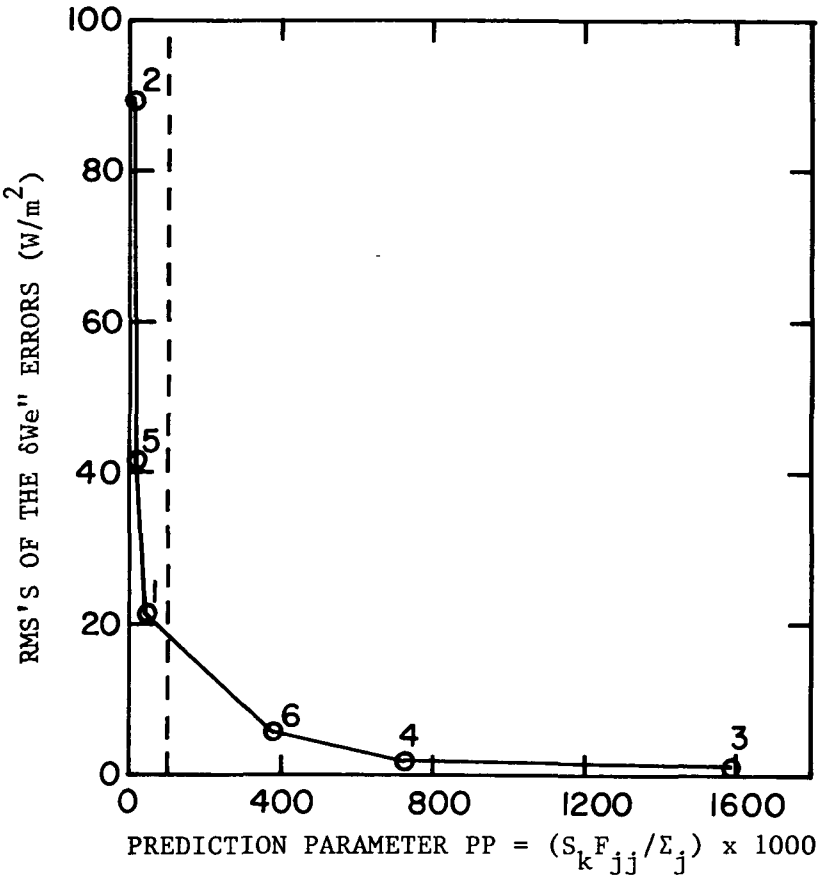

Figure 4-10. Curve Showing the Relationship between the Prediction Parameter and the Rms's of the δWe" Errors Obtained with the Stabilized Inverse Matrix of a Horizontal Plate Radiometer. (LDF Included)

unacceptable as a result of insufficient data gathered from these regions. Data from different satellite observations which include larger portions of the regions under discussion yield acceptable results for these regions as will be shown.

Figures 4-11 and 4-12 show curves for the isotropic case similar to those shown in Figures 4-9 and 4-10 for the LDF case. The rms's of the δWe" errors used in Figure 4-11 (sphere) and 4-12 (plate) are those presented in the last row of Tables 4-5 and 4-6, respectively, which are the result of Gaussian and systematic power uncertainties. From these figures, it is seen that the PP cut-off values of 150 for the sphere and 100 for the plate clearly separate the regions 1, 2, and 5 (rejectable) from regions 3, 4, and 6 (acceptable) exactly as in the LDF case.

As indicated previously, it became necessary to develop the matrix stabilization and prediction techniques to be used in conjunction with the instantaneous technique only because the sections observed of some of the regions were too small. In other words, if the satellite positions were such that sufficiently large portions of all regions are observed, the results obtained with the original matrices would be acceptable. To prove this contention, satellite positions were selected such that the FOV's covered all the regions sufficiently. The results are displayed in Tables 4-7 and 4-8. From rows 1, 3, and 5 of these tables, it is seen that the rms's of the δWe" errors obtained with the original matrices are all acceptable. The largest rms value found in these rows is 3.6 W/m^2 for region 2. Furthermore, application of the stabilization technique to both of the original matrices produced only slight improvements as can be seen from the

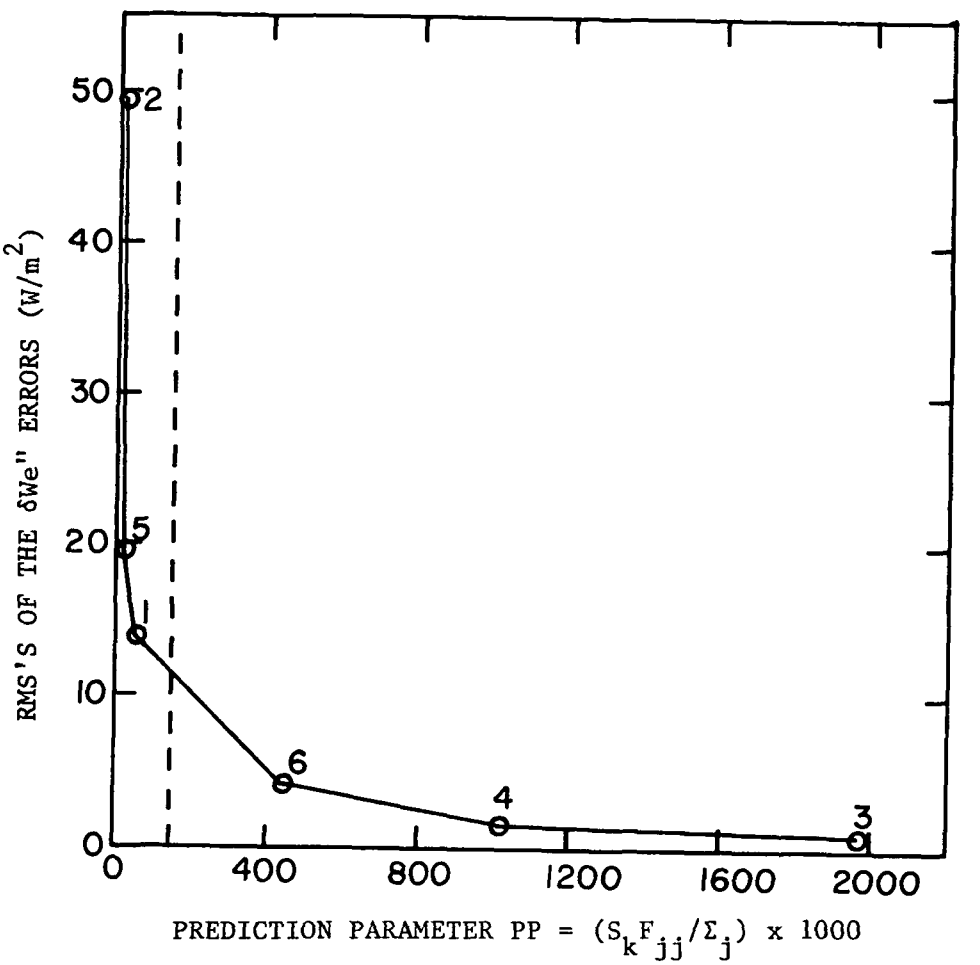

Figure 4-11. Curve Showing the Relationship between the Prediction Parameter and the Rms's of the δWe" Errors Obtained with the Stabilized Inverse Matrix of a Spherical Radiometer. (Isotropic Radiation Field)

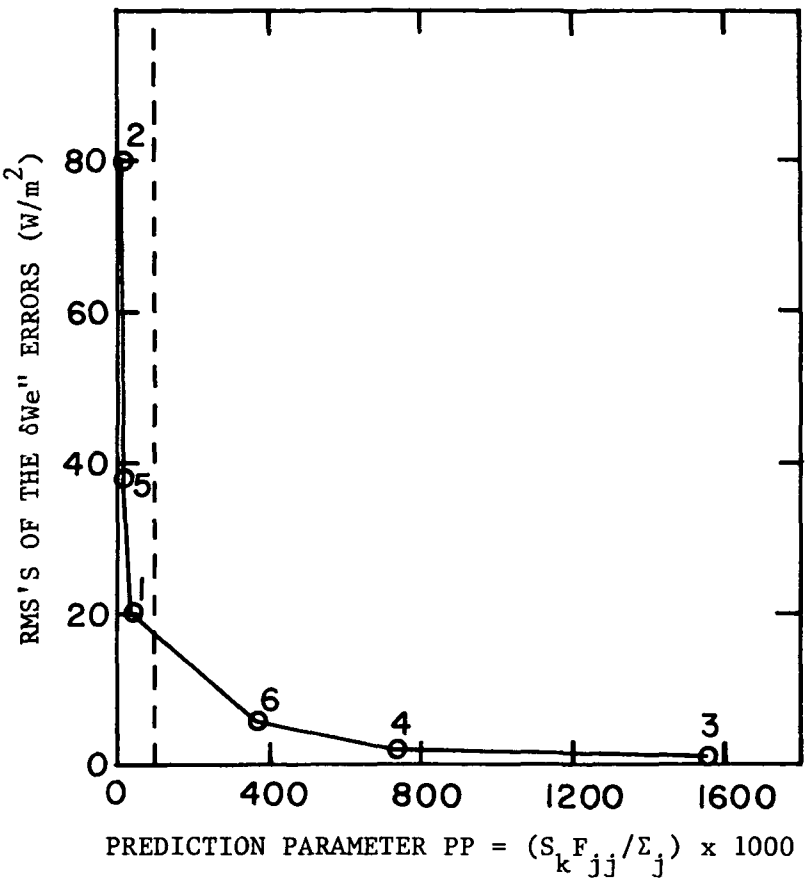

Figure 4-12. Curve Showing the Relationship between the Prediction Parameter and the Rms's of the δWe" Errors Obtained with the Stabilized Inverse Matrix of a Horizontal Plate Radiometer. (Isotropic Radiation Field)

Table 4-7. Rms's of the δWe and δWe" errors obtained with the original and stabilized inverse matrices of a spherical radiometer. Adequate portions of all regions are observed by judicious selection of satellite positions. (LDF included)

Power uncertainties	Spread	Matrix	Rms's of δWe and δWe" errors (W/m^2)					
			Region 1	Region 2	Region 3	Region 4	Region 5	Region 6
Gaussian random	σ=0.5 W	Original	2.0	3.0	1.6	2.4	1.1	1.1
Gaussian random	σ=0.5 W	Stabilized	1.8	2.6	1.6	2.1	1.1	1.0
Systematic	-.9 to .9 W	Original	0.6	0.6	0.6	0.6	0.6	0.6
Systematic	-.9 to .9 W	Stabilized	1.1	0.5	0.6	0.5	0.8	0.6
Gaussian random plus systematic	σ=0.5 W 0.9 W	Original	2.0	3.0	1.7	2.7	1.4	1.2
		Stabilized	2.1	2.6	1.3	2.4	1.6	1.2

Table 4-8. Rms's of the δWe and δWe" errors obtained with the original and stabilized inverse matrices of a horizontal plate radiometer. Adequate portions of all regions are observed by judicious selection of satellite positions. (LDF included)

Power uncertainties	Spread	Matrix	Rms's of δWe and δWe" errors (W/m^2)					
			Region 1	Region 2	Region 3	Region 4	Region 5	Region 6
Gaussian random	σ=0.5 W	Original	2.4	3.6	1.7	2.8	1.2	1.2
Gaussian random	σ=0.5 W	Stabilized	2.2	3.2	1.6	2.5	1.1	1.1
Systematic	-.9 to .9 W	Original	0.8	0.8	0.8	0.8	0.8	0.8
Systematic	-.9 to .9 W	Stabilized	1.0	0.8	0.7	0.7	0.9	0.8
Gaussian random plus systematic	σ=0.5 W 0.9 W	Original	2.4	3.6	2.0	3.2	1.6	1.5
		Stabilized	2.3	3.3	1.6	2.9	1.7	1.4

results shown in rows 2, 4, and 6 of the same tables. For example, the highest rms value of 3.6 W/m^2 for region 2 mentioned previously, decreased to 3.3 W/m^2 (Table 4-8, lines #5 and #6).

Since all the results displayed in Tables 4-7 and 4-8 are considered acceptable, the data in the last row of these tables were plotted versus the PP values of the regions in Figures 4-13, and 4-14, respectively. It is seen from these figures that all the results lie above 150 for the sphere, and above 100 for the plate. These cut-off values were therefore selected as the lowest PP values that a region must have in order for its results to be considered acceptable. These cut-off values were shown in Figures 4-9 and 4-10 for the LDF case, and in Figures 4-11 and 4-12 for the isotropic case.

The effects caused by improper selection of an angular function to describe the LWR field during data interpretation were investigated. Following is a description of the two cases studied.

In one case, the simulated power measurements of a radiation field described by a LDF were computed by using configuration factor matrices that included this LDF. The resulting exact powers are those presented in Table 4-1 for a LDF field. The perturbed powers were the same powers generated for the LDF case discussed previously and whose results were presented in Tables 4-2 and 4-3. However, those results were obtained by using the correct LDF during interpretation of the data. In this study, on the other hand, the radiation field is assumed isotropic when interpreting the data. This case, in which a LWR field described by a LDF is assumed ISOTROPIC during data evaluation will be termed LDF/ISO. The results obtained for this case with the stabilized matrix of a spherical radiometer are

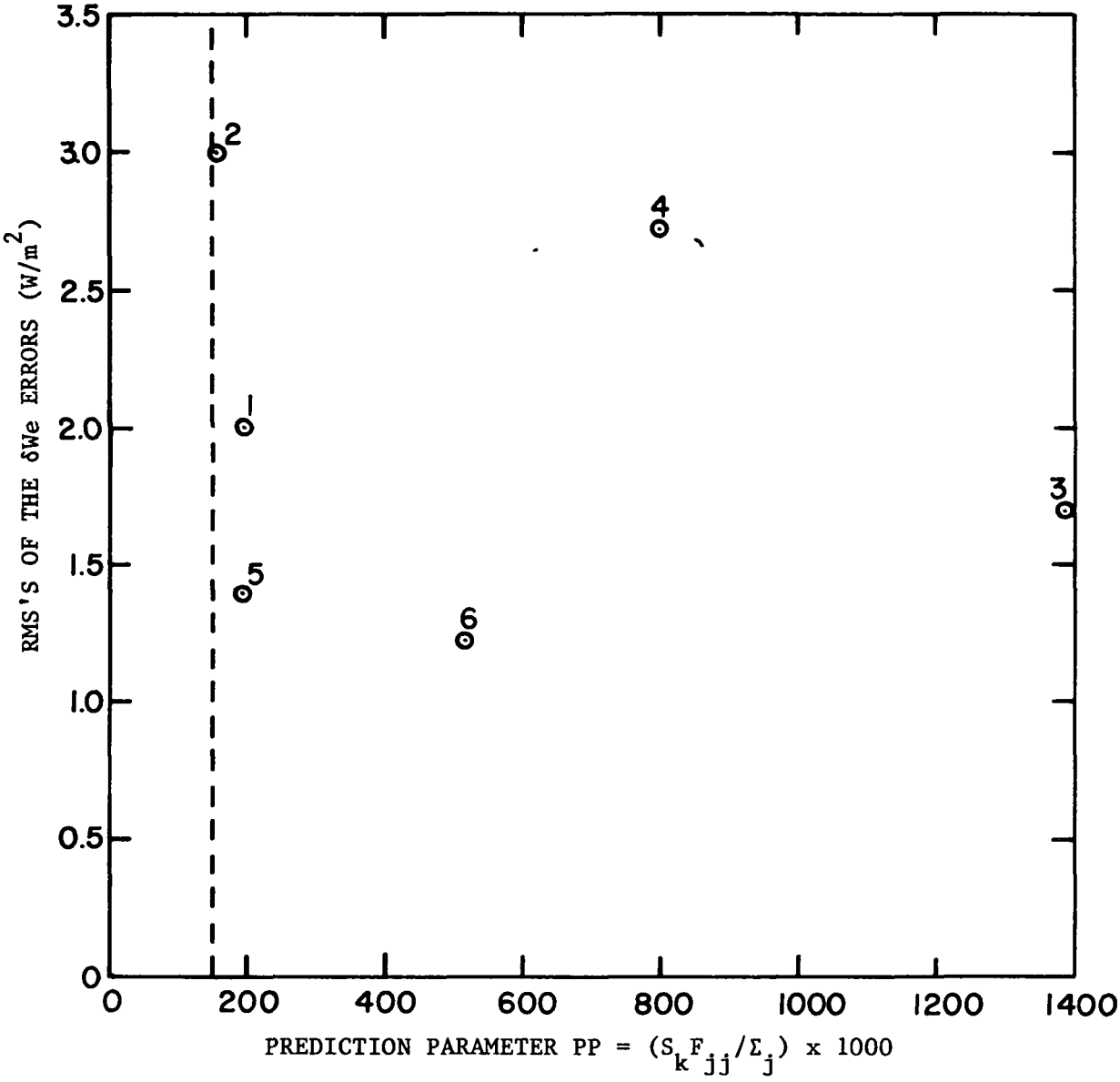

Figure 4-13. Relationship between the Prediction Parameter and the Rms's of the δWe Errors Obtained with the Inverse of the Original Matrix of a Spherical Radiometer. Adequate Portions of All Regions Are Observed by Judicious Selection of Satellite Positions. (LDF Included)

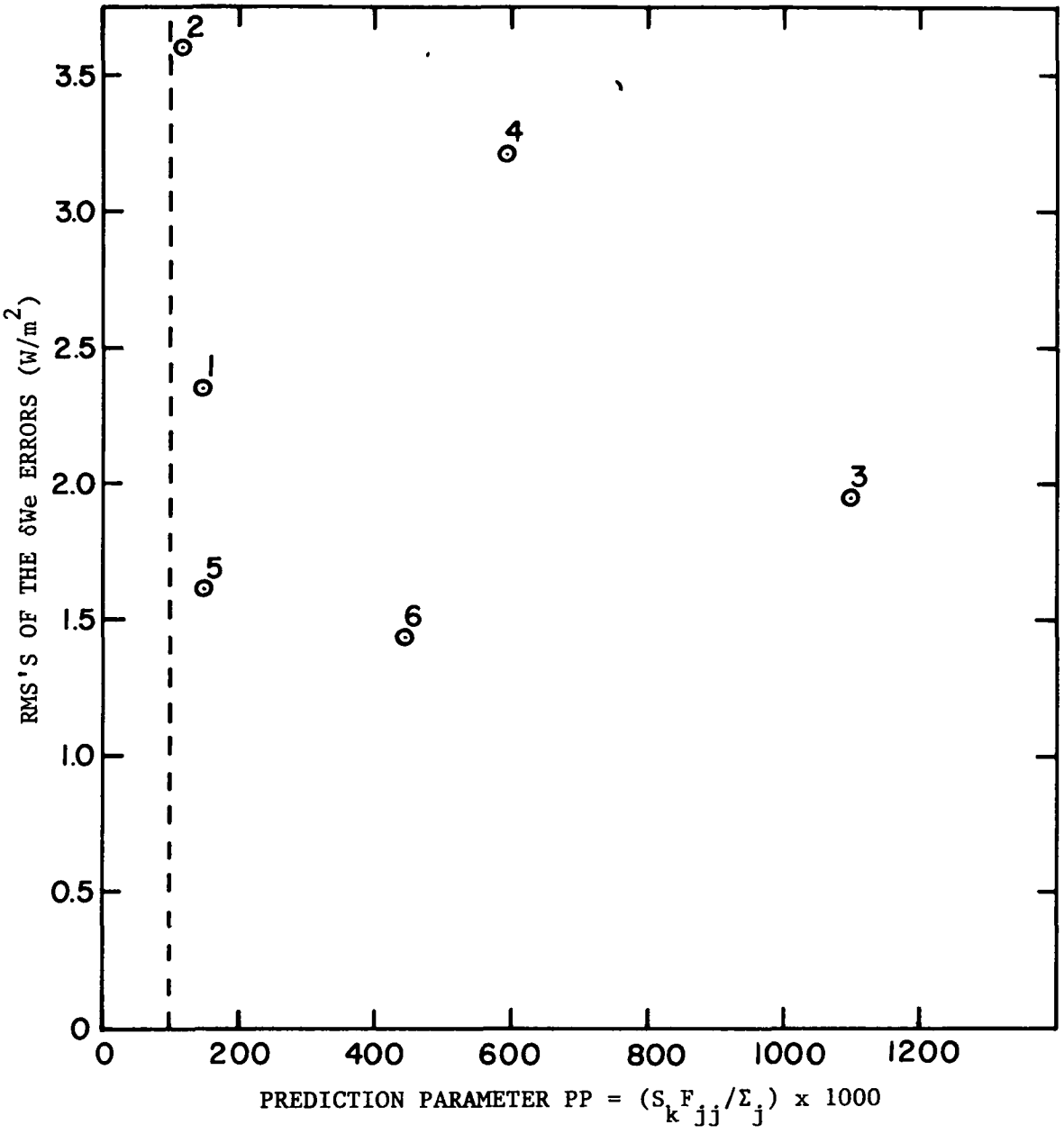

Figure 4-14. Relationship between the Prediction Parameter and the Rms's of the δWe Errors Obtained with the Inverse of the Original Matrix of a Horizontal Plate Radiometer. Adequate Portions of All Regions Are Observed by Judicious Selection of Satellite Positions. (LDF Included)

presented in Table 4-9. As in the two previous cases (LDF and isotropic) where the correct angular function of the field was used during data interpretation, regions 3, 4, and 6 have acceptable results when Gaussian power uncertainties are used either totally (row 1), or partially (row 3). The largest rms error is found in region 6, line #1. This rms error is 8 W/m^2 which is below the acceptable limit (15 W/m^2). The results obtained when systematic power uncertainties only are used (row 2) show that this type of error is not highly magnified. The rms error in this row for columns 3, 4, and 6 are 4.8, 1.8, and 7.5 W/m^2, respectively.

The prediction scheme was applied to this case and the results are similar to those obtained in the previous cases (LDF and isotropic). A plot of the rms's of the $\delta We''$ errors versus the prediction parameter PP for the six regions is shown in Figure 4-15. The rms's used in this figure are those appearing in the last row of Table 4-9 just discussed. As seen from Figure 4-15, where the prediction parameter cut-off value (broken line) previously selected for the sphere is shown, it is predicted that regions 3, 4, and 6 are to have acceptable results while those of regions 1, 2, and 5 should be considered unreliable for lack of sufficient data. This prediction agrees with the rms values in this curve.

In the other case studied, three regions were assumed to have a LWR field described by a LDF while the remaining three regions were assumed to radiate isotropically. However, when interpreting the data, the radiation field was assumed <u>entirely isotropic</u>. This case will be referred to as LDF-ISO/ISO. The rms's of the $\delta We''$ errors obtained with the stabilized matrix of the spherical radiometer

Table 4-9. Rms's of the δWe" errors obtained when the stabilized inverse matrix of a spherical radiometer which was derived for an isotropic radiation field was then applied to an anisotropic field. (Uncertainties in power measurements are included)

Power uncertainties	Spread	Rms's of δWe" errors (W/m^2)					
		Region 1	Region 2	Region 3	Region 4	Region 5	Region 6
Gaussian random	σ=0.5 W	14.2	41.0	5.2	2.2	20.5	8.0
Systematic	-.9 to .9 W	4.7	0.9	4.8	1.8	11.1	7.5
Combination of Gaussian random and systematic	σ=0.5 W 0.9 W	13.8	41.0	4.5	1.7	20.7	7.4

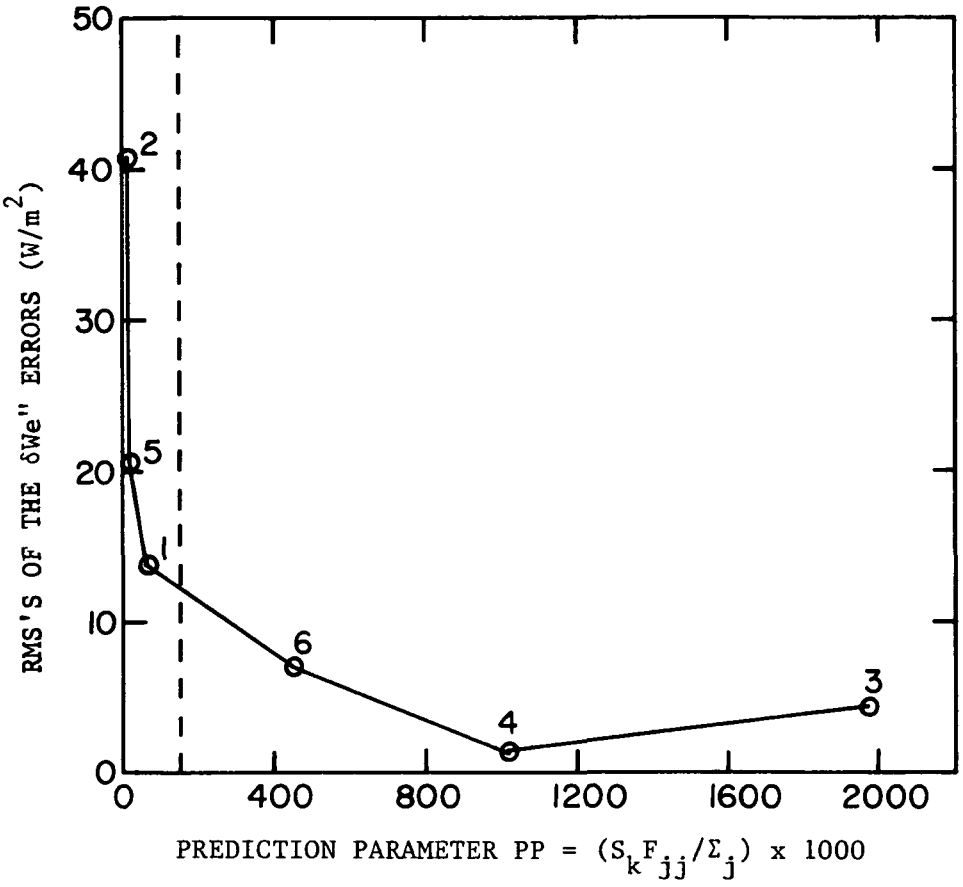

Figure 4-15. Curve Showing the Relationship between the Prediction Parameter and the Rms's of the δWe" Errors Obtained with the Stabilized Inverse Matrix of a Spherical Radiometer Which Was Derived for an Isotropic Radiation Field and Then Applied to an Anisotropic Field.

are displayed in Table 4-10. As can be seen from the three rows of data, all the results for regions 3, 4, and 6 are acceptable, just as in all previous cases considered. The highest rms value is 4.1 W/m^2 for region 6 in lines #1 and #3. The data shown in the last row of this table are plotted versus the region's prediction parameter values in Figure 4-16. The value of PP = 150 (the vertical broken line) is included in this figure to indicate that the three regions to the right (regions 3, 4, and 6) are predicted to have acceptable results, while the results of the three regions to the left (regions 1, 2, and 5) are to be considered unreliable for lack of sufficient data from these regions. The rms errors shown in this figure agree with these predictions.

The rms's of the δWe" errors obtained for the three regions (R3, R4, and R6) that passed the prediction technique test, for the case of a spherical radiometer are presented in Table 4-11 for the following four cases:

1. LDF/LDF: A LDF field is interpreted as a LDF field.
2. ISO/ISO: An isotropic field is interpreted as an isotropic field.
3. LDF/ISO: A LDF field is interpreted as an isotropic field.
4. LDF-ISO/ISO: A field which is partially LDF and partially isotropic is interpreted as an isotropic field.

Even though the rms's of the LDF/ISO case shown in Table 4-11 are higher than those obtained for the other three cases, all the rms errors in this case are acceptable. Region 6 which exhibits the highest values in rows 3, 7, and 11, has rms errors of 8.0, 7.5, and 7.4 W/m^2 which are below the acceptable limit (15 W/m^2). These results indicate that no major errors are introduced when LWR fields

Table 4-10. Rms's of the δWe" errors obtained when the stabilized inverse matrix of a spherical radiometer which was derived for an isotropic radiation field was then applied to a field which was partially anisotropic and partially isotropic. (Uncertainties in power measurements are included)

Power uncertainties	Spread	Rms's of δWe" errors (W/m^2)					
		Region 1	Region 2	Region 3	Region 4	Region 5	Region 6
Gaussian random	σ=0.5 W	15.4	56.3	1.2	1.3	19.5	4.1
Systematic	-.9 to .9 W	4.1	20.5	0.6	0.5	7.7	1.2
Combination of Gaussian random and systematic	σ=0.5 W 0.9 W	15.1	56.6	1.1	1.6	19.6	4.1

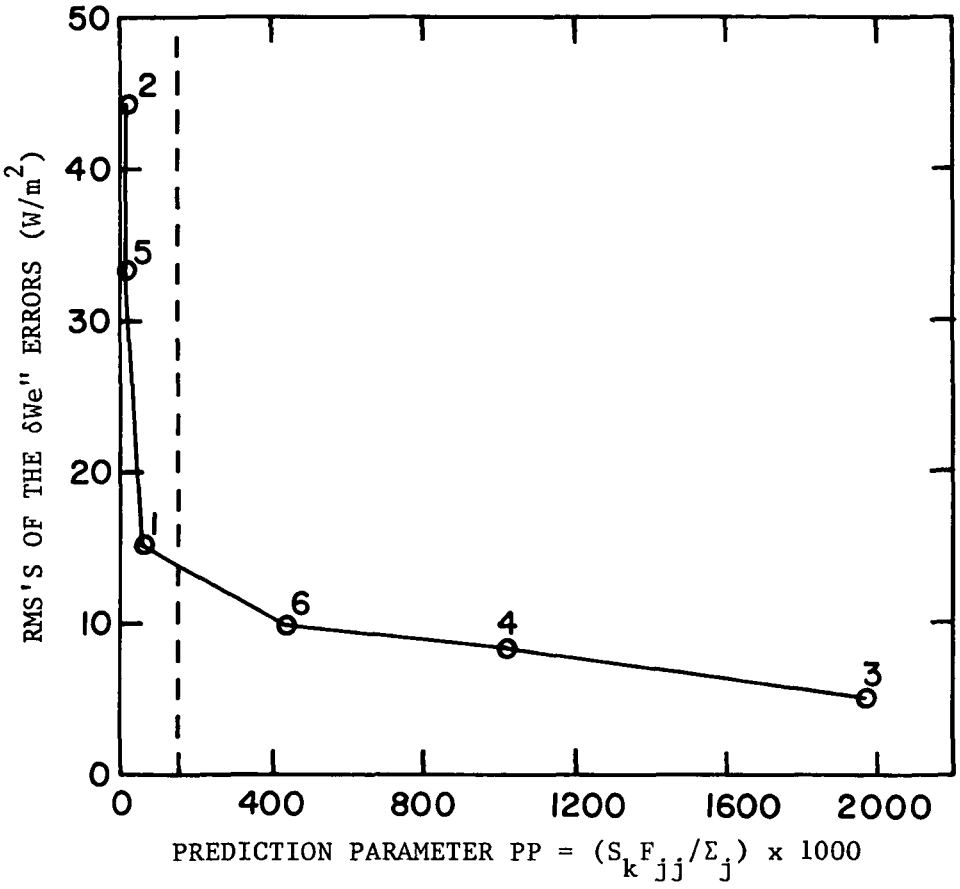

Figure 4-16. Curve Showing the Relationship between the Prediction Parameter and the Rms's of the δWe" Errors Obtained with the Stabilized Inverse Matrix of a Spherical Radiometer Which Was Derived for an Isotropic Radiation Field and Then Applied to a Field Which Was Partially Anisotropic and Partially Isotropic.

Table 4-11. Comparisons of the effects of proper and improper selection of the angular distribution function on the rms's of the δWe" errors obtained with the stabilized inverse matrix of a spherical radiometer for the three regions whose results are predicted acceptable.

Power uncertainties	Spread	Case studied	Rms's of δWe"		
			R3	R4	R6
Gaussian random	σ=0.5 W	LDF/LDF	1.3	1.3	4.3
Gaussian random	σ=0.5 W	ISO/ISO	1.5	1.3	4.3
Gaussian random	σ=0.5 W	LDF/ISO	5.2	2.2	8.0
Gaussian random	σ=0.5 W	LDF-ISO/ISO	1.2	1.3	4.1
Systematic	-.9 to .9 W	LDF/LDF	0.7	0.7	0.7
Systematic	-.9 to .9 W	ISO/ISO	0.9	0.7	0.9
Systematic	-.9 to .9 W	LDF/ISO	4.8	1.8	7.5
Systematic	-.9 to .9 W	LDF-ISO/ISO	0.6	0.5	1.2
Gaussian		LDF/LDF	1.1	1.7	4.4
random	σ=0.5 W	ISO/ISO	1.1	1.8	4.4
plus		LDF/ISO	4.5	1.7	7.4
systematic	0.9 W	LDF-ISO/ISO	1.1	1.6	4.1

are assumed ISOTROPIC during data interpretation.

As discussed in detail before, the instantaneous technique is assumed to apply to regions of the E-A system which have fairly homogeneous emitting and reflecting characteristics. Furthermore, the number of observations should match the number of regions observed in order to obtain a unique solution. Therefore, if a region is split into two subregions having different We values, an additional observation must be taken to meet the requirement of a unique solution. Nevertheless, the following results show that the instantaneous technique can deal successfully with several of these cases without including the required additional radiometer observation.

The errors resulting from region inhomogeneity become more significant if the region is divided into two subregions of approximately equal area, and hence this was the type of region division selected to investigate the effects of inhomogeneities. As explained previously, ΔWe is the difference between the We values of the two subregions formed. Several values of ΔWe were assumed and the results obtained for a spherical radiometer are compared with the corresponding values of the evaluation parameter EP. The value of EP is calculated according to Eq.(4-29) which is rewritten here as applied to the three regions considered acceptable according to the prediction technique.

$$EP = \left[\frac{1}{3} \sum_{\ell=1}^{3} \varepsilon_{\ell}^{2}\right]^{\frac{1}{2}} \qquad (4\text{-}29)$$

where ε is given by Eq.(4-28) which is also rewritten here for easy reference

$$\varepsilon_k = \overline{We_k} - We_k'' \qquad (4\text{-}28)$$

where the subscript k denotes the kth region. $\overline{We}_k$ and We_k'' were previously defined.

Region 3 was selected to be divided into two subregions of approximately equal area in these inhomogeneity studies because it has the largest S_k value. As explained before, S_k is the sum of the shape factors contributed by the kth region to the total set of observations. The S_k value of regions 3, 4 and 6 (that were predicted acceptable) are 2.976, 2.076 and 0.825, respectively, (refer to the matrix for the sphere in Fig. 4-4). For comparison, region 6 was also split into two approximately equal areas and an example of the effects caused by the inhomogeneity of this region is also included. This is the region that has the lowest S_k value among the three regions considered acceptable.

The results obtained are presented in Table 4-12. As seen from lines 2, 4, 6 and 10 of this table, region 6 has the largest rms error in each of these lines. In line 8, regions 4 and 6 have about the same rms value. Hence, the rms error of region 6 is generally the largest in each of the lines and for this reason it was selected for comparison with the corresponding EP value in each case studied. The $\delta We''$ errors from which the rms errors shown in the table were computed are obtained by subtracting the corresponding We" values from the hypothetical standard We's assigned to the regions. In the case of a split region, the standard value is assumed to be the arithmetic mean of the We values assigned to the two subregions.

It can be seen from Table 4-12 that when region 3 was split into two subregions with a difference of $\Delta We = 50\ W/m^2$, the rms error of region 6 became 18.74 W/m^2 which is unacceptable. The EP value in this case is

Table 4-12. Comparisons of evaluation parameters (EP) for different inhomogeneity (ΔWe) values.

ΔWe (W/m^2)	Inhomogeneous region	Parameter	ε_k or rms of δWe"			EP (W/m^2)
			Region 3	Region 4	Region 6	
0	None	ε_k	-6.72	4.53	18.04	11.42
0	None	rms of δWe"	1.06	1.73	4.44	
6	3	ε_k	-7.95	6.53	20.74	13.37
6	3	rms of δWe"	1.38	2.32	4.82	
10	3	ε_k	-8.02	6.90	21.44	13.80
10	3	rms of δWe"	1.18	3.31	5.27	
50	3	ε_k	-14.51	16.00	34.74	23.62
50	3	rms of δWe"	2.99	19.69	18.74	
50	6	ε_k	-6.35	4.81	13.61	9.10
50	6	rms of δWe"	1.06	2.27	15.72	

23.62 W/m^2. All other cases in the table where region 3 is the inhomogeneous region are acceptable.

The last two lines in Table 4-12 refer to the splitting of region 6 into two subregions having a ΔWe value of 50 W/m^2. The rms error of region 6 in this case was only 15.72 W/m^2, barely above the maximum permissible rms value of 15 W/m^2; the corresponding EP value is 9.10 W/m^2. From these results, an estimate of the range of values of EP which indicates when region inhomogeneity can be disregarded was obtained. This range is

$$10 \leq EP \leq 20 \ W/m^2$$

It should be noted that by analyzing additional cases which included varying values of observational errors (combinations of Gaussian and systematic) but excluded regional inhomogeneities, a range of values of EP between 11 and 19 W/m^2 was obtained which is within the range of 10 and 20 W/m^2 discussed above. Hence, it can be concluded that as long as the evaluation parameter has a value between 10 and 20 W/m^2, the effects due to region inhomogeneity can be treated as if caused by instrumental uncertainties, and all regions passing the test of the prediction technique will have acceptable results.

As indicated previously, in extreme cases where the evaluation parameter might be outside the permissible range of values (10 to 20 W/m^2), the value of EP indicates that the radiometer data must be <u>supplemented</u> by other forms of information, (such as cloud photographs),in order to include the additional region.

Best fit technique

The best fit technique is an outgrowth of the instantaneous method just discussed. In that method, the number of measurements matches the number of regions studied and a unique solution is obtained. In the present technique, the number of measurements is much greater than the number of regions observed and the method of least squares is used to find an approximate solution. The results obtained with this method are time averages of the We values of each of the regions observed for the time interval (e.g., month, season) during which the observations are made. The fundamentals of this technique and the results obtained by applying it to a simulated series of satellite observations are presented below.

A. Technique fundamentals

The best fit technique is developed following the same reasoning used in deriving Eq.(4-1) through Eq.(4-17). For easy reference, Eqs.(4-16) and (4-17) are rewritten and renumbered here

$$P_j = \sum_{k=1}^{K} P_{jk} = \sum_{k=1}^{K} F_{jk} \, We_k \tag{4-37}$$

$$F_{jk} = \sum_{i=1}^{I} \frac{\Delta A}{2\pi I(f_k)} \left(\frac{f(\theta) \cos\theta \cos\alpha}{r^2}\right)_{ijk} \tag{4-38}$$

where P_j is the jth power measurement, P_{jk} is the power which the kth region contributes to P_j and F_{jk} is the configuration factor contributed by the kth region to the jth observation. I is the number of elemental areas ΔA of the kth region which appear within the FOV of the jth observation. K is the total number of regions under study. If a region does not appear within the FOV, its corresponding configuration factor is

zero and will not contribute anything to the sum in Eq.(4-37).

The equations are written for a horizontal flat plate radiometer. However, they apply equally well to a spherical radiometer by equating to one the factor cos α in all equations where it appears.

In this technique, the number of measurements J is much greater than the number of regions K. Hence, the problem can be considered overdetermined and some smoothing of errors is to be expected. The smoothing obtained is dependent upon the J/K ratio (Panofsky and Brier, 1968). Instead of the J=K equations shown in Eq.(4-18a) for the instantaneous scheme, one has in this technique J>>K equations representing J power measurements, as follows.

$$\begin{aligned} P_1 &= F_{11}\, We_1 + F_{12}\, We_2 + \ldots + F_{1K}\, We_K \\ P_2 &= F_{21}\, We_1 + F_{22}\, We_2 + \ldots + F_{2K}\, We_K \\ &\vdots \\ P_J &= F_{J1}\, We_1 + F_{J2}\, We_2 + \ldots + F_{JK}\, We_K \end{aligned} \tag{4-39}$$

Eqs.(4-39) represent J surfaces in the coordinate system given by $F_1, F_2, \ldots, F_K$. For example, for the jth plane, the values of these coordinates are $F_{j1}, F_{j2}, \ldots, F_{jK}$.

It is desirable to choose satellite positions which yield more or less equal values of S_k for all regions. As defined before, S_k is the sum of the shape factors in the kth column (i.e., the kth region). For example, for the first column one has

$$S_1 = F_{11} + F_{21} + \ldots + F_{J1} \tag{4-40}$$

and in general,

$$S_k = F_{1k} + F_{2k} + \ldots + F_{Jk} \tag{4-41}$$

This choice of satellite positions insures that the matrix derived from the final K normal equations yields acceptable δWe errors for all regions observed.

The required K normal equations are generated by the method of least squares. The approximate solution obtained is represented by a regression surface P_R whose equation can be written in this application as follows (Spiegel, 1961)

$$P_R = P_o + We_1 F_{R1} + We_2 F_{R2} + \ldots + We_K F_{RK} \tag{4-42}$$

where the coordinate values of this regression surface are F_{R1}, F_{R2},..., F_{RK}. This equation contains K+1 unknowns, the K coefficients We_k, and the P-intercept P_o. Hence, one needs K+1 normal equations to obtain these unknowns.

Since all of the Eqs.(4-39) pass through the origin of the F_1, F_2,.., F_K coordinate system, it will be assumed that the regression surface also passes through the origin of the coordinate system. Then, Eq.(4-42) can be written as

$$P_R = We_1 F_{R1} + We_2 F_{R2} + \ldots + We_K F_{RK} \tag{4-43}$$

Hence, in this case only K normal equations are required to solve the problem. The determinant of the coefficients of the normal equations is found to be nonzero and an approximate solution of the problem is obtained.

Although it is recognized that by making the above assumption (that the regression surface passes through the origin of the coordinate system) one has possibly introduced errors in the partial regression coefficients We, these errors are small and the results are acceptable as will be shown.

Derivation of the K normal equations according to the method of least squares is as follows:

1. Multiply each equation by the first shape factor F_{j1} appearing in the equation and add up the resulting equations. That is, multiply the first equation by F_{11}, the second equation by F_{21}, and so on until the Jth equation is multiplied by F_{J1}. The addition of these equations yields the first of K normal equations, namely

$$\sum_{j=1}^{J} P_j F_{j1} = We_1 \sum_{j=1}^{J} F_{j1}^2 + We_2 \sum_{j=1}^{J} F_{j2} F_{j1} + \ldots$$

$$+ We_K \sum_{j=1}^{J} F_{jK} F_{j1} \qquad (4\text{-}44)$$

2. Multiply each equation by its second shape factor and add the resulting equations to obtain the second normal equation

$$\sum_{j=1}^{J} P_j F_{j2} = We_1 \sum_{j=1}^{J} F_{j1} F_{j2} + We_2 \sum_{j=1}^{J} F_{j2}^2 + \ldots$$

$$+ We_K \sum_{j=1}^{J} F_{jK} F_{j2} \qquad (4\text{-}45)$$

3. Do the same with the remaining shape factors. When each of the equations is multiplied through by its own K shape factor, and the resulting J equations are added up, the Kth normal equation

is obtained, namely

$$\sum_{j=1}^{J} P_j F_{jK} = We_1 \sum_{j=1}^{J} F_{j1} F_{jK} + We_2 \sum_{j=1}^{J} F_{j2} F_{jK} + \ldots + We_K \sum_{j=1}^{J} F_{jK}^2 \tag{4-46}$$

The resulting K equations can be greatly simplified by using the symbols defined below.

$$\overline{PF_\ell} \equiv \sum_{j=1}^{J} P_j F_{j\ell} \tag{4-47}$$

$$\overline{F_\ell F_n} \equiv \sum_{j=1}^{J} F_{j\ell} F_{jn} \tag{4-48}$$

Making these substitutions into the K equations illustrated by Eq.(4-44) through (4-46), one obtains the K equations which are given below in matrix form.

$$\begin{bmatrix} \overline{F_1F_1} & \overline{F_1F_2} & \cdots & \overline{F_1F_K} \\ \overline{F_2F_1} & \overline{F_2F_2} & \cdots & \overline{F_2F_K} \\ \vdots & & & \vdots \\ \overline{F_KF_1} & \overline{F_KF_2} & & \overline{F_KF_K} \end{bmatrix} \begin{bmatrix} We_1 \\ We_2 \\ \vdots \\ We_K \end{bmatrix} = \begin{bmatrix} \overline{PF_1} \\ \overline{PF_2} \\ \vdots \\ \overline{PF_K} \end{bmatrix} \tag{4-49}$$

Or, in symbolic form, these matrices can be written as

$$\overline{FF}\ \{We\} = \{\overline{PF}\} \tag{4-50}$$

where $\overline{FF}$ is the KxK matrix made up of the sums of the products of the

shape factors as defined by Eq.(4-48). {We} is the column matrix whose elements are the regional We values. $\{\overline{PF}\}$ is the column matrix whose elements are the sums of the products of the powers and shape factors as defined by Eq.(4-47).

From Eq.(4-50), it is seen that by inverting the matrix $\overline{FF}$ to obtain $(\overline{FF})^{-1}$ one can find the We values from the relation

$$\{We\} = (\overline{FF})^{-1} \{\overline{PF}\} \tag{4-51}$$

The results obtained by using this technique are now illustrated.

B. Results

The regions observed are those previously presented in schematic form in Figure 4-2, and used for describing the instantaneous technique. In that case, it was assumed that the We values of the six regions remained constant during the short time interval during which the six power measurements were made. Now, however, thirty-six observations are made of the six regions by each radiometer. The We values of the six regions are assumed to remain constant only during six measurements, and then they change before the next set of measurements is taken. The thirty-six values of We are presented in Table 4-13. The average values of the regions (or columns) appear in the last row.

Four types of power measurements (itemized below) were used in order to analyze the range of values that the δWe errors have. In this technique, the δWe errors are the differences between the results obtained and the averages of the regional We values which are shown in the last row of Table 4-13. For each of the four types of power measurements, thirty-six observations were simulated for each radiometer, sphere and

Table 4-13. Values of We of the six regions for each of the six sets of observations.

Meas. No.	Values of We (W/m^2)					
K	Region 1	Region 2	Region 3	Region 4	Region 5	Region 6
1-6	280.0	250.0	240.0	220.0	200.0	160.0
7-12	290.0	240.0	230.0	235.0	210.0	150.0
13-18	300.0	230.0	220.0	240.0	225.0	140.0
19-24	310.0	220.0	210.0	250.0	230.0	130.0
25-30	295.0	230.0	250.0	235.0	215.0	145.0
31-36	285.0	245.0	260.0	225.0	205.0	155.0
AVERAGES	293.3	235.8	235.0	234.2	214.2	146.7

plate. The four types of measurements considered are:

1. Power measurements are exact, i.e., no instrumental errors are included.
2. Powers include Gaussian random errors with σ = 0.5 W.
3. All power measurements include a 0.9 W systematic uncertainty.
4. Powers include combinations of the above mentioned Gaussian and systematic uncertainties.

Table 4-14 displays the results obtained from these simulated power measurements by use of the best fit technique. All of the results shown in this table for cases with and without instrumental errors are found acceptable.

As discussed previously in the case of the instantaneous technique, the effects produced by improper selection of LDF or by inhomogeneities within a region are similar to those produced by instrumental errors and can be treated as such. As mentioned before, these errors are smoothed out by having large values of the ratio J/K. The δWe errors displayed in Table 4-14 show this to be the case, that is, all the results obtained are acceptable.

Table 4-14. δWe errors obtained with the best fit technique for spherical and horizontal plate radiometers. (LDF included)

Power uncertainties	Spread	Radiometer	δWe errors (W/m^2)					
			Region 1	Region 2	Region 3	Region 4	Region 5	Region 6
None	--	Sphere	10.9	-9.8	-9.0	7.8	4.4	-2.3
None	--	Plate	10.0	-7.5	-8.3	5.9	3.1	-1.2
Gaussian random	σ=0.5 W	Sphere	12.1	-11.3	-9.3	8.3	4.3	-2.4
Gaussian random	σ=0.5 W	Plate	11.4	-9.3	-8.5	6.5	3.0	-1.3
Systematic	0.9 W	Sphere	11.7	-8.9	-8.2	8.7	5.2	-1.5
Systematic	0.9 W	Plate	11.1	-6.4	-7.2	7.0	4.2	-0.1
Gaussian random plus systematic	σ=0.5 W 0.9 W	Sphere	13.0	-10.4	-8.5	9.2	5.1	-1.5
		Plate	12.5	-8.1	-7.4	7.6	4.1	-0.2

CHAPTER V. TECHNIQUES FOR OBTAINING THE RADIANT REFLECTANCE

The instantaneous and best fit techniques as used for determining the radiant reflectance Wr from power measurements by spherical and horizontal plate radiometers are discussed in this chapter. These techniques were introduced in the previous chapter for the case of the terrestrial emitted LWR flux We since that application is less complex than the present one. Since the best fit technique is an outgrowth of the instantaneous technique, the latter will be treated first just as was done in the case of We.

Instantaneous technique

The instantaneous technique yields the values of Wr that the regions under study have at the time the set of measurements is performed. The Wr values are obtained from a set of J simultaneous equations expressing the powers measured by a detector observing the K=J regions under study. Therefore, if the solution exists, it is unique.

A. Technique development

The following application for the case of Wr is very similar to the development introduced for We, except that in that case a LDF is used while the present application includes a bidirectional reflectance model. A horizontal plate satellite radiometer will be considered in this development; however, the equations discussed also apply to a spherical radiometer by equating the factor $\cos \alpha = 1$ wherever this factor appears.

Figure 5-1 presents for easy reference the same regions observed in the case of the emitted LWR, as well as the same satellite position

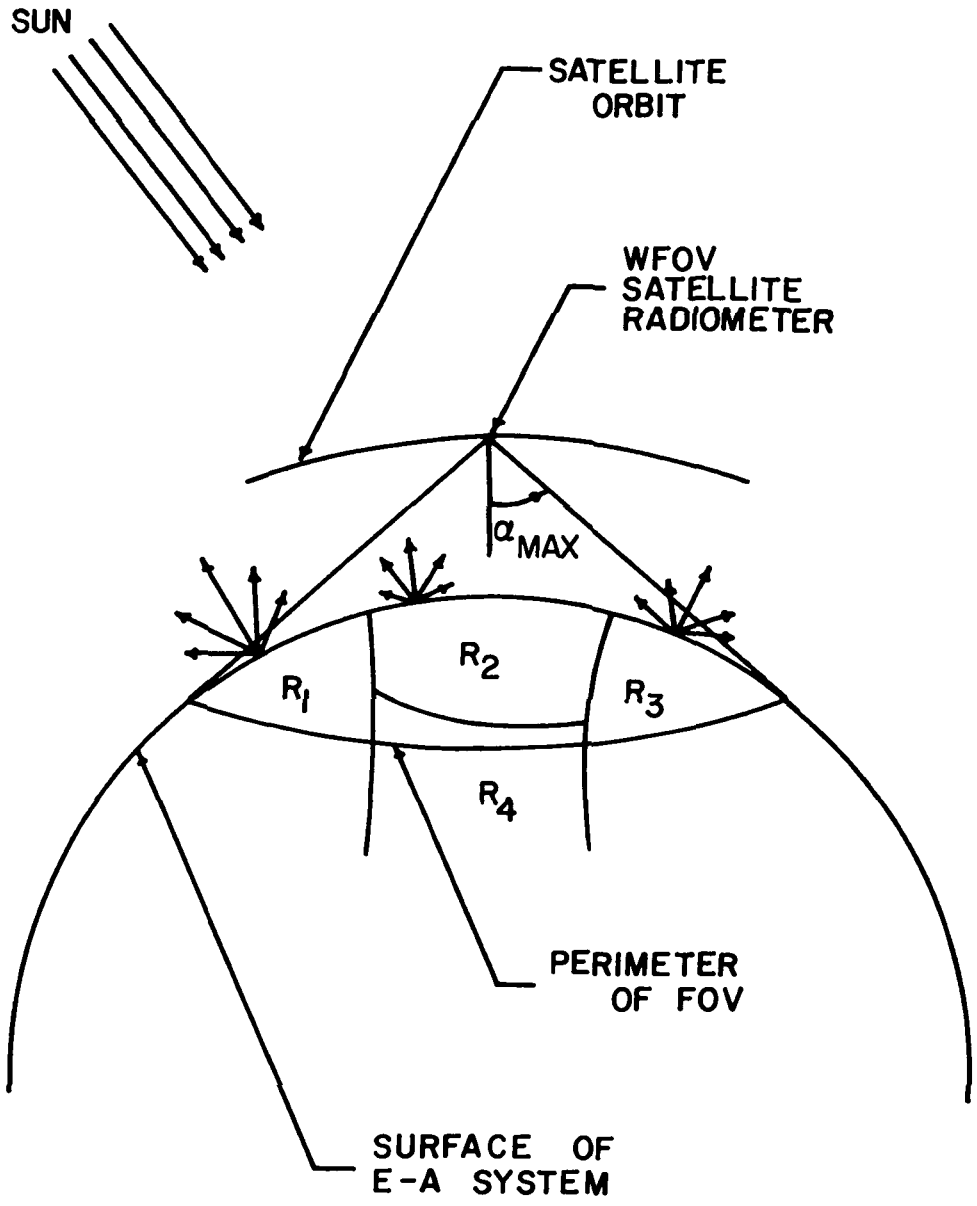

Figure 5-1. Observation of the Solar Radiation Reflected by the Several Regions within the FOV of a Low Spatial Resolution Radiometer.

from which one of the observations is assumed to be made. Furthermore, the regions are defined identically as for the case of LWR by using the same ΔA's. The only difference between the case of We and Wr is that in the latter case it is the reflecting characteristics that are assumed different from region to region. The ΔA's used to define the regions and to perform the numerical integrations are all of equal area as described previously. The division of the E-A system's surface into these elemental areas is discussed in detail in Appendix A.

An expression similar to Eq.(4-8) for the SWR power ΔP_{ijk} that ΔA_{ijk} contributes to a radiometer measurement is developed as follows. If ΔA_{ijk} denotes the ith elemental area within the k th region that appears in the FOV of the jth observation, then ΔP_{ijk} represents the power increment that this elemental area contributes to the jth observation. The expression for ΔP_{ijk} is written as

$$\Delta P_{ijk} = Nr\ (\theta,\psi,\zeta)_{ijk}\ \Delta A_{ijk} \cos\ \theta_{ijk} \frac{A_s \cos\alpha_{ijk}}{r^2_{ijk}} \qquad (5\text{-}1)$$

where $Nr(\theta,\psi,\zeta)$ is the reflected radiance. As indicated by its arguments, this quantity depends on the solar zenith angle ζ, and on the zenith and aximuthal angles of the radiometer θ, and ψ, respectively. (Refer to Figure 5-2 which defines pictorially the angles used in the expression). α is the nadir angle of ΔA as observed from the satellite, and r is the distance between ΔA and the satellite. As in the case of We, the characteristic area of the satellite radiometer A_s is assumed to be unity and no subscripts will be affixed to ΔA since all elemental areas are equal. Then, Eq.(5-1) reduces to

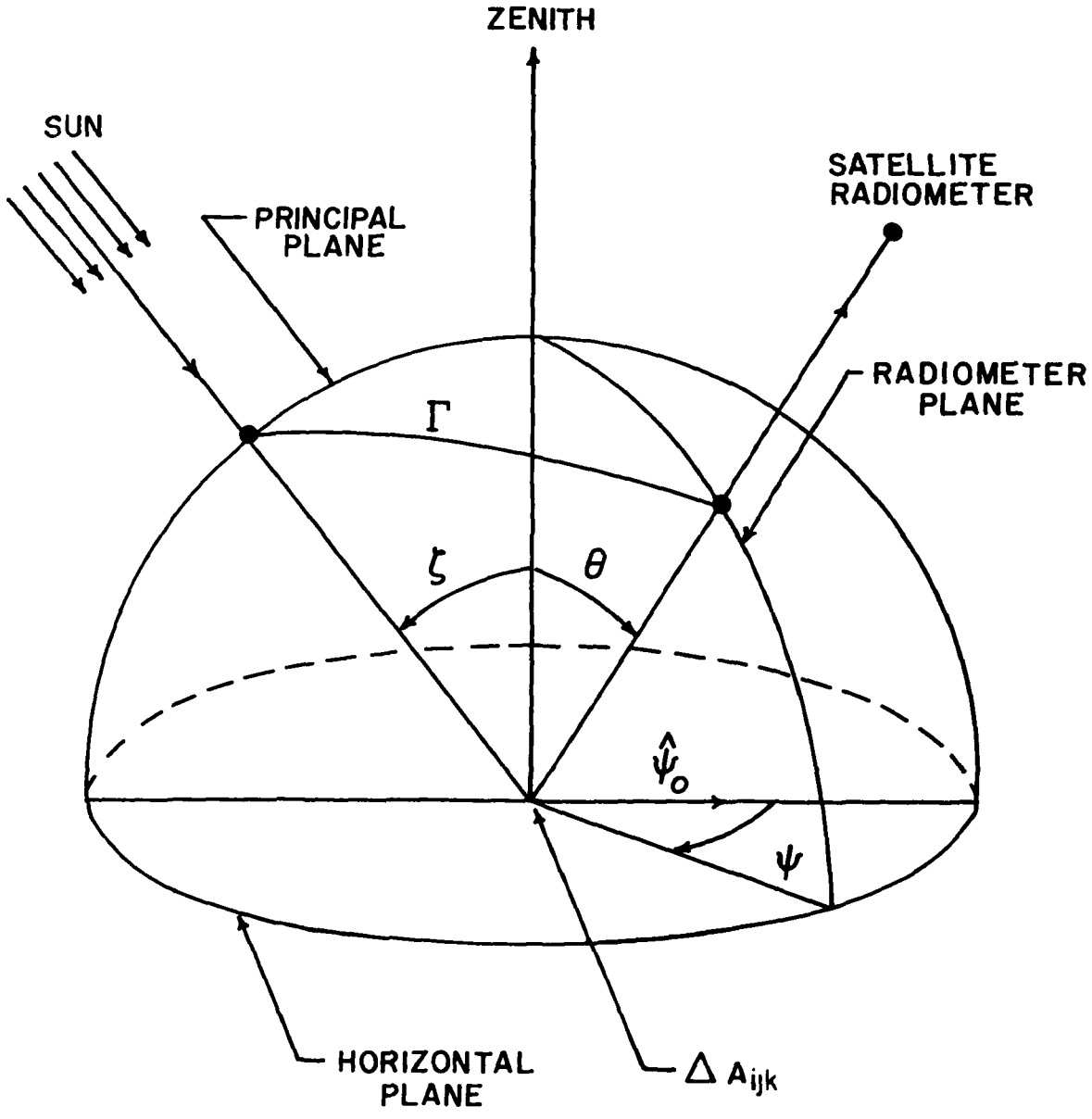

Figure 5-2. Pictorial Definition of the Angles Used to Compute the SWR Power Increment ΔP_{ijk} Contributed by the Elemental Area ΔA_{ijk}.

$$\Delta P_{ijk} = Nr_{ijk}\ \Delta A\ \left(\frac{\cos\theta\cos\alpha}{r^2}\right)_{ijk} \tag{5-2}$$

where Nr_{ijk} denotes the reflected radiance at ΔA_{ijk}.

One of the fundamental concepts included in the instantaneous and best fit techniques when applied to the SWR flux is that a bidirectional reflectance model (BRM) can be used to describe the reflected radiation field (Raschke, et al., 1973). In order to express Eq.(5-2) in terms of the bidirectional reflectance $\rho(\theta,\psi,\zeta)$ this quantity is now defined as

$$\rho(\theta,\psi,\zeta) = \frac{Nr(\theta,\psi,\zeta)}{Hs(\zeta)} \tag{5-3}$$

where $Hs(\zeta)$ is the solar irradiance at ΔA_{ijk} which can be expressed in terms of H_o, the solar irradiance at ΔA_{ijk} for zero solar zenith angle as follows

$$Hs(\zeta) = H_o \cos\zeta \tag{5-4}$$

Hence, using Eqs.(5-3) and (5-4) in (5-2) one obtains

$$\Delta P_{ijk} = \Delta A\ H_o\ [\cos\zeta\ \rho(\theta,\psi,\zeta)]_{ijk}\left(\frac{\cos\theta\cos\alpha}{r^2}\right)_{ijk} \tag{5-5}$$

The following three quantities are needed in order to develop an expression for ΔP_{ijk} that facilitates its computation. The directional reflectance $r(\zeta)$ is defined by

$$r(\zeta) = \frac{Wr(\zeta)}{Hs(\zeta)} \tag{5-6}$$

The ratio of this quantity for an arbitrary solar zenith angle to its value for zero solar zenith angle will be denoted by $R_1(\zeta)$, that is

$$R_1(\zeta) = \frac{r(\zeta)}{r(0)} \tag{5-7}$$

This quantity is very useful in this development and its value for several values of ζ has been obtained by several investigators (Raschke, et al., 1973).

Another ratio that will often be used is defined by

$$R_2(\theta,\psi,\zeta) = \frac{r(\zeta)}{\pi\rho(\theta,\psi,\zeta)} \tag{5-8}$$

This quantity is also plotted by Raschke, et al. (1973).

Substitution in Eq.(5-5) of the value $\rho(\theta,\psi,\zeta)$ as obtained from Eq.(5-8) results in

$$\Delta P_{ijk} = \Delta A\, H_o \left[\frac{r(\zeta)\cos\zeta}{\pi R_2(\theta,\psi,\zeta)} \right]_{ijk} \left(\frac{\cos\theta\cos\alpha}{r^2} \right)_{ijk} \tag{5-9}$$

Using the value of $r(\zeta)$ given by Eq.(5-7) in this expression one has

$$\Delta P_{ijk} = \left(\frac{\Delta A}{\pi} \right) \left[\frac{\cos\theta\cos\alpha}{R_2(\theta,\psi,\zeta) r^2} \right]_{ijk} \left[R_1(\zeta)\cos\zeta \right]_{ijk} H_o \left[r(0) \right]_{ijk} \tag{5-10}$$

From Eq.(5-6) one writes

$$Wr(\zeta) = Hs(\zeta)\, r(\zeta) \tag{5-11}$$

from which one obtains for $\zeta=0$

$$Wr(0) = Hs(0)\, r(0) \tag{5-12}$$

But from Eq.(5-4), $Hs(0) = H_o$. Hence,

$$Wr(0) = H_o\, r(0) \tag{5-13}$$

Substituting this value of $H_o\, r(0)$ into Eq.(5-10) one obtains

$$\Delta P_{ijk} = \left(\frac{\Delta A}{\pi} \right) \left[\frac{\cos\theta\cos\alpha}{R_2(\theta,\psi,\zeta) r^2} \right]_{ijk} \left[R_1(\zeta)\cos\zeta \right]_{ijk} \left[Wr(0) \right]_{ijk} \tag{5-14}$$

One recalls that the shape factor F for a LWR field and a radiometer of unit characteristic area was defined by

$$P = F\ We \tag{5-15a}$$

or

$$\Delta P_{ijk} = F_{ijk}\ We_{ijk} \tag{5-15b}$$

One can make a similar definition here, that is,

$$\Delta P_{ijk} = F_{ijk}\ Wr(0)_{ijk} \tag{5-16}$$

Then, comparing Eqs.(5-14) and (5-16) one can write for the shape factor in this application

$$F_{ijk} = \left(\frac{\Delta A}{\pi}\right) \left[\frac{\cos\theta \cos\alpha}{R_2(\theta,\psi,\zeta) r^2}\right]_{ijk} [R_1(\zeta) \cos\zeta]_{ijk} \tag{5-17}$$

Before discussing the significance of Eq.(5-17), it is convenient to derive a similar expression for a slightly different shape factor as follows. Using Eq.(5-4) to substitute the value of $H_o \cos\zeta$ in Eq.(5-9) one has

$$\Delta P_{ijk} = \left(\frac{\Delta A}{\pi}\right) \left[\frac{\cos\theta \cos\alpha}{R_2(\theta,\psi,\zeta) r^2}\right]_{ijk} [Hs(\zeta)\ r(\zeta)]_{ijk} \tag{5-18}$$

But the last factor in this expression is $Wr(\zeta)$ as given by Eq.(5-11). Hence, the result is

$$\Delta P_{ijk} = \left(\frac{\Delta A}{\pi}\right) \left[\frac{\cos\theta \cos\alpha}{R_2(\theta,\psi,\zeta) r^2}\right]_{ijk} [Wr(\zeta)]_{ijk} \tag{5-19}$$

Comparing Eqs.(5-14) and (5-19), one sees that

$$[Wr(\zeta)]_{ijk} = [R_1(\zeta) \cos\zeta]_{ijk} [Wr(0)]_{ijk} \tag{5-20}$$

Furthermore, while Eq.(5-14) contains explicitly the value of Wr only for $\zeta=0$, Eq.(5-19) contains $Wr(\zeta)$ which applies to any position of the sun. For this reason, a "true" shape factor Ft is defined from Eq.(5-20) based on the definition given by Eq.(5-15b) as follows.

$$Ft_{ijk} = \left(\frac{\Delta A}{\pi}\right)\left[\frac{\cos\theta \cos\alpha}{R_2(\theta,\psi,\zeta)r^2}\right]_{ijk} \tag{5-21}$$

Hence, Eq.(5-19) can be written as

$$\Delta P_{ijk} = Ft_{ijk}\,[Wr(\zeta)]_{ijk} \tag{5-22}$$

From Eqs.(5-17) and (5-21) one has

$$F_{ijk} = Ft_{ijk}\,[R_1(\xi)\cos\zeta]_{ijk} \tag{5-23}$$

or

$$[R_1(\zeta)\cos\zeta]_{ijk} = \frac{F_{ijk}}{Ft_{ijk}} \tag{5-24}$$

Substituting this expression into Eq.(5-20) one obtains,

$$[Wr(\zeta)]_{ijk} = \left[\frac{F}{Ft}\right]_{ijk}[Wr(0)]_{ijk} \tag{5-25}$$

One now has available the equation required to give a mathematical definition of a region for the case of reflected SWR. It is necessary to use a quantity that can have a constant value throughout a given region in order to represent the homogeneous reflecting characteristics of the region. Obviously, $Wr(\zeta)$ can not be used since it depends on ζ which varies within any region for a given sun position due to the earth's curvature. However, Wr(0) can be used as follows. Every ΔA within an area having approximately homogeneous reflecting characteristics would reflect the same amount of energy Wr(0) if the sun were positioned at the zenith of each ΔA.

An expression similar to Eq.(4-15) for the case of LWR can now be found for SWR. That is, an expression can be developed for the SWR power P_{jk} (which is the power that the kth region contributes to the jth observation) in terms of the configuration factor F_{jk} of the kth region and jth observation. By summing up the powers ΔP_{ijk} contributed by the ΔA's (I in number) within the kth region, and using Eq.(5-16) to express ΔP_{ijk} in terms of F_{ijk}, one obtains

$$P_{jk} = \sum_{i=1}^{I} \Delta P_{ijk} = \sum_{i=1}^{I} F_{ijk} \{Wr(0)\}_{ijk} \tag{5-26}$$

Since Wr(0) is a constant throughout the kth region, it can be taken outside the summation sign, that is

$$P_{jk} = \{Wr(0)\}_k \sum_{i=1}^{I} F_{ijk} = F_{jk} \{Wr(0)\}_k \tag{5-27}$$

where $F_{jk} = \sum_{i=1}^{I} F_{ijk}$ is, as mentioned previously, the configuration factor contributed by the kth region to the jth observation.

An expression similar to Eq.(4-16) for the total power of the jth observation is obtained by summing up the powers contributed by each region within the FOV of the radiometer. Hence,

$$P_j = \sum_{k=1}^{K} F_{jk} \{Wr(0)\}_k \tag{5-28}$$

where K is the number of regions in the set that is under study. There are J equations of the type of Eq.(5-28) for the J observations made, and this number must match K, the total number of regions observed. In order to simplify the notation, the symbol Wro will be used to denote Wr(0). Then, the J = K equations are

$$
\begin{aligned}
P_1 &= F_{11}\,Wro_1 + F_{12}\,Wro_2 + \ldots + F_{1K}\,Wro_K \\
P_2 &= F_{21}\,Wro_1 + F_{22}\,Wro_2 + \ldots + F_{2K}\,Wro_K \\
&\cdot \\
&\cdot \\
&\cdot \\
P_J &= F_{J1}\,Wro_1 + F_{J2}\,Wro_2 + \ldots + F_{JK}\,Wro_K
\end{aligned}
\qquad (5\text{-}29a)
$$

These equations are represented in matrix form as follows.

$$
\begin{vmatrix}
F_{11} & F_{12} & \cdot & \cdot & \cdot & F_{1K} \\
F_{21} & F_{22} & \cdot & \cdot & \cdot & F_{2K} \\
\cdot & & & & & \\
\cdot & & & & & \\
\cdot & & & & & \\
F_{J1} & F_{J2} & \cdot & \cdot & \cdot & F_{JK}
\end{vmatrix}
\begin{vmatrix}
Wro_1 \\ Wro_2 \\ \cdot \\ \cdot \\ \cdot \\ Wro_K
\end{vmatrix}
=
\begin{vmatrix}
P_1 \\ P_2 \\ \cdot \\ \cdot \\ \cdot \\ P_J
\end{vmatrix}
\qquad (5\text{-}29b)
$$

Symbolically, these matrices are written as

$$F\{Wro\} = \{P\} \qquad (5\text{-}29c)$$

where F is the JxJ (or KxK since J = K) configuration factor matrix. {Wro} and {P} are the column matrices made up of the Wro values of the K regions and the P powers of the J observations, respectively. Eqs.(5-29a) through (5-29c) are equivalent to Eqs.(4-18a) through (4-18c), respectively, for the LWR case.

If the exact values of P are known, then by inverting F one obtains F^{-1} and the values Wro' are obtained from the following expression.

$$\{Wro'\} = F^{-1}\,\{P\} \qquad (5\text{-}30a)$$

As in the case of Eq.(4-19) for the LWR problem, the values of Wro' obtained agree with the actual Wro values to at least six decimal places. This indicates that the matrix inversion subroutines used do not introduce computational errors. In this case then, since Wro' = Wro, one can write

$$F^{-1}\{P\} = \{Wro\} \tag{5-30b}$$

Before proceeding to discuss the effects that observational errors have on the results obtained, one point needs to be clarified. Eq.(5-30b) yields the hypothetical value Wro of a region by means of the matrix operation indicated by this equation. However, how does one go from here to obtaining the desired result? That is, how does one obtain the value of $Wr(\zeta)$ of a region if Wro is known for that region? This question is answered in the following discussion.

It is not possible to develop a set of equations equivalent to Eqs.(5-29) in terms of $Wr(\zeta)$ rather than Wro. The reason for this is that when the power increments ΔP_{ijk} are added up to obtain the power P_{jk} contributed by the kth region to the jth observation, $Wr(\zeta)$ can not be taken out of the summation sign as was done with Wro to obtain Eq.(5-27). This can be seen by adding up Eq.(5-22), that is

$$P_{jk} = \sum_{i=1}^{I} Ft_{ijk} \, [Wr(\zeta)]_{ijk} \tag{5-31}$$

where the value of $Wr(\zeta)$ is different for each ΔA_{ijk}. However, it is possible to write

$$P_{jk} = \overline{[Wr(\zeta)]}_{jk} \sum_{i=1}^{I} Ft_{ijk}$$

or

$$P_{jk} = Ft_{jk} \, \overline{[Wr(\zeta)]}_{jk} \tag{5-32}$$

where $\overline{[Wr(\zeta)]}_{jk}$ is the average value of $Wr(\zeta)$ obtained for the kth region during the jth observation.

Eq.(5-32) is similar to Eq.(5-27) which is rewritten here in terms of Wro rather than Wr(0), that is

$$P_{jk} = F_{jk}\, Wro_k \tag{5-33}$$

It is convenient to derive from Eqs.(5-32) and (5-33) two different expressions for the power P_k that the kth region contributes to the total number of observations J=K. One expression is obtained by adding up Eq.(5-32) over the J measurements.

$$P_k = \sum_{j=i}^{J} P_{jk} = \sum_{j=1}^{J} Ft_{jk}\, \overline{[Wr(\zeta)]}_{jk} \tag{5-34}$$

or

$$P_k = \langle Wr(\zeta)\rangle_k \sum_{j=1}^{J} Ft_{jk} \tag{5-35}$$

or

$$P_k = St_k \langle Wr(\zeta)\rangle_k \tag{5-36}$$

where St_k is the sum of the true configuration factors Ft_{jk} contributed by the kth region to the total set of J observations. $\langle Wr(\zeta)\rangle_k$ is the average value of $Wr(\zeta)$ obtained for the kth region for the set of J observations.

Similarly, by adding up Eq.(5-33), one writes

$$P_k = \sum_{j=1}^{J} F_{jk}\, Wro_k \tag{5-37}$$

As discussed previously, the kth region is assumed to have the value Wro_k during the short time interval in which the J observations are made; that is, the reflecting characteristics of the region remain

unchanged. Hence, it can be taken out of the summation sign to obtain

$$P_k = Wro_k \sum_{j=1}^{J} F_{jk} \tag{5-38}$$

or

$$P_k = S_k \, Wro_k \tag{5-39}$$

where S_k is the sum of the shape factors contributed by the kth region to the complete set of J observations.

Equating Eqs. (5-36) and (5-39) one has

$$St_k \, \langle Wr(\zeta) \rangle_k = S_k \, Wro_k \tag{5-40}$$

or

$$\langle Wr(\zeta) \rangle_k = \frac{S_k}{St_k} Wro_k \tag{5-41}$$

Thus, once the values of Wro have been determined by use of Eq.(5-30b) (or equations similar to this which will be introduced later) one can find the corresponding average values of $Wr(\zeta)$ by using Eq.(5-41).

B. Observational errors

The effects that observational errors have on the results is now investigated. A notation similar to that introduced for the case of LWR is used here. P' is the sum of the instrumental error δP and the exact power P. δWro is the difference between Wro', which is the value obtained, and the actual value Wro. Hence one can write

$$F^{-1}\{P'\} = F^{-1}\{P+\delta P\} = \{Wro'\} = \{ Wro + \delta Wro\} \tag{5-42}$$

Subtracting Eq.(5-30b) from Eq.(5-42) one obtains

$$F^{-1}\{\delta P\} = \{\delta Wro\} \tag{5-43}$$

As in the case of LWR, it was found that the inverse matrix F^{-1} was unstable, that is, the power uncertainties δP were highly magnified by F^{-1}. By applying the stabilization scheme developed and used previously, the original matrix F was rendered well-conditioned. This new matrix is denoted by F_{wc} and its inverse by F_{wc}^{-1} as was done in the case of We. $\delta Wro'$ denotes the new errors added to Wro by operating with F_{wc}^{-1} on the column matrix {P} made up of exact power values. $Wro^{(1)}$ is the sum of Wro and the Wro' errors, that is

$$F_{wc}^{-1}\{P\} = \{Wro^{(1)}\} = \{Wro + \delta Wro'\} \tag{5-44}$$

which is similar to Eq.(4-23) for the case of We.

An expression similar to Eq.(4-24) is also obtained, namely,

$$F_{wc}^{-1}\{P'\} = F_{wc}^{-1}\{P + \delta P\} = \{Wro''\} = \{Wro + \delta Wro''\} \tag{5-45}$$

where $\delta Wro''$ is the error obtained from the perturbed powers $P' = P + \delta P$ with the new inverse matrix F_{wc}^{-1}. Wro" is the sum of the actual value Wro and the error $\delta Wro''$.

As was shown previously, the value of $\langle Wr(\zeta)\rangle_k$ can be obtained by using Eq.(5-41) once Wro is known. This value of Wro is obtained only when there are no uncertainties in the power measurements, that is when $\delta P = 0$, as seen from Eq.(5-30b). Hence, the values of $\langle Wr(\zeta)\rangle_k$ also correspond to the case for which $\delta P = 0$. Now, however, the results Wro" contain the uncertainties $\delta Wro''$ as indicated in Eq.(5-45). There-

fore, Eq.(5-41) is written in the following modified form,

$$\frac{S_k}{St_k} Wro''_k = \langle Wr''(\zeta)\rangle_k \tag{5-46}$$

where

$$\langle Wr''(\zeta)\rangle_k = \langle Wr(\zeta)\rangle_k + \delta Wr''(\zeta)_k \tag{5-47}$$

The value of $\langle Wr(\zeta)\rangle_k$ is given by Eq.(5-41) for the case of $\delta P=0$, as was just explained, and $\delta Wr''(\zeta)_k$ is the error contained in the result $\langle Wr''(\zeta)\rangle_k$. The Wro''_k values are the results obtained by means of Eq.(5-45).

Thus, Eq.(5-46) can be rewritten as

$$\frac{S_k}{St_k} [Wro + \delta Wro'']_k = \langle Wr(\zeta)\rangle_k + \delta Wr''(\zeta)_k \tag{5-48}$$

Subtracting Eq.(5-41) from Eq.(5-48) one obtains

$$\delta Wr''(\zeta)_k = \frac{S_k}{St_k} \delta Wro''_k \tag{5-49}$$

This equation and Eq.(5-41) will be used later in the analysis of the results obtained. It should be pointed out here that the $\delta Wr''(\zeta)$'s are the errors that have real significance since they represent the errors in the $\langle Wr''(\zeta)\rangle$ values according to Eq.(5-47). However, the $\delta Wro''$'s must be known first in order to obtain the $\delta Wr''(\zeta)$'s per Eq.(5-49).

C. Diffuse reflection model

In this section is discussed the procedure followed to study how the results are affected when one assumes a diffuse reflection (DIF) model for interpreting data collected from regions whose SWR field is described in terms of a bidirectional reflectance model (BRM). The essential difference between these two models resides in the value assigned to the parameter $R_2(\theta,\psi,\zeta)$ defined by Eq.(5-8) which is rewritten here for easy reference

$$R_2(\theta,\psi,\zeta) = \frac{r(\zeta)}{\pi\rho(\theta,\psi,\zeta)} \qquad (5\text{-}8)$$

As was pointed out previously, plots of the function R_2 are given by Raschke, et al. (1973) for snow and different cloud types. Some of the plotted values for R_2 go as low as 0.4, while others go as high as 1.4. The curves presented by Raschke, et al. were used as a basis for constructing a hypothetical BRM to describe a SWR field. A series of satellite radiometer observations were simulated and the power measurements were computed using the BRM indicated above.

During data interpretation in one of the investigations, $R_2(\theta,\psi,\zeta)$ was equated to one which is the value that this function has for a diffuse reflection model. The results obtained were affected in a totally unpredictable manner. Some of the results that should have been acceptable became rejectable, while some of the rejectable ones became acceptable. Hence, as opposed to the LWR case where use of an improper LDF during data interpretation does not significantly affect the original results, the use of the DIF model during interpretation of SWR data can produce results which may be totally unreliable.

D. Computational procedure

The procedure followed to obtain the Wro" values according to Eq.(5-45) first requires generating the matrix F; then, by applying to F the stabilization procedure, F_{wc} is obtained, from which the inverse matrix F_{wc}^{-1} is calculated. Hence, the procedure must include computations of each F_{jk} which are the elements of the matrix F. These elements are the sums of the shape factors F_{ijk} of the elemental areas ΔA_{ijk} according to Eq.(5-27). Therefore, the shape factor F_{ijk} of each ΔA_{ijk} within the FOV of the radiometer must be calculated. These calculations are done by computer.

The following discussion introduces the equations used in the computer program in order to calculate each F_{ijk} according to Eq.(5-17) which is rewritten here to facilitate reference to it.

$$F_{ijk} = \left(\frac{\Delta A}{\pi}\right)\left[\frac{\cos\theta \cos\alpha \cos\zeta}{r^2}\right]_{ijk}\left[\frac{R_1(\zeta)}{R_2(\theta,\psi,\zeta)}\right]_{ijk} \qquad (5\text{-}50)$$

One can see that the angles θ, α, and ζ must be determined in order to compute the three cosine functions and the functions R_1 and R_2 shown in the above equation. Also, r, the distance between the radiometer and the observed ΔA, must be calculated.

The values of the following eight quantities must be known for each value of F_{ijk} to be calculated. The same symbols used by Raschke, et al. (1973) are used here in order to facilitate reference to their document.

1. λ_G, δ: the Greenwich hour angle (measured in degrees westward) and the declination of the sun, respectively.

2. λ, ϕ: the longitude and latitude of ΔA_{ijk}, respectively.
3. λ_s, ϕ_s: the longitude and latitude of the sub-satellite point, respectively.
4. R: the radius of the E-A system. The value used is 6401.55 km; 6371.23 km for the radius of the earth, and 30.32 km for the thickness of the atmospheric spherical shell.
5. H: the height of the satellite, assumed here to be 800 km.

The following quantity is often used and hence it is here defined

$$K = \frac{R+H}{R} \tag{5-51}$$

From Figure 3-2, three important relationships among the different angles shown in the figure are easily deduced. An expression for r, the distance between the satellite and ΔA_{ijk} can be obtained from this figure. Eqs.(3-23) through (3-26) give these relationships which are rewritten here for easy reference.

$$\theta = \alpha + \gamma \tag{5-52}$$

$$R \sin \theta = (R+H) \sin \alpha \tag{5-53}$$

or

$$\sin \theta = K \sin \alpha \tag{5-54}$$

$$\sin \gamma = \frac{r}{R} \sin \alpha \tag{5-55}$$

$$r^2 = R^2 + (R+H)^2 - 2R(R+H) \cos \gamma \tag{5-56}$$

From the above equations θ and r are computed. The remaining angles needed to solve Eq.(5-50) are ζ and ψ which are obtained from the following expressions given by Raschke, et al. (1973). A detailed derivation of these expressions is presented in Appendix B.

$$\zeta = \cos^{-1}\{\cos\phi\cos\delta\cos(\lambda_G - \lambda) + \sin\phi\sin\delta\} \tag{5-57}$$

$$\psi = \cos^{-1}\{\frac{\cos\zeta\cos\theta - \cos\Gamma}{\sin\zeta\sin\theta}\} \tag{5-58}$$

where

$$\cos\Gamma = \frac{1}{D}\{(K\cos\phi_s\cos(\lambda_s - \lambda_G) - \cos\phi\cos(\lambda - \lambda_G))\cos\delta + (K\sin\phi_s - \sin\phi)\sin\delta\} \tag{5-59}$$

and

$$D = \{K^2 + 1 - 2K(\cos\phi_s\cos\phi\cos(\lambda - \lambda_s) + \sin\phi_s\sin\phi)\}^{\frac{1}{2}} \tag{5-60}$$

E. Results

The illustration selected to discuss the application of the instantaneous technique to the case of Wro is the same as that introduced earlier for We. In that application, a satellite was assumed to circle the earth in an orbit whose inclination was slightly greater than 90^o. Six observations were simulated of six hypothetical regions which had different We values. Figure 4-2 is a schematic representation of the six regions and the subsatellite points of the six observations. In the present application, these same regions are assumed to have different Wro values which are uniform within each of the regions. Figure 5-3 displays the six regions, the six subsatellite points, the subsolar point, and the Wr(0) = Wro values. This figure also shows the values of $\langle Wr(\zeta)\rangle_s$ and $\langle Wr(\zeta)\rangle_p$ obtained according to Eq.(5-41)

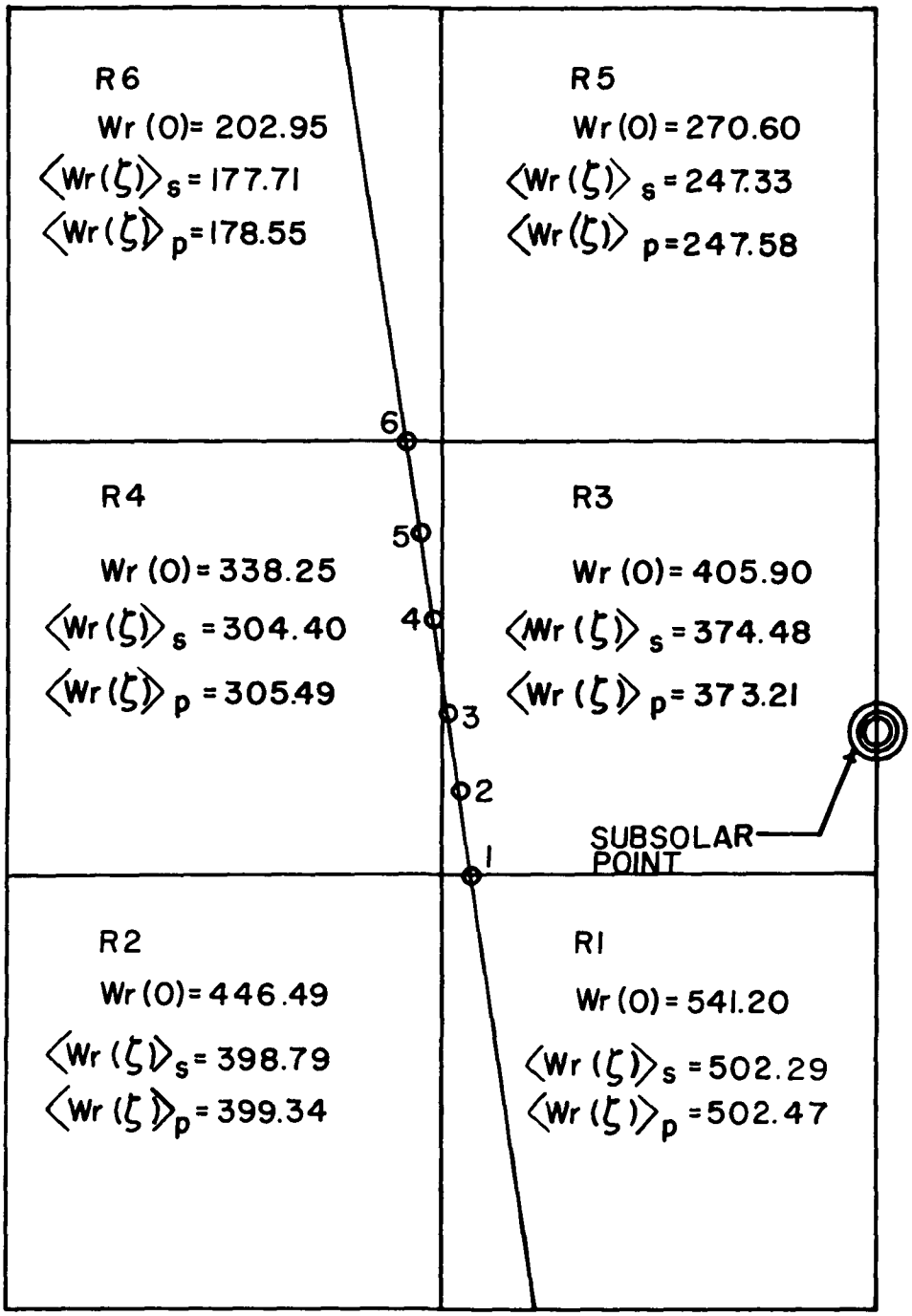

Figure 5-3. Schematic of the Six Regions Observed During a Single Satellite Pass. The Identifying Number and the Value of Wr(0) of Each Region, the Subsolar Point and the Six Subsatellite Points of the Observations Are Shown.

as particularized to the sphere and plate in Eqs.(5-61) and (5-62).

$$\langle Wr(\zeta)\rangle_s = \left(\frac{S_k}{St_k}\right)_s Wr(0) \tag{5-61}$$

$$\langle Wr(\zeta)\rangle_p = \left(\frac{S_k}{St_k}\right)_p Wr(0) \tag{5-62}$$

where s and p are subscripts denoting sphere and plate, respectively. $\left(\frac{S_k}{St_k}\right)_s$ and $\left(\frac{S_k}{St_k}\right)_p$ are the ratios of the sums of the shape factors to the sums of the true shape factors that the kth region contributes to the total set of six measurements. As indicated by Eqs.(5-38) and (5-39), and by Eqs.(5-35) and (5-36), S_k and St_k are given by

$$S_k = \sum_{j=1}^{J=6} F_{jk} \tag{5-63}$$

$$St_k = \sum_{j=1}^{J=6} Ft_{jk}$$

where J = 6 is the total number of observations in the present illustration.

The reason corresponding values of $\langle Wr(\zeta)\rangle_s$ and $\langle Wr(\zeta)\rangle_p$ differ slightly for the six regions in Figure 5-3 is thought to be due to small truncation errors introduced in the computations of the shape factors and their sums S_k and St_k.

Figure 5-4 displays the original, ill-conditioned, 6 x 6 configuration factor matrices for the sphere and plate radiometers generated according to Eqs.(5-29) for the six observations under consideration.

F(J,1)	F(J,2)	F(J,3)	F(J,4)	F(J,5)	F(J,6)
.189686179	.068394333	.543375122	.144790086	.000000000	.000000000
.040528358	.029207258	.628556145	.238738238	.000456674	.000883453
.007450660	.009006905	.579626443	.329356206	.004237711	.010115524
.000691278	.001268763	.437124002	.442853207	.017848877	.049218886
.000000000	.000000000	.247445185	.473557131	.052651685	.189266111
.000000000	.000000000	.092187183	.256772937	.104251122	.501478375

F(J,1)	F(J,2)	F(J,3)	F(J,4)	F(J,5)	F(J,6)
.126764844	.039499114	.434097178	.093010661	.000000000	.000000000
.021624949	.014954778	.495612491	.154382702	.000210052	.000406401
.003573654	.004301107	.451826047	.221787030	.002009307	.004822862
.000318527	.000584634	.329962902	.328326005	.008973405	.025947694
.000000000	.000000000	.175288545	.376384609	.028911033	.124049597
.000000000	.000000000	.057340905	.180722206	.060610569	.398413452

Figure 5-4. Original ill-conditioned configuration factor matrices for a spherical radiometer (above) and a horizontal plate radiometer (below). (BRM)

The following equations will be used to discuss the results obtained in this illustration. Eqs. (5-29c), (5-30b), and (5-42) through (5-45) are rewritten and renumbered here, respectively, in order to facilitate reference to them.

$$F\{Wro\} = \{P\} \tag{5-65}$$

$$F^{-1}\{P\} = \{Wro\} \tag{5-66}$$

$$F^{-1}\{P'\} = F^{-1}\{P + \delta P\} = \{Wro'\} = \{Wro + \delta Wro\} \tag{5-67}$$

$$F^{-1}\{\delta P\} = \{\delta Wro\} \tag{5-68}$$

$$F_{wc}^{-1}\{P\} = \{Wro^{(1)}\} = \{Wro + \delta Wro'\} \tag{5-69}$$

$$F_{wc}^{-1}\{P'\} = F_{wc}^{-1}\{P + \delta P\} = \{Wro''\} = \{Wro + \delta Wro''\} \tag{5-70}$$

Using the configuration factor matrices shown in Figure 5-4 and the Wro values of the six regions of Figure 5-3 in Eq.(5-65) one obtains the two column power matrices, one for the sphere and one for the plate, which are displayed in Table 5-1. The elements of the power matrices in this table are the exact power values, that is, they do not contain uncertainties. Hence, when the inverses of the two original matrices shown in Figure 5-4 operate on the corresponding power matrices {P} of Table 5-1 in accordance with Eq.(5-66),

Table 5-1 Power column matrices {P} obtained for the sphere and plate radiometers. (BRM)

Observation No.	Power matrix elements P (W)	
	Sphere	Plate
1	402.726754250	293.901994233
2	371.161717506	271.908959494
3	357.928570698	263.792636358
4	342.983272546	253.115921135
5	313.277803126	231.460905826
6	254.257613163	181.663189538

the column matrix {Wro} is obtained. The Wro elements of this matrix match the original Wro values shown in Figure 5-3 to at least six decimal places. The accuracy of this computation implies that no significant truncation errors are introduced by the subroutine used to accomplish the matrix inversions.

The effects that observational errors have upon the results were investigated in exactly the same manner as was done in the case of LWR. That is, it was accomplished by simulating thirty sets of power measurements by each radiometer from the six points of observation pictured in Figure 5-3. The new power measurements including uncertainties (for both radiometers) were simulated by perturbing the exact power values shown in Table 5-1 with three types of instrumental errors δP as follows: a) Gaussian random, b) systematic, c) combinations of Gaussian and systematic. The sigma value of the Gaussian errors was 0.5 W, while the systematic errors ranged from -0.9 to 0.9 W. Ten satellite passes making six measurements in each pass by each radiometer, and for each of the

three types of instrumental uncertainties were simulated. Hence, a total of thirty satellite passes making six radiometer measurements in each pass were simulated.

The perturbed powers $P' = P + \delta P$ constitute the elements of the new power column matrices $\{P'\} = \{P + \delta P\}$ for each set of six measurements simulated for both types of radiometers. The matrices F^{-1}, which are the inverses of the original ill-conditioned matrices in Figure 5-4 were multiplied with the new perturbed power matrices $\{P'\}$ in accordance with Eq.(5-67) to obtain $\{Wro'\}$. The errors δWro in this equation are obtained by subtracting the original Wro values from the corresponding new Wro' results. These errors can also be obtained by operating on $\{\delta P\}$ with the inverse matrix F^{-1} in accordance with Eq.(5-68). This is done for both types of radiometers. The rms's of the δWro errors of each region for each set of ten satellite passes for each of the three types of uncertainties were then computed. These rms's are displayed in lines 1, 4, and 7 of Table 5-2 for the sphere, and of Table 5-3 for the plate.

From the results shown in line #4 of both of the above tables, it is seen that systematic power uncertainties do not produce large δWro errors, just as was true in the LWR case. The largest rms value in line #4 is 0.8 W/m^2 for the sphere and 1.1 W/m^2 for the plate. However, from lines 1 and 7 of the same tables, it is clear that Gaussian random power uncertainties are highly magnified by the inverse matrices F^{-1} of both radiometers. Only region #3 has acceptable values (below 15 W/m^2) in lines 1 and 7 in both tables. Region#5 has the largest rms values in these two lines, namely, 350.5 W/m^2

Table 5-2. Rms's of the δWro, δWro" and δWr" errors obtained with the original and the stabilized inverse matrices of a spherical radiometer. (BRM)

Power uncertainties	Spread	Error type	Rms's of the δWro, δWro" and δWr" errors (W/m^2)					
			Region 1	Region 2	Region 3	Region 4	Region 5	Region 6
Gaussian random	σ=0.5 W	δWro	41.8	161.5	11.1	18.1	350.3	66.2
Gaussian random	σ=0.5 W	δWro"	18.5	64.6	2.7	1.4	29.4	6.4
Gaussian random	σ=0.5 W	δWr"	16.6	52.9	2.5	1.2	23.5	5.5
Systematic	-.9 to .9 W	δWro	0.6	0.7	0.7	0.7	0.4	0.8
Systematic	-.9 to .9 W	δWro"	11.5	50.7	2.2	1.1	19.3	3.6
Systematic	-.9 to .9 W	δWr"	10.3	41.5	2.1	1.0	15.4	3.1
Gaussian random	σ=0.5 W	δWro	41.6	161.6	11.0	18.3	350.5	66.5
plus		δWro"	17.9	65.2	1.9	2.0	29.6	6.2
systematic	0.9 W	δWr"	16.1	53.4	1.8	1.8	23.7	5.3

Table 5-3. Rms's of the δWro, δWro" and δWr" errors obtained with the original and the stabilized inverse matrices of a horizontal plate radiometer. (BRM)

Power uncertainties	Spread	Error type	Rms's of the δWro, δWro" and δWr" errors (W/m^2)					
			Region 1	Region 2	Region 3	Region 4	Region 5	Region 6
Gaussian random	σ=0.5 W	δWro	53.2	221.1	8.4	15.1	370.7	51.4
Gaussian random	σ=0.5 W	δWro"	23.8	86.7	2.0	1.8	49.8	7.8
Gaussian random	σ=0.5 W	δWr"	21.6	72.0	1.8	1.6	40.5	6.8
Systematic	-.9 to .9 W	δWro	0.8	1.0	0.9	0.9	0.6	1.1
Systematic	-.9 to .9 W	δWro"	9.5	45.9	1.2	0.8	18.9	2.4
Systematic	-.9 to .9 W	δWr"	8.6	38.1	1.1	0.8	15.4	2.1
Gaussian random	σ=0.5 W	δWro	53.1	221.3	8.3	15.4	370.9	51.8
plus		δWro"	23.2	87.4	1.5	2.3	49.9	7.8
systematic	0.9 W	δWr"	21.0	72.5	1.4	2.1	40.6	6.8

for the sphere (line 7 of Table 5-2), and 370.9 W/m^2 for the plate (line 7 of Table 5-3). These results clearly show that the original matrices F of the two radiometers shown in Figure 5-4 are ill-conditioned and that their corresponding inverses F^{-1} are unstable.

Application of the matrix stabilization technique previously described and applied to the case of LWR was used here in an identical fashion. The two resulting well-conditioned matrices are displayed in Figure 5-5. The same optimum cut-off values found for stabilizing the matrices in the LWR case were used here, namely, 0.032 and 0.016. Any element smaller than 0.032 in the configuration factor matrix for the sphere, and smaller than 0.016 in that for the plate is removed and added to the diagonal element in the same row of the element removed.

Comparisons of the elements of the original matrices in Figure 5-4 with the corresponding elements of the well-conditioned matrices in Figure 5-5 indicate that all non-diagonal elements below the cut-off values have been translated along their corresponding rows and added to the diagonal elements in those rows.

Inversion of the two well-conditioned matrices F_{wc} shown in Figure 5-5 produced the inverses F_{wc}^{-1} which were multiplied with the perturbed power column matrices {P'} in accordance with Eq.(5-70). The new errors δWro" obtained per this equation were used to compute new sets of rms's for the six regions and for both radiometers. These new rms's are shown in lines 2, 5, and 8 of Table 5-2 for the sphere and of Table 5-3 for the plate. Comparison of the rms's in line 2 with those of line 1, and those of line 8 with those of line 7

F(J,1)	F(J,2)	F(J,3)	F(J,4)	F(J,5)	F(J,6)
.189686179	.068394333	.543375122	.144790086	.000000000	.000000000
.040528358	.030547386	.628556145	.238738238	.000000000	.000000000
.000000000	.000000000	.610437244	.329356206	.000000000	.000000000
.000000000	.000000000	.437124002	.462662226	.000000000	.049218886
.000000000	.000000000	.247445185	.473557131	.052651685	.189266111
.000000000	.000000000	.092187183	.256772937	.104251122	.501478375

F(J,1)	F(J,2)	F(J,3)	F(J,4)	F(J,5)	F(J,6)
.126764844	.039499114	.434097178	.093010661	.000000000	.000000000
.021624949	.015571231	.495612491	.154382702	.000000000	.000000000
.000000000	.000000000	.466532977	.221787030	.000000000	.000000000
.000000000	.000000000	.329962902	.338202571	.000000000	.025947694
.000000000	.000000000	.175288545	.376384609	.028911033	.124049597
.000000000	.000000000	.057340905	.180722206	.060610569	.398413452

Figure 5-5. Well-conditioned configuration factor matrices for a spherical radiometer (above) and a horizontal plate radiometer (below). (BRM)

is indicative of the excellent results obtained with the matrix stabilization technique. For example, the highest rms value for the sphere was found in region 5 as mentioned previously. This rms value of 350.5 W/m^2 (line 7) was drastically reduced to 29.6 W/m^2 (line 8). Region 5 also had the highest rms value in the case of the plate. This value which was 370.9 W/m^2 (line 7) became 49.9 W/m^2 (line 8). Similarly, region 2 in the case of the sphere had an rms value of 161.6 W/m^2 in line 7 of Figure 5-2 which was reduced to 65.2 W/m^2 (line 8). For the plate, the corresponding rms value in Table 5-3 was 221.3 W/m^2 (line 7 , region 2) which was brought down to 87.4 W/m^2.

It should be pointed out that the stabilization scheme increases the δWro errors due to systematic power uncertainties. As seen from a comparison of the rms values in lines 4 and 5 of Tables 5-2 and 5-3, the error increase is notable for regions 1, 2, and 5. The new rms values of these regions are 11.5, 50.7 and 19.3 W/m^2 for the sphere (Table 5-2), and 9.5, 45.9 and 18.9 W/m^2 for the plate (Table 5-3). The error increase for regions 3, 4 and 6 is not as significant. These regions have the following new rms values: a) 2.2, 1.1, and 3.6 W/m^2 for the sphere, b) 1.2, 0.8 and 2.4 W/m^2 for the plate. It will be shown soon that according to the results obtained with the prediction technique, the results obtained for regions 3, 4 and 6 are considered acceptable, while those obtained for regions 1, 2 and 5 are unreliable due to lack of sufficient information from these regions. Consequently, the error increments, (although large) introduced by the matrix stabilization technique

into the results of regions 1, 2 and 5 have no significance in the final analysis since in any case the results of these regions will be shown to be unacceptable.

Rows 3, 6 and 9 in Tables 5-2 and 5-3 deserve special attention. The data in these rows have no counterpart in the LWR case. These data are the rms's of the $\delta Wr''(\zeta)$ errors that are computed from the rms's of the $\delta Wro''$ errors appearing in lines 2, 5 and 8 according to Eq.(5-49). This equation is rewritten here in the modified form used to obtain

$$[\delta Wr''(\zeta)]_{rms} = \frac{S_k}{St_k} [\delta Wro'']_{rms} \tag{5-71}$$

The values of the ratios S_k/St_k for the six regions for both radiometers are given in Table 5-4 below. Using these ratios, two examples will be discussed.

Table 5-4. Values of the ratio S_k/St_k for the six regions and for both radiometers. (BRM)

Radiometer	R1	R2	R3	R4	R5	R6
Sphere	0.896	0.819	0.934	0.909	0.799	0.863
Plate	0.905	0.830	0.927	0.910	0.813	0.871

The value 1.8 for region 3 in row 9 of Table 5-2 is obtained by multiplying the value 1.9 immediately above it by 0.934. This last factor is the value of S_k/St_k for the sphere and region 3 in Table 5-4. Similarly, 1.4, the corresponding value for the plate in Table 5-3 is obtained by multiplying the value above it (1.5) by 0.927 from Table 5-4.

All the values of S_k/St_k in Table 5-4 are less than one. This indicates that the rms's of the $\delta Wr''(\zeta)$ errors are smaller than the rms's of the $\delta Wro''$ errors. Because of this, it is believed unnecessary to include the rms's of the $\delta Wr''(\zeta)$ errors in the data tables of the diffuse reflection case to be discussed later.

Figures 5-6 and 5-7 display the curves of the rms's of the δWro and $\delta Wro''$ errors (derived from combinations of Gaussian and systematic power uncertainties) versus the regional configuration factor S_k of each region for the sphere and plate, respectively. These figures show the remarkable contrast between the curves obtained with the unstable and with the stabilized inverse matrices. As defined previously, S_k is the sum of the shape factors that the kth region contributed to all six observations and is referred to as the regional configuration factor of the kth region. The curves in Figures 5-6 and 5-7 are plots of the data appearing in the 7th and 8th rows of Tables 5-2 and 5-3 previously presented.

An additional method of showing the striking difference between the original ill-conditioned matrices F and the new well-conditioned matrices F_{wc} is by comparing their condition numbers. The values of this parameter are displayed in Table 5-5 for both radiometers. From the last column, it is seen that the values of the condition numbers dropped from 1192 to 134 for the sphere, and from 987 to 190 for the plate. The significant reduction in the values of this parameter for both radiometers clearly indicates the effectiveness of the matrix stabilization technique developed just as was shown to be the case in the LWR application.

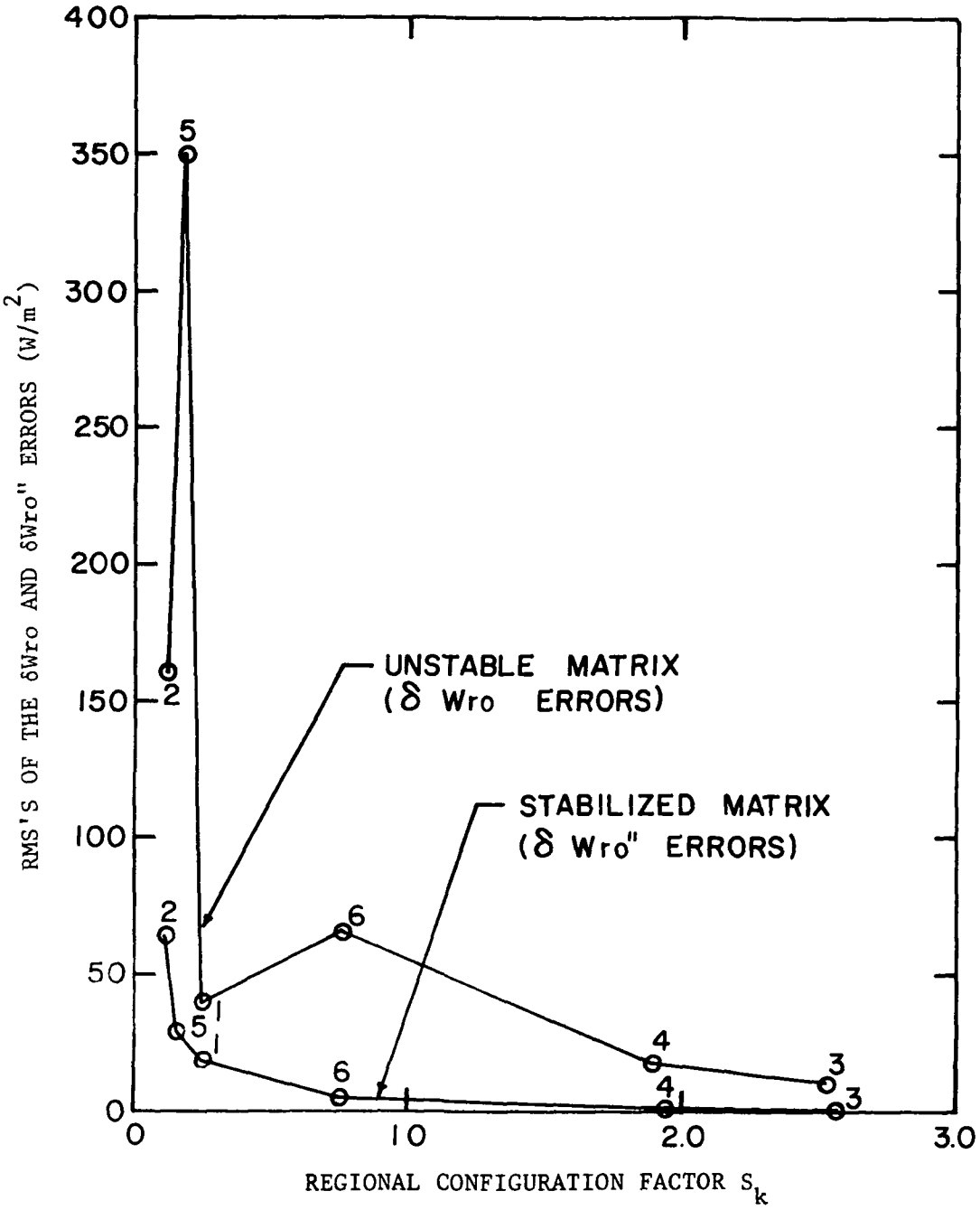

Figure 5-6. Rms's of the Errors δWro and δWro" (Derived from Gaussian and Systematic Uncertainties) for the Six Regions with the Unstable and Stabilized Inverse Matrices of a Spherical Radiometer. (BRM)

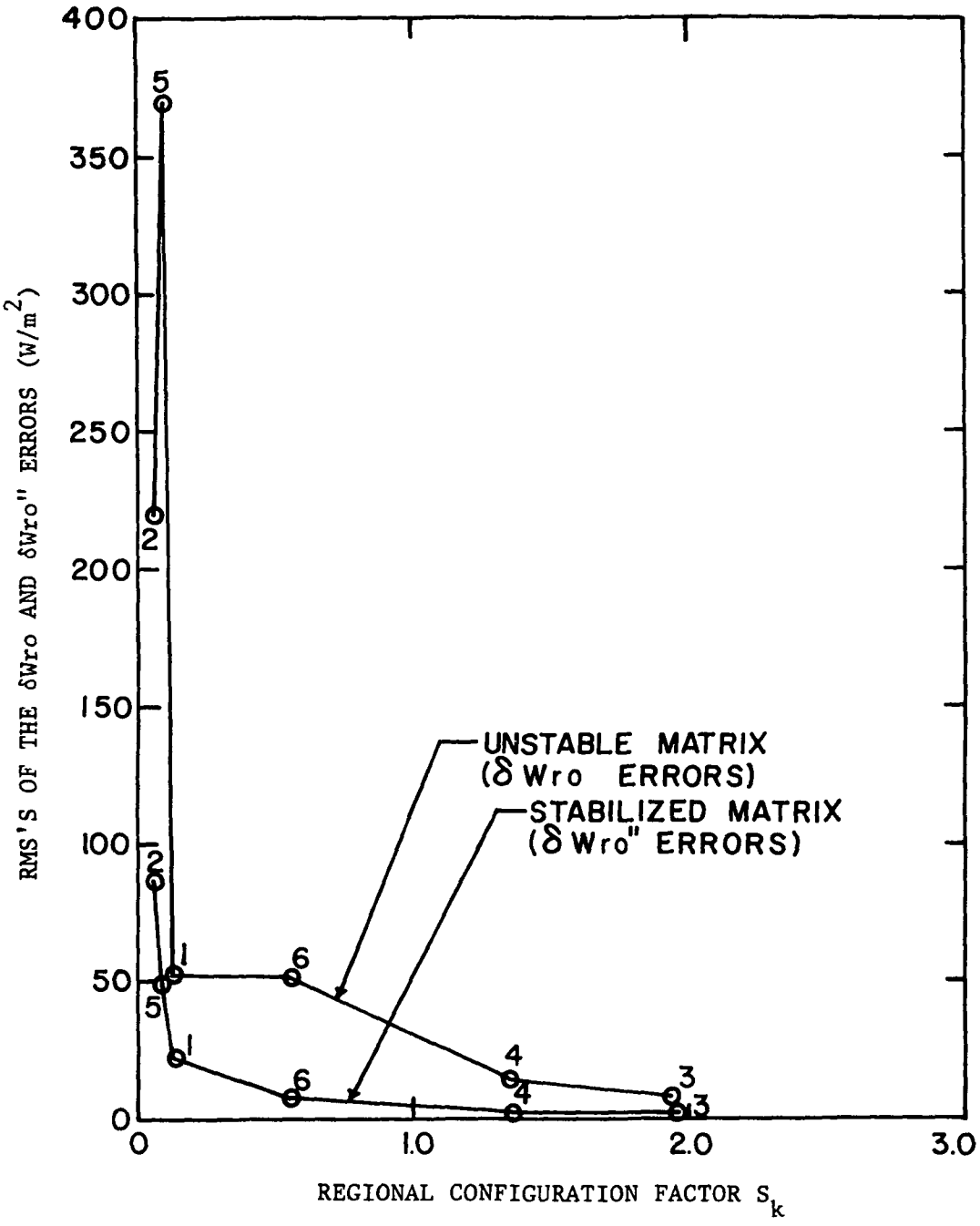

Figure 5-7. Rms's of the Errors δWro and δWro" (Derived from Gaussian and Systematic Uncertainties) for the Six Regions with the Unstable and Stabilized Inverse Matrices of a Horizontal Plate Radiometer. (BRM)

Table 5-5. Condition numbers of the original, ill-conditioned and the new, well-conditioned configuration factor matrices for both types of radiometer, spherical and horizontal plate. (BRM)

Radiometer	Matrix F	Matrix F^TF	Eigenvalues μ of F^TF		Condition number
			μ_{max}	μ_{min}	
Sphere	Original, F	F^TF	1.845019494	0.000001298	1192
Sphere	Well-conditioned, F_{wc}	$F_{wc}^T F_{wc}$	1.887796292	0.000104577	134
Plate	Original, F	F^TF	1.045866846	0.000001073	987
Plate	Well-conditioned, F_{wc}	$F_{wc}^T F_{wc}$	1.061700938	0.000082767	190

The instantaneous technique was also applied to a SWR field which was assumed to be described by a DIF model. As explained before, the parameter $R_2(\theta,\psi,\zeta) = r(\zeta)/\pi\rho(\theta,\psi,\zeta) = 1$ in this model. This case was treated in the same manner as the BRM case just discussed. The rms's of the δWro errors obtained with the unstable matrices, as well as the rms's of the δWro" errors calculated with the stabilized matrices are displayed in Table 5-6 for the sphere and in Table 5-7 for the plate. As in the case of the BRM, and also as in the case of LWR, lines 2, 4 and 6 of both tables show acceptable results for regions 3, 4 and 6 for both types of radiometers.

Figures 5-8 and 5-9 exhibit the curves of the rms's of the δWro and δWro" errors (derived from combinations of Gaussian and systematic uncertainties) versus the regional configuration factor S_k of each region for the sphere and plate, respectively. These figures show the significant difference between the curves obtained with the unstable and with the stabilized matrices. Comparing the curves in Figures 5-8 and 5-9 for the DIF case with those in Figures 5-6 and 5-7 for the BRM case, one can see that the stabilization scheme produces excellent results in both applications.

The prediction parameter PP was introduced in the LWR case and its definition was given by Eq.(4-36) which is here rewritten and renumbered for easy reference.

$$PP = (S_k \, F_{jj}/\Sigma_j) \times 1000 \qquad (5\text{-}72)$$

where S_k is the regional configuration factor of the kth region, F_{jj} is the diagonal element in the jth row of the configuration factor matrix F, and Σ_j is the sum of the elements in the jth

Table 5-6. Rms's of the δWro and δWro" errors obtained with the original and stabilized inverse matrices of a spherical radiometer. (Diffuse model)

Power uncertainties	Spread	Matrix	Rms's of δWro and δWro" errors (W/m^2)					
			Region 1	Region 2	Region 3	Region 4	Region 5	Region 6
Gaussian random	σ=0.5 W	Original	40.5	179.4	12.6	24.4	315.5	58.7
Gaussian random	σ=0.5 W	Stabilized	15.6	57.1	1.6	1.6	32.5	6.7
Systematic	-.9 to .9 W	Original	0.6	0.7	0.6	0.7	0.1	0.7
Systematic	-.9 to .9 W	Stabilized	5.9	31.3	0.9	0.9	30.8	5.5
Gaussian random plus systematic	σ=0.5 W 0.9 W	Original	40.4	179.6	12.5	24.6	315.5	59.0
		Stabilized	15.2	57.5	1.2	1.4	33.1	6.1

Table 5-7. Rms's of the δWro and δWro" errors obtained with the original and stabilized matrices of a horizontal plate radiometer. (Diffuse model)

Power uncertainties	Spread	Matrix	Rms's of δWro and δWro" errors (W/m^2)					
			Region 1	Region 2	Region 3	Region 4	Region 5	Region 6
Gaussian random	σ=0.5 W	Original	50.4	233.9	8.6	18.1	323.4	44.2
Gaussian random	σ=0.5 W	Stabilized	22.4	89.1	1.6	2.1	43.9	6.8
Systematic	-.9 to .9 W	Original	0.8	1.2	0.8	0.9	0.2	1.0
Systematic	-.9 to .9 W	Stabilized	4.6	26.9	0.7	1.0	30.3	3.8
Gaussian random plus systematic	σ=0.5 W 0.9 W	Original	50.2	179.6	12.5	24.6	315.5	59.0
		Stabilized	22.0	89.6	1.6	2.1	44.3	6.4

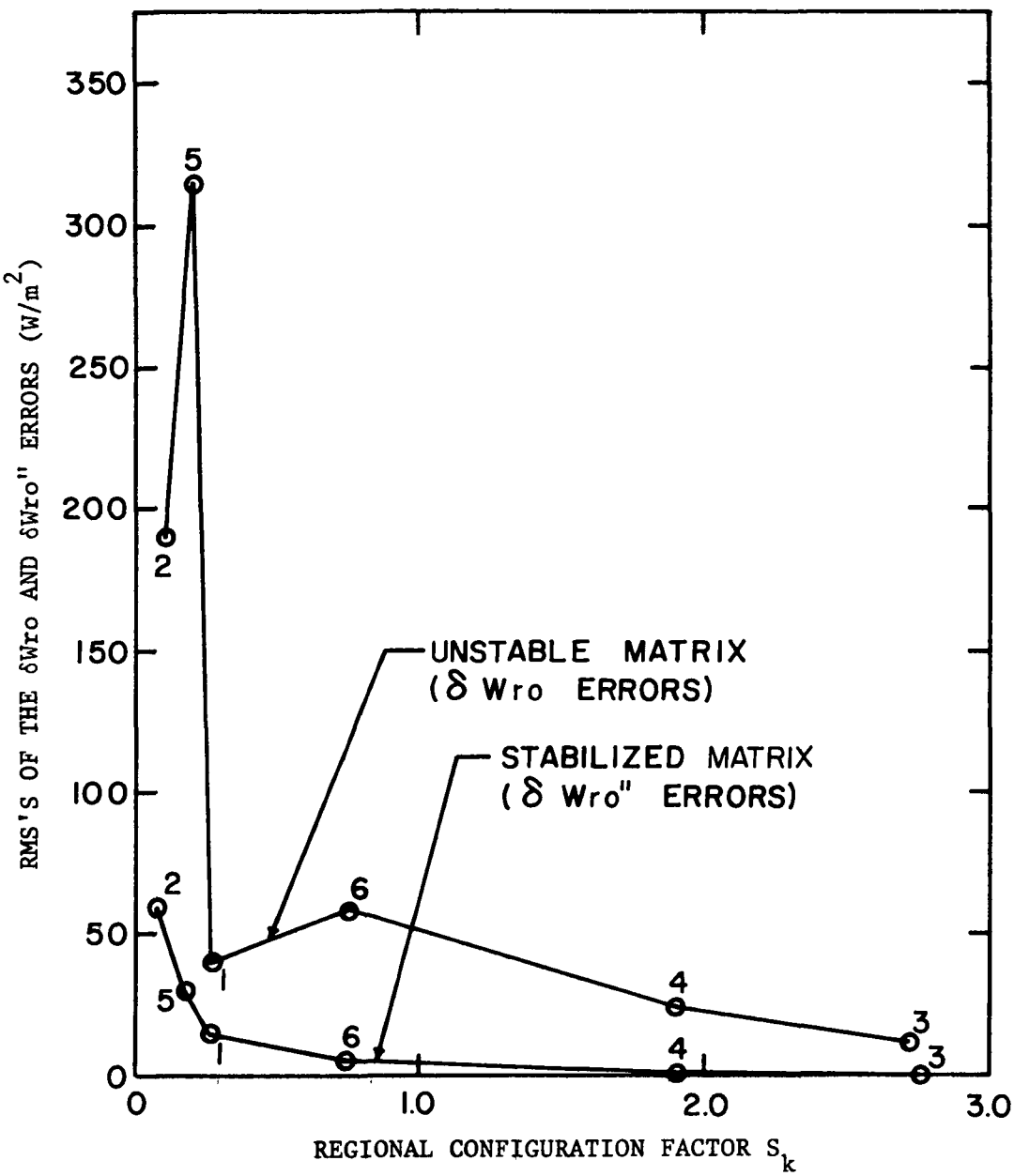

Figure 5-8. Rms's of the Errors δWro and δWro" (Derived from Gaussian and Systematic Uncertainties) for the Six Regions with the Unstable and Stabilized Inverse Matrices of a Spherical Radiometer. (DIF)

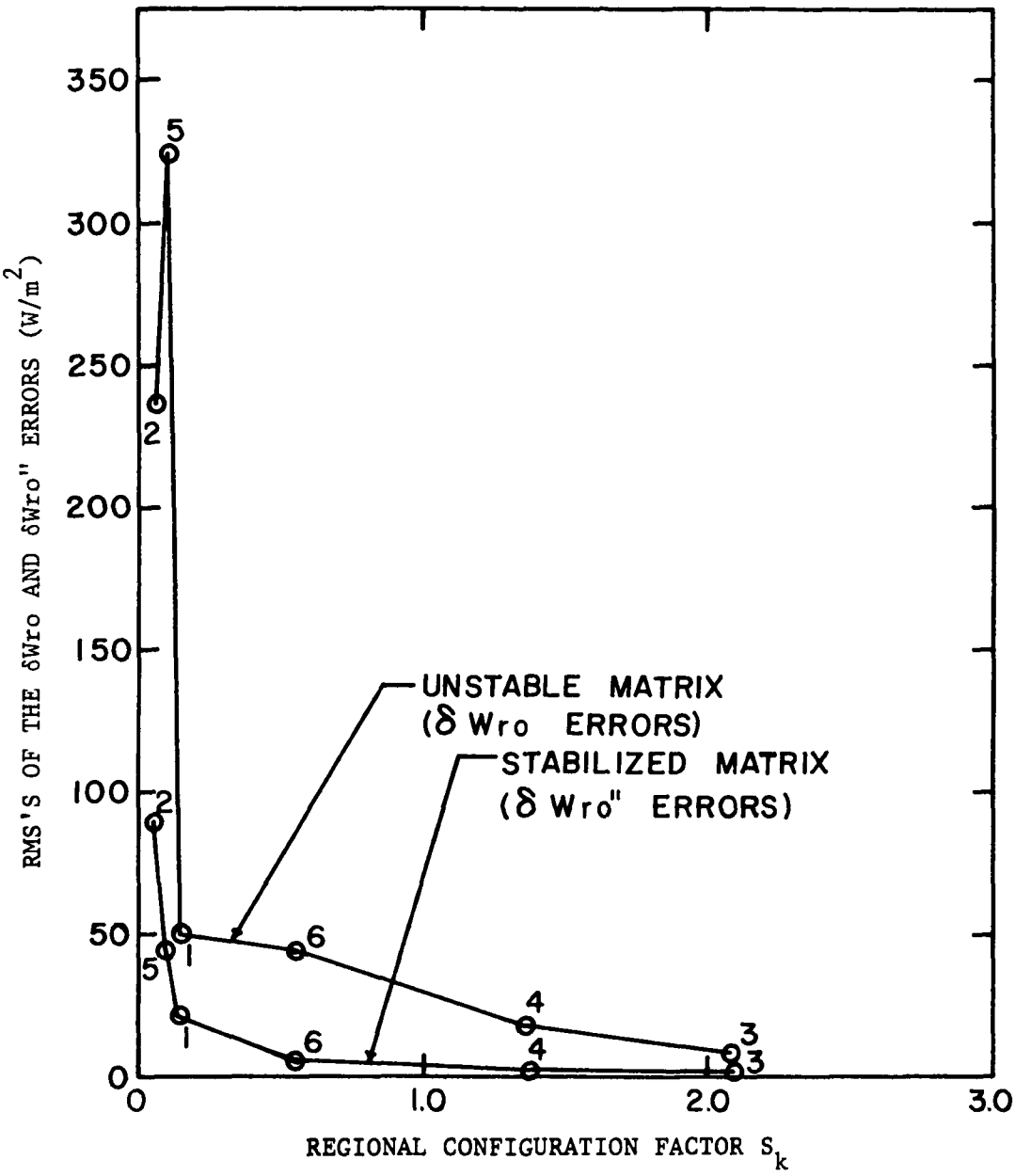

Figure 5-9. Rms's of the Errors δWro and δWro" (Derived from Gaussian and Systematic Uncertainties) for the Six Regions with the Unstable and Stabilized Inverse Matrices of a Horizontal Plate Radiometer. (DIF)

row of this same matrix F. The cut-off values determined for this parameter in the case of LWR were found to be applicable also in the SWR case, as will be shown later. These cut-off values of PP are 150 for the sphere and 100 for the plate.

Figures 5-10 and 5-11 are plots of the rms's of the δWro" errors for the BRM case (derived from Gaussian plus systematic power errors) of the six regions versus the values of PP for these regions for the sphere and plate, respectively. In both figures, regions 3, 4 and 6 show rms values of less than 8 W/m^2, while regions 1, 2 and 5 show rms values of 20 W/m^2 or greater. The gap in the value of PP between these two groups is at least 250. The broken vertical lines denote the cut-off values of PP (150 for the sphere and 100 for the plate) already discussed. Hence, according to these cut-off values, the prediction scheme indicates that only the results of regions 3, 4 and 6 are to be considered acceptable, while those of regions 1, 2 and 5 should be considered unreliable for lack of sufficient information from these regions. These predictions, as one sees from these curves, agree with the rms's of the δWro" errors obtained from simulation experiments of several satellite observations. Data gathered during different satellite passes which include sufficiently large sections of the three rejected regions (1, 2 and 5) yield results that are acceptable for these regions as will be shown soon.

Figures 5-12 and 5-13 show plots for the DIF model case which are the equivalent of those exhibited in Figures 5-10 and 5-11 for the case of the BRM. Again here, the PP cut-off values of 150 for the sphere and 100 for the plate predict that only the results of

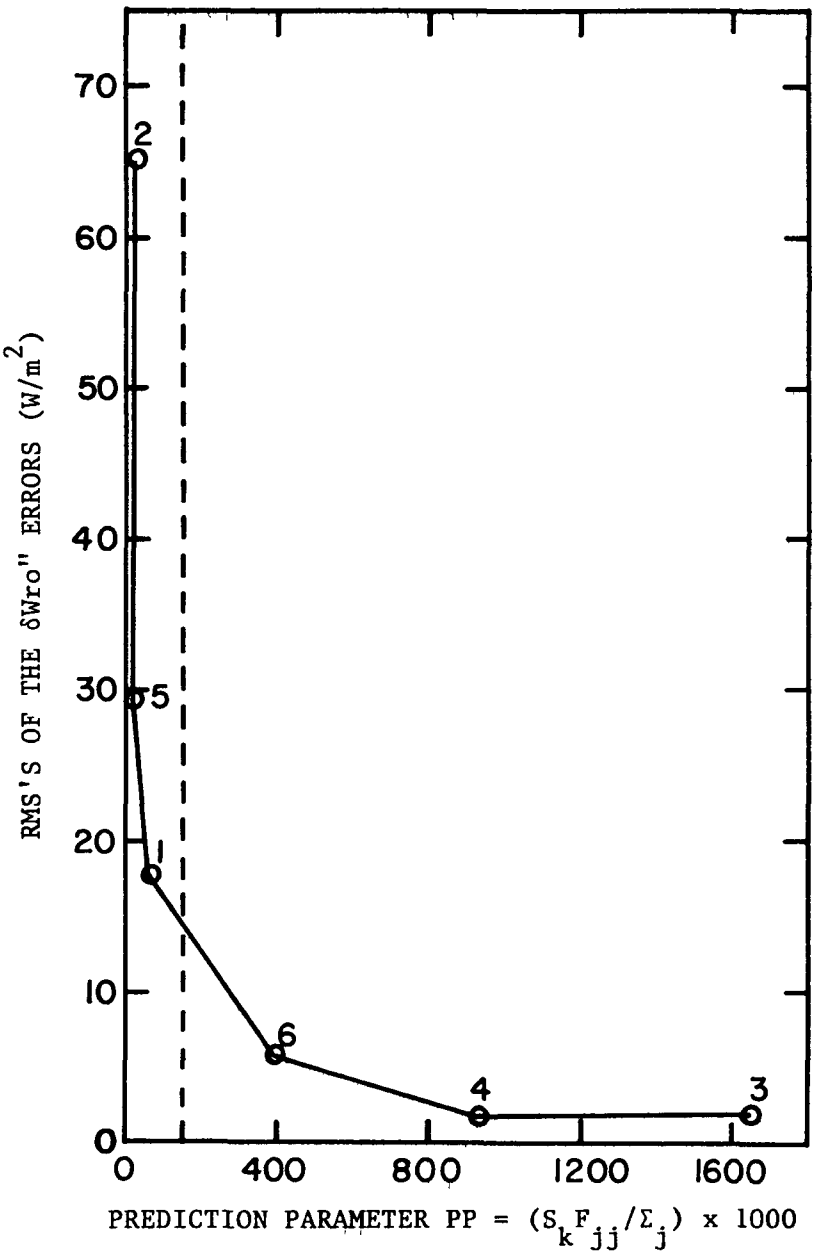

Figure 5-10. Relationship between the Prediction Parameter and the Rms's of the δWro" Errors Obtained with the Stabilized Inverse Matrix of a Spherical Radiometer. (BRM)

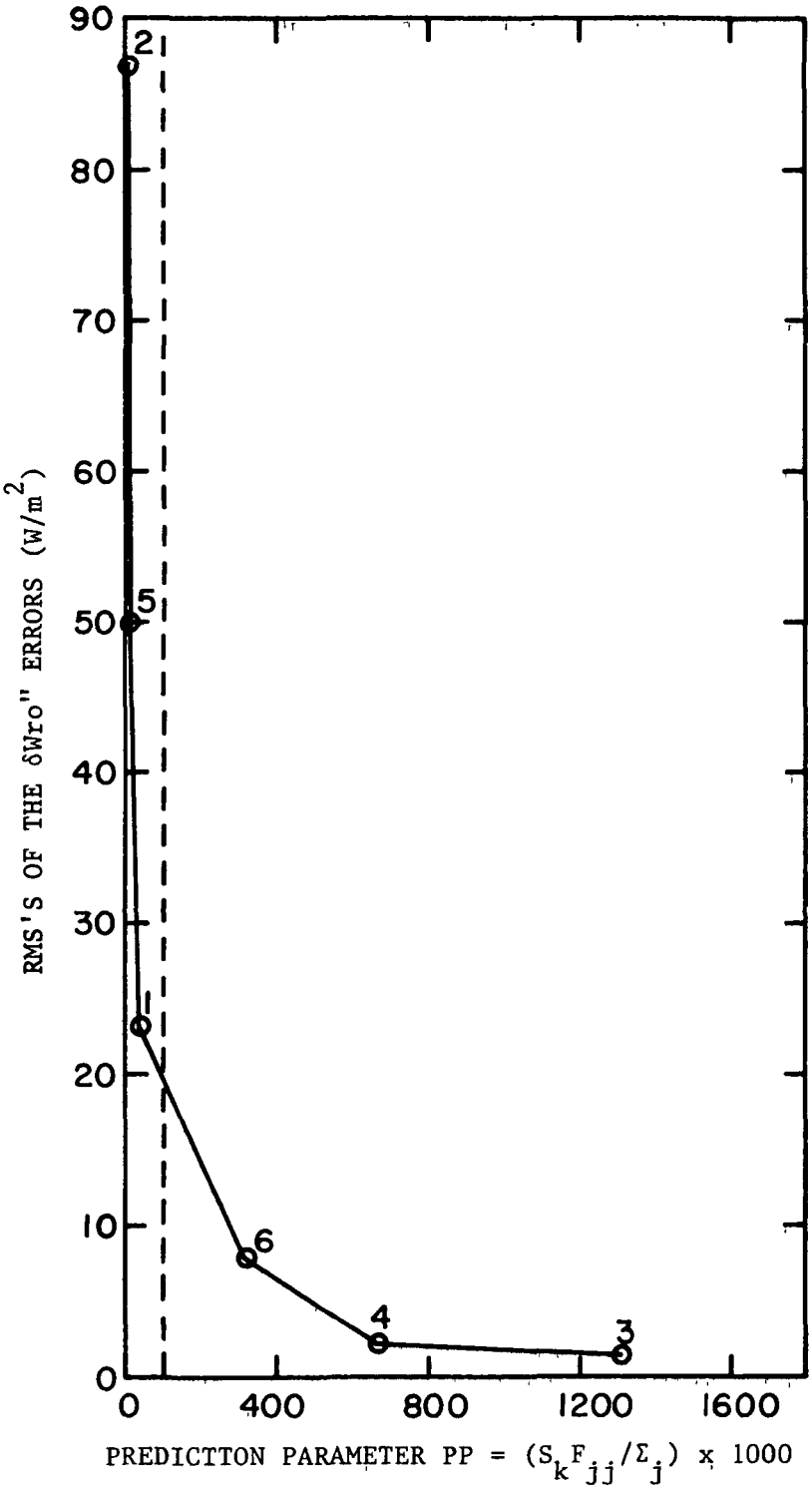

Figure 5-11. Relationship between the Prediction Parameter and the Rms's of the δWro" Errors Obtained with the Stabilized Inverse Matrix of a Horizontal Plate Radiometer. (BRM)

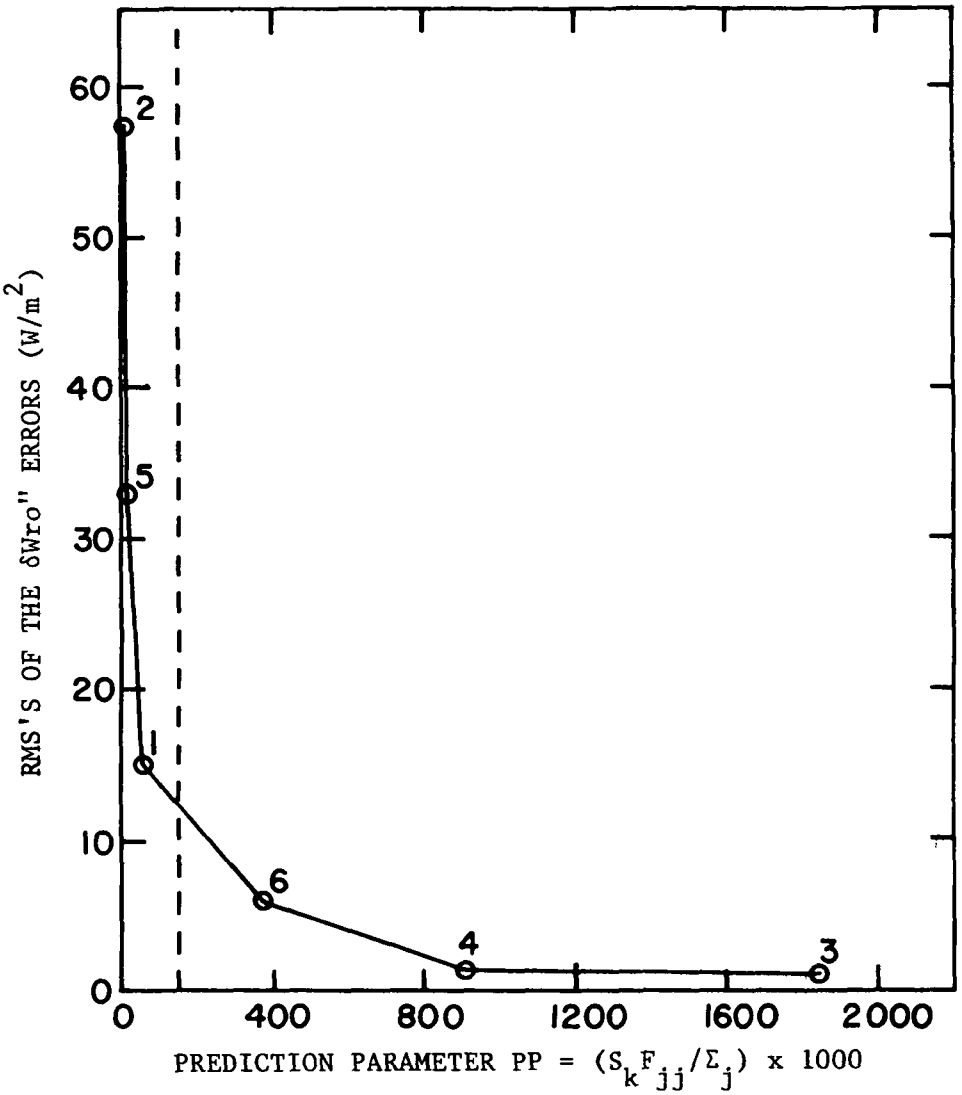

Figure 5-12. Relationship between the Prediction Parameter and the Rms's of the δWro" Errors Obtained with the Stabilized Inverse Matrix of a Spherical Radiometer. (DIF)

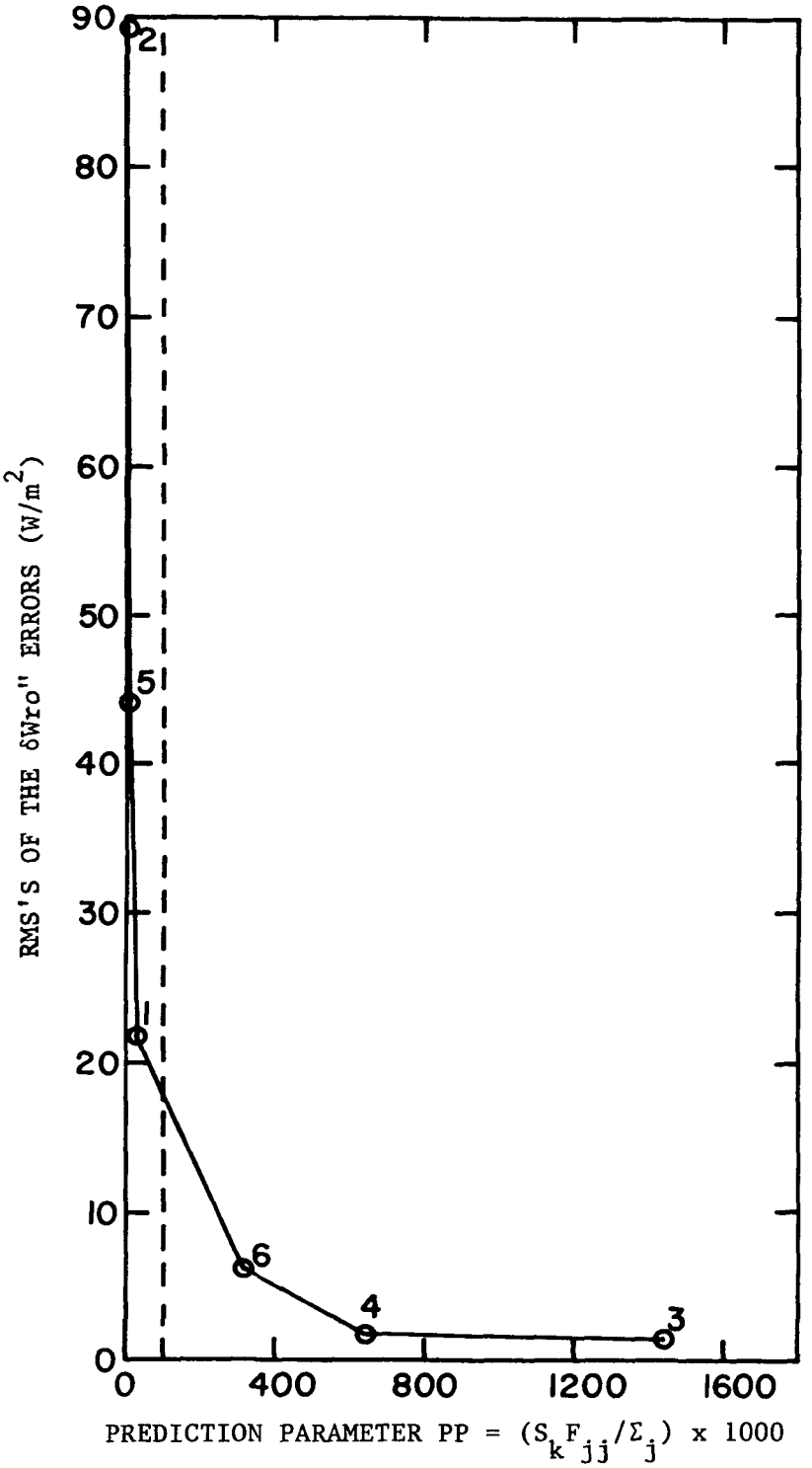

Figure 5-13. Relationship between the Prediction Parameter and the Rms's of the δWro" Errors Obtained with the Stabilized Inverse Matrix of a Horizontal Plate Radiometer. (DIF)

regions 3, 4 and 6 are acceptable. This is easily verified by observing that the rms's of the δWro" errors of these regions are less than 15 W/m^2 in both figures, while those of regions 1, 2 and 5 are above 15 W/m^2.

As was stated in the LWR case, it was necessary to develop the matrix stabilization and prediction techniques for use in conjunction with the instantaneous technique only because the portions observed of some of the regions were too small. Hence, as was proven in the case of the LWR, if the satellite positions are selected so as to observe sufficiently large sections of all the regions under study, then the results obtained with the original matrices of both radiometers would be acceptable. There would then be no need for using any matrix stabilization techniques or prediction schemes.

The same satellite positions selected in the LWR case to observe sufficiently large portions of all regions were used in the SWR case. The rms's of the δWro errors calculated with the original matrices and the rms's of the δWro" errors obtained with the stabilized matrices are displayed in Table 5-8 for the sphere and 5-9 for the plate. From rows 1, 3 and 5 in these tables it is seen that the results obtained with the original matrices for all six regions are acceptable. The highest rms value is 3.4 W/m^2 for the sphere (region 2, row 5, Table 5-8), and 4.1 W/m^2 (same region and row of Table 5-9). It is also seen from lines 2, 4 and 6 of both tables that in those instances in which the stabilized matrices produce an improved result, the improvement is negligible.

Table 5-8. Rms's of the δWro and δWro" errors obtained with the original and stabilized inverse matrices of a spherical radiometer. Adequate portions of all regions are observed by judicious selection of satellite positions. (BRM)

Power uncertainties	Spread	Matrix	Rms's of the δWro and δWro" errors (W/m^2)					
			Region 1	Region 2	Region 3	Region 4	Region 5	Region 6
Gaussian random	σ=0.5 W	Original	2.4	3.4	1.9	2.8	1.4	1.4
Gaussian random	σ=0.5 W	Stabilized	2.7	2.9	2.7	2.4	1.8	1.3
Systematic	-.9 to .9 W	Original	0.6	0.7	0.7	0.6	0.6	0.7
Systematic	-.9 to .9 W	Stabilized	2.5	0.7	1.8	0.5	1.6	0.7
Gaussian random plus systematic	σ=0.5 W	Original	2.4	3.4	2.1	3.1	1.7	1.5
	0.9 W	Stabilized	3.3	3.0	2.1	2.6	2.4	1.5

Table 5-9. Rms's of the δWro and δWro" errors obtained with the original and stabilized matrices of a horizontal plate radiometer. Adequate portions of all regions are observed by judicious selection of satellite positions. (BRM)

Power uncertainties	Spread	Matrix	Rms's of the δWro and δWro" errors (W/m^2)					
			Region 1	Region 2	Region 3	Region 4	Region 5	Region 6
Gaussian random	σ=0.5 W	Original	2.8	4.0	2.1	3.2	1.5	1.5
Gaussian random	σ=0.5 W	Stabilized	2.6	3.6	2.3	2.8	1.5	1.4
Systematic	-.9 to .9 W	Original	0.9	0.9	0.9	0.9	0.8	0.9
Systematic	-.9 to .9 W	Stabilized	1.8	1.1	1.1	0.7	1.2	1.0
Gaussian random plus systematic	σ=0.5 W 0.9 W	Original	2.8	4.1	2.3	3.7	1.9	1.8
		Stabilized	3.1	3.8	1.9	3.2	2.2	1.8

The data in the fifth row of Tables 5-8 and 5-9 were plotted versus the corresponding values of PP for the six regions. These plots are displayed in Figure 5-14 for the sphere and 5-15 for the plate. It is seen that the PP values of all regions in Figure 5-14 are above the cut-off value of 150, except for region 2 whose PP value fell just below this mark. Its value is 148. Thus, for all practical purposes, the cut-off value of 150 introduced for the sphere in the LWR case is still applicable in this instance. The PP values of all six regions in Figure 5-15 are greater than 100 which is the cut-off value determined for the plate in the LWR case and which is also applicable in this case.

The effects on the results caused when an improper BRM was used during data interpretation were evaluated as follows. First, a set of six power measurements of a SWR field described by a BRM was simulated, and the powers were computed using the correct BRM. These powers are the ones displayed in Table 5-1 for the sphere and plate for the BRM case discussed previously. These powers were then perturbed in the same manner as was done for the case of the BRM. In that case, the BRM was used during interpretation of the data. Now, however, a DIF model is assumed during data interpretation. That is, the perturbed power matrices were multiplied with the inverse matrices derived for a DIF model case.

Table 5-10 shows the rms's of the the δWro" errors for the case just described for a spherical radiometer. These rms values were calculated as follows. The information obtained by observing a SWR field which is described by a BRM was processed under the assumption

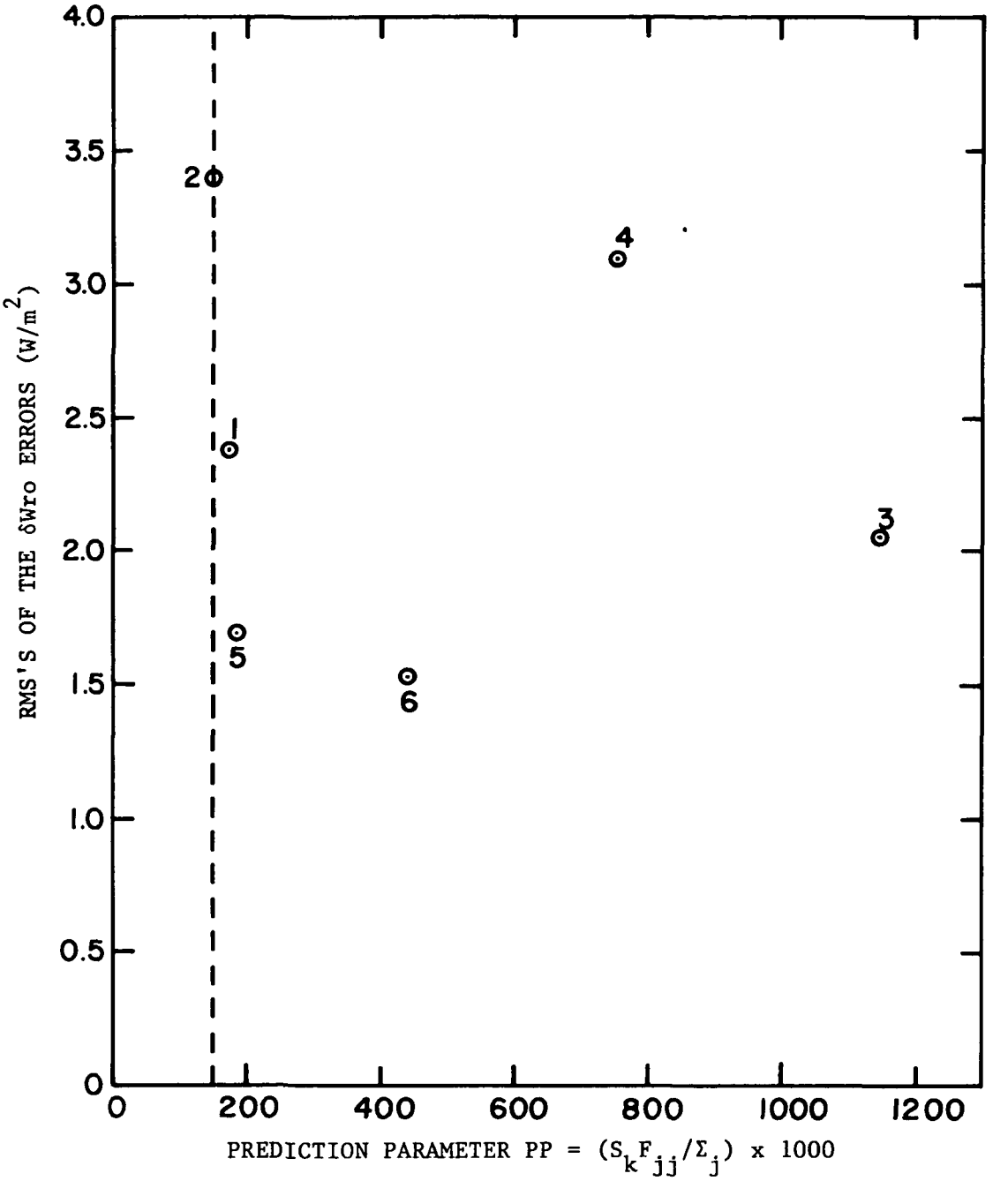

Figure 5-14. Relationship between the Prediction Parameter and the Rms's of the δWro Errors Obtained with the Inverse Matrix of a Spherical Radiometer. Adequate Portions of All Regions Are Observed by Judicious Selection of Satellite Positions. (BRM)

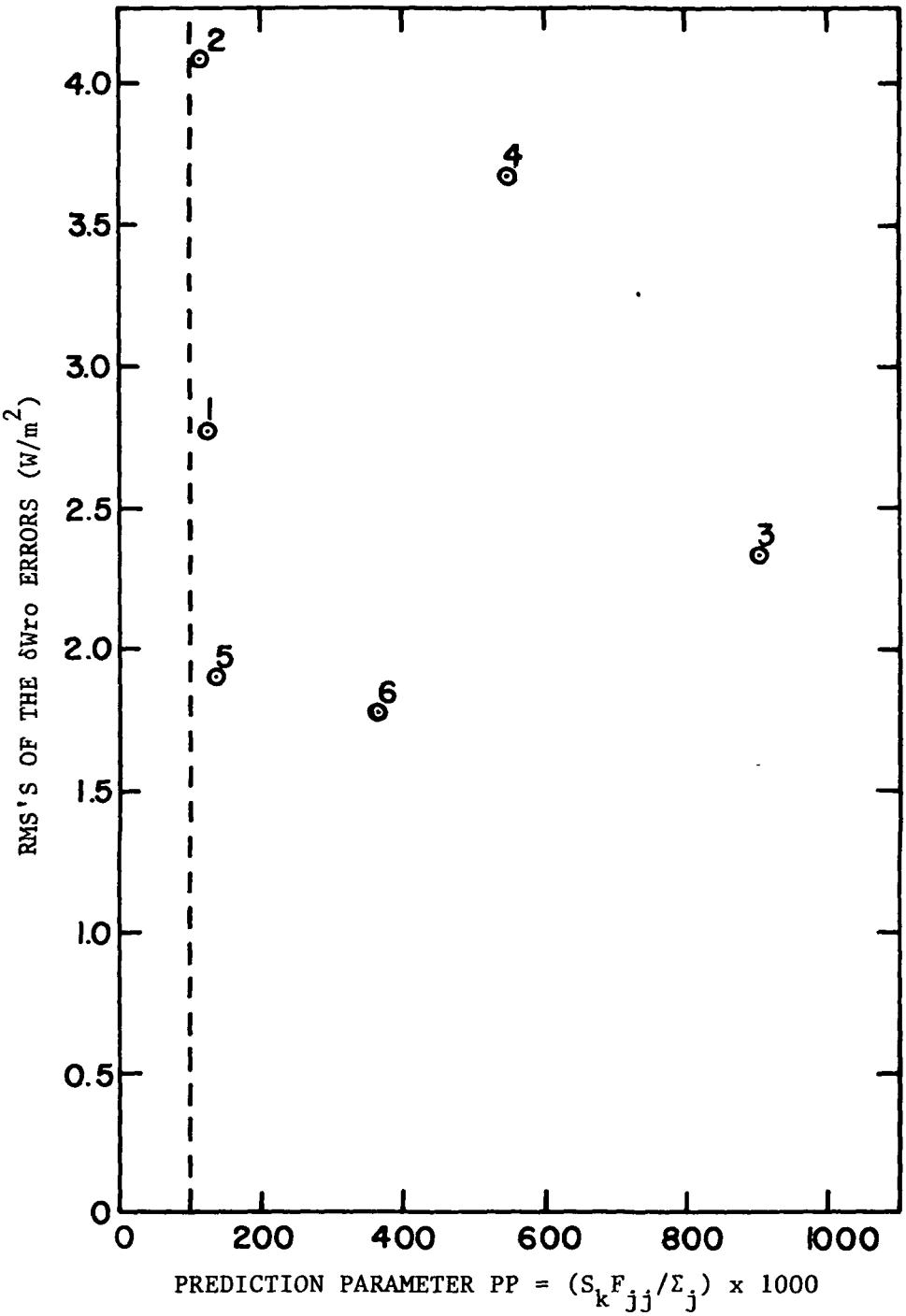

Figure 5-15. Relationship between the Prediction Parameter and the Rms's of the δWro Errors Obtained with the Inverse Matrix of a Horizontal Plate Radiometer. Adequate Portions of All Regions Are Observed by Judicious Selection of Satellite Positions. (BRM)

Table 5-10. Rms's of the δWro" errors obtained when the stabilized inverse matrix of a spherical radiometer derived for a diffuse reflectance model (DIF) was then applied to a Wr field which is described by a bidirectional reflectance model. (BRM/DIF)

Power uncertainties	Spread	Rms's of the δWro" errors (W/m^2)					
		Region 1	Region 2	Region 3	Region 4	Region 5	Region 6
Gaussian random	σ=0.5 W	13.3	81.6	33.0	1.4	44.4	10.1
Systematic	-.9 to .9 W	2.2	70.5	32.7	0.5	45.1	9.8
Combination of Gaussian random and systematic	σ=0.5 W 0.9 W	13.4	80.9	32.2	1.6	45.1	9.3

that it was derived from a radiation field described by a diffuse reflection model. Two important points should be noted from the results in Table 5-10: a) region 3, which had an acceptable rms error of 1.9 W/m^2 (Table 5-2, line 8) when the correct BRM was used during data interpretation, now has an unacceptable value of 32.2 W/m^2 (Table 5-10, line 3); b) region 1, which had an unacceptable rms error of 17.9 W/m^2 (Table 5-2, line 8), now has an acceptable value of 13.4 W/m^2. These results are absurd since region 3 has the largest S_k value (2.56), while the S_k value of region 1 (0.23) is one of the smallest. Hence, use of an incorrect BRM during data interpretation, such as application of a diffuse reflection model, can produce results which may be unreliable.

Figure 5-16 serves to depict the discrepancy now existing in the above situation. The prediction scheme indicates as before that regions 3, 4 and 6 should have acceptable results since they have large S_k values and large PP values. However, the rms of the $\delta Wro''$ error of region 3 is above 30 W/m^2. Region 1 has an rms value of less than 15 W/m^2, but since the S_k value is small, its PP value is also small and it is predicted to have unreliable results for lack of sufficient data from this region.

The three SWR cases investigated with the instantaneous technique are:

1. BRM/BRM: A field described by a BRM is interpreted by using the correct BRM.

2. DIF/DIF: A diffuse reflection field is interpreted as such.

3. BRM/DIF: A field described by a BRM is erroneously interpreted by assuming it to be a diffuse reflection field.

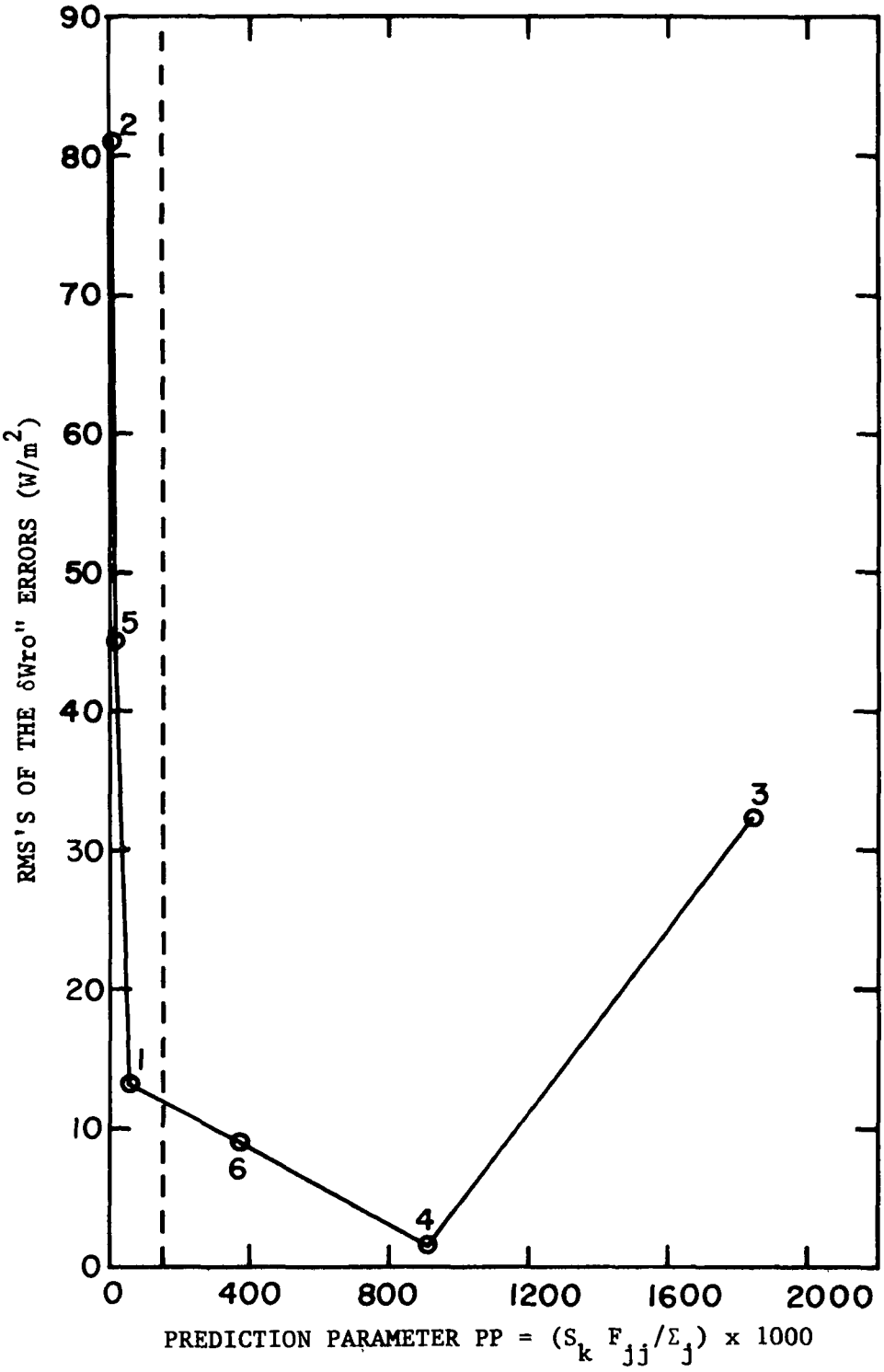

Figure 5-16. Relationship between the Prediction Parameter and the Rms's of the δWro" Errors Obtained with the Stabilized Inverse Matrix of a Spherical Radiometer Which Was Derived for Diffuse Reflection and Then Applied to a Field Described by a Bidirectional Reflectance Function.

A comparison of the results obtained in the above three cases for those regions whose data was predicted acceptable (regions 3, 4 and 6) is presented in Table 5-11. From the results shown in rows 1, 2, 4, 5, 7 and 8 of this table it is seen that whenever the correct angular function that describes the field is used during data interpretation, the results obtained for regions 3, 4 and 6 are satisfactory. Rows 3, 6 and 9 indicate that region 3 is not acceptable when the DIF model is used to interpret data obtained from a radiation field which is represented by a BRM. This result is unreasonable, as indicated above, since region 3 was observed more than any of the other regions, that is, it has the largest value of S_k.

Table 5-11. Comparisons of the effects of proper and improper selection of the angular distribution function on the rms's of the δWro" errors obtained with the stabilized inverse matrix of a spherical radiometer for the three regions whose results are predicted acceptable.

Power uncertainties	Spread	Case studied	Rms's of δWro"		
			R3	R4	R5
Gaussian random	σ=0.5 W	BRM/BRM	2.7	1.4	6.4
Gaussian random	σ=0.5 W	DIF/DIF	1.6	1.6	6.7
Gaussian random	σ=0.5 W	BRM/DIF	33.0	1.4	10.1
Systematic	-.9 to .9 W	BRM/BRM	2.2	1.1	3.6
Systematic	-.9 to .9 W	DIF/DIF	0.9	0.9	5.5
Systematic	-.9 to .9 W	BRM/DIF	32.7	0.5	9.8
Gaussian random	σ=0.5 W	BRM/BRM	1.9	2.0	6.2
plus		DIF/DIF	1.2	1.4	6.1
systematic	0.9 W	BRM/DIF	32.2	1.6	9.3

Best fit technique

This technique is a natural outgrowth of the instantaneous technique. As explained in detail in its application to the LWR case, the main difference between the two methods developed is that in the instantaneous technique, the number of observations J equals the number of regions K, while in the best fit technique the number of observations J is much greater than K the number of regions observed. In the best fit technique, the method of least squares is used to find an approximate solution to the problem.

Since the details of the best fit technique were thoroughly discussed in the LWR case, the application of this technique to the case of SWR will be done by simply using the same illustration introduced in the LWR case. That is, it is assumed that thirty-six observations are made of the same six regions used in that illustration. The values of Wro of the six regions are presumed to remain constant during each set of six measurements, and then they are changed before the next set of six measurements is taken. Table 5-12 displays the thirty-six values of Wro. Each row in this table has the Wro values that the six regions have during a given set of six measurements.

As in the case of LWR, the four types of power measurements itemized below are studied. For each of these four types of measurements, thirty-six observations are simulated for both types of radiometers. The four types of measurements considered are the same ones used in the LWR application and which are restated here for easy reference.

Table 5-12. Values of Wro of the six regions for each of the six sets of observations.

Meas. No.	Values of Wro (W/m^2)					
K	Region 1	Region 2	Region 3	Region 4	Region 5	Region 6
1-6	541.0	446.0	406.0	338.0	271.0	203.0
7-12	531.0	457.0	416.0	323.0	261.0	213.0
13-18	521.0	467.0	426.0	318.0	246.0	223.0
19-24	511.0	477.0	436.0	308.0	241.0	233.0
25-30	526.0	467.0	396.0	323.0	256.0	218.0
31-36	536.0	452.0	386.0	333.0	266.0	208.0
AVERAGES	527.7	461.0	411.0	323.8	256.8	216.3

1. Exact power measurements, i.e., no uncertainties included.
2. Power values include Gaussian random errors with σ=0.5 W.
3. Powers include 0.9 W systematic errors.
4. Combinations of the above Gaussian and systematic uncertainties are included in the power values.

Table 5-13 displays the results obtained with the best fit technique by simulating the types of power measurements described above. The δWro errors shown in this table were calculated by subtracting the results obtained in each case from the average value of Wro computed for each region. These averages are shown in the last row of Table 5-12.

The SWR field is assumed to be described by a BRM and this same BRM is used for interpreting the data.

The magnitudes of all of the δWro errors obtained with the best fit technique are below 12 W/m^2 as seen from the results shown in Table 5-13, and hence, the errors are acceptable.

Table 5-13. δWro errors obtained with the best fit technique for spherical and horizontal plate radiometers. (BRM)

Power uncertainties	Spread	Radiometer	δWro errors (W/m^2)					
			Region 1	Region 2	Region 3	Region 4	Region 5	Region 6
None	--	Sphere	-10.9	9.1	9.1	-7.2	-4.3	2.5
None	--	Plate	-10.1	7.1	8.4	-5.5	-3.1	1.3
Gaussian random	σ=0.5 W	Sphere	-12.5	9.9	9.5	-7.1	-4.7	2.9
Gaussian random	σ=0.5 W	Plate	-11.8	7.8	8.8	-5.3	-3.5	1.9
Systematic	0.9 W	Sphere	-10.0	10.1	10.0	-6.3	-3.4	3.4
Systematic	0.9 W	Plate	-8.8	8.4	9.7	-4.3	-1.9	2.6
Gaussian random plus systematic	σ=0.5 W 0.9 W	Sphere	-11.5	10.8	10.5	-6.2	-3.8	3.9
		Plate	-10.5	9.1	10.1	-4.1	-2.2	3.2

CHAPTER VI. CONCLUSIONS AND RECOMMENDATIONS

Conclusions

On the basis of the results obtained in this investigation, the following is concluded.

1. The techniques developed in this research, denoted as instantaneous and best fit, provide two methods for computing the radiation budget $Q = Hs - Wr - We$ of regions of the earth-atmosphere system which are smaller than the field of view of low spatial resolution radiometers. The two techniques yield the instantaneous and averaged values of the radiant reflectance Wr and the radiant emittance We for each region under study. As previously explained in the Introduction, the regional spatial average of incident solar radiation Hs, the first component of Q, can be easily obtained by available procedures.
2. The instantaneous and best fit techniques have the important characteristic of isolating in space the problem of determining the regional values of We and Wr. No region outside the set of regions under study is used in obtaining the results of the set investigated. Conversely, the data gathered from a given set of regions is not used in computing the results of any that is outside this set. The sizes of the regions in this investigation were arbitrarily chosen. The ratio of the area of the smallest region to the area of the field of view is 0.256, while the ratio of the largest region to the field of view is 0.428. The area of the earth-atmosphere system that is subtended by the field of view of a radiometer at an altitude of about 800 km is 28,606,466 km^2.

An estimate of the smallest region size that is theoretically possible in the use of the instantaneous technique was obtained. For a sampling rate of two observations per minute, the minimum region size is about 5.06×10^6 km^2, which is about 0.177 times the area of the field of view.

3. The scheme introduced for performing the numerical integrations required for computing the powers intercepted by the radiometers represents the simplest way of accomplishing this integration. In this integration scheme, the earth-atmosphere system is divided into 2060 elemental areas. These areas are fixed, that is, their size and position remain unchanged as the satellite moves, regardless of the type of satellite orbit (circular or elliptical).
4. The instantaneous technique isolates in time the determination of We and Wr by evaluating these quantities from radiometer data acquired during a single satellite pass. Consequently, this technique provides the instantaneous regional values of We and Wr.
5. The instantaneous technique yields excellent results when applied to the case of radiant emittance as well as to the case of radiant reflectance when used in conjunction with the matrix stabilization and prediction techniques. The high accuracies obtained are illustrated by the following range of uncertainties in the values of We and Wr when typical observational errors are included in the power measurements of spherical and horizontal plate radiometers: a) 1.1 to 4.4 W/m^2 for the sphere, and 1.4 to 4.9 W/m^2 for the plate in the case of We; b) 1.8 to 5.3 W/m^2 for the sphere and 1.4 to 6.8 W/m^2 for the plate in the case of Wr.

6. The stabilization scheme developed in this research renders well-conditioned the configuration factor matrices F as demonstrated by a) the significant reduction in the values of the condition numbers of the matrices, from 1087 to 184 for the sphere, and from 945 to 253 for the plate in the case of We; from 1192 to 134 for the sphere, and from 987 to 190 for the plate in the case of Wr; b) the remarkable decrease in the magnification of observational errors, from 43.7 to 4.4 W/m^2 for the sphere, and from 35.1 to 5.9 W/m^2 for the plate in the case of a LDF field for region 6.
7. The prediction technique represents a reliable method for determining which results are to be considered acceptable within defined error limits and which are to be taken as unreliable for lack of adequate information. Generally, a region will have unreliable results (errors greater than 15 W/m^2) if the magnitude of the prediction parameter is less than 150 for the sphere and 100 for the plate.
8. Matrix stabilization and prediction techniques are unnecessary when applying the instantaneous technique to cases that include instrumental errors when sufficiently large portions of all of the regions are observed. This was demonstrated by simulating a series of observations from selected satellite positions in such a manner that adequate sections of all regions were observed. The results obtained with the original matrix for the sphere had errors not greater than 3 W/m^2 which are considered acceptable relative to the criterion of 15 W/m^2. It was unnecessary to use the stabilization and prediction techniques in this case which further demonstrates the feasibility of the approach.

9. The errors in the results increase by about 3 W/m^2 (from about 3% to about 5% for the worst acceptable case) when a LWR field which is described by a limb darkening function is assumed to be isotropic. Hence, the isotropic assumption can be used during interpretation of observations of LWR fields without introducing errors beyond reasonable limits.

10. The errors in Wr are affected in an unpredictable fashion when a SWR field which is described by a bidirectional reflectance model is interpreted as a diffuse field in the solution. For example, region no.3 which had an acceptable rms error of 1.9 W/m^2 jumped to 32.2 W/m^2 which is unacceptable. On the other hand, region no.1 which had an unacceptable rms error of 17.9 W/m^2 changed to 13.4 W/m^2 which is acceptable. Therefore, it is not advisable to assume that a reflected radiation field is diffuse unless there is evidence (e.g., data collected with a narrow field of view scanner radiometer) that this is the case.

11. The division of the earth-atmosphere system into regions presupposes that the regions have homogeneous emitting and reflecting characteristics. However, it was found that the instantaneous technique yields acceptable results in many cases where a region is divided into two subregions of almost equal size and having different values of We. It was determined that the values of We in the two subregions can differ by as much as 10 W/m^2 with a resulting rms error below 6 W/m^2. Furthermore, in two cases the difference between the two subregions was as much as 50 W/m^2 and the results obtained were: a) -13.3 and 15.7 W/m^2 for the sphere

and plate, respectively, in one case; b) 18.7 and 20.0 W/m^2 for the sphere and plate, respectively, in the other case. The results in the first case are acceptable (the acceptable limit is 15 W/m^2), while those of the second are not. However, an evaluation parameter was developed which identifies these situations.

12. The best fit technique produces solutions which are acceptable for all regions. The magnitude of the errors in these solutions range from 1.5 to 13.0 W/m^2 for the sphere, and from 0.2 to 12.5 W/m^2 for the plate in the case of emitted LWR. In the reflected SWR case, the errors range from 3.8 to 11.5 W/m^2 for the sphere, and from 2.2 to 10.5 W/m^2 for the plate.

Recommendations

The following two items are recommended.

1. Investigate the effects that satellite altitude uncertainties can have upon the elements of the configuration factor matrices as well as on the results.
2. Apply the techniques developed to data gathered by satellite radiometer systems consisting of wide field of view and scanner narrow field of view radiometers (such as NOAA's ERB experiment). Data from the scanner radiometer can be used to obtain the angular distributions of the radiation fields observed. The resulting angular functions can then be incorporated into the instantaneous and best fit techniques in order to interpret the data collected by the wide field of view radiometer.

LIST OF REFERENCES

LIST OF REFERENCES

Bandeen, W. R.; Hanel, R. A.; Licht, J.; Stampfl, R. A.; Stroud, W. G. "Infrared and Reflected Solar Radiation from TIROS II Meteorological Satellite." NASA TN D-1096, 1961.

Bignell, K. J. "Heat-Balance from an Earth-Satellite - an Analysis of Some Possibilities." Quart. J. Roy. Meteor. Soc., 87, 231-244 (1961).

Campbell, G. G.; Vonder Haar, T. H. "Monthly Average of Global and Zonal Radiation Budget from Integrating Sensors, an Accuracy Assessment from Numerical Simulation." Collection of Abstracts of the Second Conference on Atmospheric Radiation of the American Meteorological Society, 115-118 (1975).

Chang, D. T.; Widger, Jr., W. K. "Study, Simulation, of Oceanographic and Geophysical Space-Sensor Displays." Technical Report NAVTRADEVCEN 66-C-0031-1, Naval Training Device Center, 1968.

Cohen, A. M.: Cutts, J. F.; Fielder, R.; Jones, D. E.; Ribbaus, J.; Stuart, E. Numerical Analysis. New York: John Wiley and Sons, 1973.

Faddeev, D. K.; Faddeeva, V. N. Computational Methods of Linear Algebra. San Francisco: W. H. Freeman and Company, 1963.

Fleming, H. E.; Wark, D. Q. "A Numerical Method for Determining the Relative Spectral Response of the Vidicons in a Nimbus Satellite System." Appl. Opt., 4, 337-342 (1965).

Hanel, R. A.; Wark, D. Q. "Physical Significance of the TIROS II Radiation Experiment." NASA TN D-701, 1961.

Harrison, E. F.; Brooks, D. R.; Gibson, G. G. "Mission Analysis to Define Satellite Orbits for Earth Radiation Budget Measurements." AIAA Paper No. 76-811, AIAA/AAS Astrodynamics Conference, 1976.

Holloway, L. "Correcting for Unavoidable Smoothing of Artificial Satellite Data." Paper presented at the 155th National Meeting of the AMS. (Available as a manuscript of the U. S. Weather Bureau.) Washington, D. C., 1957.

House, F. B. "A Satellite Experiment to Measure Fluctuations in the Earth's Heat Balance." Master's Thesis, Department of Meteorology, University of Wisconsin, 1961.

House, F. B. "The Radiation Balance of the Earth from a Satellite." Ph.D. Thesis, Department of Meteorology, University of Wisconsin, 1965.

House, F. B. "The Reduction, Analysis, and Interpretation of Radiation Balance Measurements from ESSA Weather Satellites." Final Report, Contract No. E-119-68(N), prepared by GCA Corporation for ESSA/NESC, 1970.

House, F. B. "Deconvolution of Wide-Field Radiative Measurements from Satellites." Preprints of the Conference on Atmospheric Radiation of the American Meteorological Society, 1972.

House, F. B.; Sweet, G. E.; Babcock, R. A.; Mahan, J. R.; Woerner, C. V.; Vonder Haar, T. H. "Long-Term Zonal Earth Energy Budget Experiment." A proposal to AAFE, NASA-Langley, 1973.

Hubert, L. F.; Lehr, P. E. Weather Satellites. 1st edition. Waltham, Massachusetts: Ginn-Blaisdell, 1967.

Jacobowitz, H.; Ruff, I.; Smith, W. L.; Chen, T. S. "The Angular Distribution of Terrestrial Radiation Measured During the Earth Radiation Budget (ERB) Experiment." Collection of Abstracts of the Second Conference on Atmospheric Radiation of the American Meteorological Society, 104 (1975).

Kondratyev, K. Ya. Radiation in the Atmosphere. New York: Academic Press, 1969.

Larsen, S. H. H.; Fugita, T.; Fletcher, W. L. "Evaluation of Limb Darkening from TIROS III Radiation Data." Research Paper No. 18, Mesometeorology Project, Dept. of the Geophysical Sciences, University of Chicago, 1963.

List, R. J. Smithsonian Meteorological Tables. 6th revised edition. Washington, D. C.: Smithsonian Institution, 1966.

Littan, H. H. "A Theoretical Model of Temperature Variations at the Surface of an Orbiting Satellite." J. Geophys. Res., 66, 3693-3698 (1961).

Liventsov, A. V.; Markov, M. N.; Merson, Ya. I.; Shamilev, M. R. "Investigation of the Angular Distribution of Terrestrial Thermal Radiation to Outer Space in the August 27, 1958 Flight of a Geophysical Rocket." Cosmic Research, 4, 523-526 (1966).

Panofsky, H. A.; Brier, G. W. Some Applications of Statistics to Meteorology. University Park, Pa.: The Pennsylvania State University, 1968.

Phillips, D. L. "A Technique for the Numerical Solution of Certain Integral Equations of the First Kind." J. Assoc. Comp. Mach., 9, 84-97 (1962).

Pina, J. F.; House, F. B. "Techniques for Computing the Radiant Emittance from Observations by Wide-Angle Satellite Radiometers." NASA Contractor Report No. CR-145011, 1975a.

Pina, J. F.; House, F. B. "An Inversion Method for Computing Radiances and Albedos of Earth-Atmosphere Regions from Wide-Angle Satellite Sensor Measurements." Collection of Abstracts of the Second Conference on Atmospheric Radiation of the American Meteorological Society, 119-122 (1975b).

Rabbe, A. "Angular Dependence of Albedo from Stratiform Clouds as Measured by TIROS IV Scanning Radiometers." Research Paper No. 58, Satellite and Mesometeorology Research Project, Dept. of the Geophysical Sciences, University of Chicago, 1966.

Raschke, E. "The Radiation Balance of the Earth-Atmosphere from Radiation Measurements of the Nimbus II Meteorological Satellite." NASA TN D-4589, 1968.

Raschke, E.; Vonder Haar, T. H.; Bandeen, W. R.; Pasternak, M. "The Annual Radiation Balance of the Earth-Atmosphere System During 1969-1970 from Nimbus 3 Measurements." NASA TN-7249, 1973.

Ruff, I.; Koffer, R.; Fritz, S.; Winston, J. S.; Rao, P. K. "Angular Distribution of Solar Radiation Reflected from Clouds as Determined from TIROS IV Radiometer Measurements." ESSA Technical Report NESC-38, 1967.

Ruttenberg, S. (Ed.) IGY World Data Center A,IGY General Report Series No. 5, 6-7 (1959).

Smith, G. L.; Green, R. N. "A Technique for Analysis of Low Resolution Measurements of Earth Radiation Budget." Collection of Abstracts of the Second Conference on Atmospheric Radiation of the American Meteorological Society, 111-114 (1975).

Smith, G. L.; Green, R. N. "Theoretical Analysis of Wide Field of View Radiometer Measurements of Earth Energy Budget." Fifth Annual Remote Sensing of Earth Resources Conference, 1976a.

Smith, G. L.; Green, R. N. "The Analysis of Wide Field of View Radiometer Measurements of Earth Radiation Budget." Nineteenth Plenary Meeting of COSPAR Symposium on Meteorological Observations from Space, 1976b.

Smith, G. L.; Green, R. N.; Campbell, G. G. "A Statistical Interpretation Technique for Wide Angle Radiometer Measurements of Earth Energy Budget." Fourth Conference on Probability and Statistics, American Meteorological Society, 1975.

Spiegel, M. R. Theory and Problems of Statistics. New York: Schaum's Outline Series, McGraw-Hill Book Company, 1961.

Stevenson, J. A.; Grafton, J. C. "Radiation Heat Transfer Analysis for Space Vehicles." ASD Technical Report 61-119, Part I. Aeronautical Systems Division, Air Force Systems Command, U. S. Air Force, Wright Patterson Air Force Base (Ohio), 297-426 (1961).

Suomi, V. E. "The Radiation Balance of the Earth from a Satellite." Annals of the IGY, 6, 331-340 (1958).

Suomi, V. E. "The Thermal Radiation Balance Experiment on Board Explorer VII." NASA TN D-608, 11, 273-305 (1961).

Suomi, V. E.; Hanson, K. J.; Vonder Haar, T. H. "The Theoretical Basis for Low-Resolution Radiometer Measurements from a Satellite." Annual Report, Grant WBG-27, Department of Meteorology, University of Wisconsin, 79-100 (1967).

Twomey, S. "On the Numerical Solution of Fredholm Integral Equations of the First Kind by the Inversion of the Linear System Produced by Quadrature." J. Assoc. Comp. Mach., 10, 97-101 (1963).

Twomey, S. "The Application of Numerical Filtering to the Solution of Integral Equations Encountered in Indirect Sensing Measurements." J. of the Franklin Institute, 279, 95-109 (1965).

Twomey, S. "Indirect Measurements of Atmospheric Temperature Profiles from Satellites: Mathematical Aspects of the Inversion Problem." Monthly Weather Review, 94, 363-366 (1966).

Van Allen, J. A. "Scientific Instrumentations of Satellites." Geophysics and the IGY, edited by H. Odishaw and S. Ruttenberg, American Geophysical Union, Pub. No. 590, (Geophysical Monograph Number 2), 1958.

Vonder Haar, T. H. "Variations of the Earth's Radiation Budget." Ph.D. Thesis, Department of Meteorology, University of Wisconsin, 1968.

Wark, D. Q.; Fleming, H. E. "Indirect Measurements of Atmospheric Temperature Profiles from Satellites: Introduction." Monthly Weather Review, 94, 351-362 (1966).

APPENDICES

APPENDIX A

DIVISION OF THE SURFACE AREA OF THE E-A SYSTEM INTO ELEMENTAL AREAS

APPENDIX A

DIVISION OF THE SURFACE AREA OF THE E-A SYSTEM INTO ELEMENTAL AREAS

The power intercepted by a horizontal flat plate radiometer during the jth observation of a set of K regions is given by

$$P_j = \sum_{k=1}^{K} \int_{\psi'_k} d\psi' \int_{\alpha_k} N'(\alpha,\psi',t)\sin\alpha\cos\alpha\, d\alpha \qquad \text{(A-1)}$$

where α and ψ' are the nadir and azimuthal angles of the elemental area observed from the satellite, and N' is the radiance when expressed in terms of α and ψ'. The angles ψ'_k and α_k under the integration signs indicate that the integrations over each region k must be performed between the corresponding lower and upper limits of these angles. If one of the regions of the set K under study is not included within the FOV of the jth observation, this region will not appear in the sum indicated in Eq.(A-1).

The following three schemes for performing numerically the double integration in Eq.(A-1) were evaluated. Scheme #3 was found to represent the simplest procedure for performing this numerical integration.

1. The FOV is divided into a finite number of <u>equal</u> elemental solid angles $\Delta\Omega$. Each $\Delta\Omega$ subtends an elemental area ΔA at the surface of the E-A system. As the nadir angle of $\Delta\Omega$ increases, the elemental area ΔA subtended by the elemental solid angle also increases. All $\Delta\Omega$'s that have <u>equal nadir angle</u> subtend equal elemental areas ΔA.

The origin of this grid of ΔA's, or reference system, is assumed to be centered at the nadir point of the satellite. Hence, it is supposed to move with the nadir point. One of the main difficulties with this scheme is that one ΔA can include large portions of two adjacent regions (especially at the limb where the ΔA's are largest) and there is no simple procedure for evaluating what fraction of the ΔA is occupied by each region.

2. The surface area of the E-A system that is subtended by the FOV of the radiometer is divided into a finite number N of equal elemental areas ΔA. As in the previous scheme, the origin of this grid of ΔA's, or reference system, is centered at the nadir point of the satellite and hence, travels with it. This scheme is difficult to handle if it is applied to elliptical orbits, especially orbits with high eccentricities. In these cases the area A subtended by the FOV constantly changes and hence, the size of the ΔA's also changes if N is held constant. An alternative approach is to keep the size of the ΔA's approximately the same by varying N to compensate for the variations in A. Either of these two approaches requires extra computations which are unnecessary when using scheme #3 shown below which was the scheme finally selected.

3. The entire surface of the E-A system is divided into 2060 elemental areas as will be shown in detail below. These elemental areas are fixed on the surface of the E-A system

and are numbered consecutively starting at the north pole and ending at the south pole. The positions of the ΔA's are given by the longitudes and latitudes of their centroids. The regions into which the E-A system is divided are defined in terms of these elemental areas in such a way that each ΔA belongs to one, and only one, region.

This is the first time that this scheme has ever been introduced to perform numerically the double integration that appears in Eq.(A-1). It is believed that this scheme represents the simplest way of accomplishing this integration.

The power increments ΔP contributed by the ΔA's in the kth region are summed up to obtain the value of the double integral for the kth region in Eq.(A-1). The values of ΔP are easily computed once the altitude of the satellite and the longitudes and latitudes of the subsatellite point and ΔA are known.

The procedure followed in scheme #3 to perform the division of the surface of the E-A system into 2060 elemental areas is itemized as follows:

1. The radius of a spherical earth having the same surface area as the actual earth is approximately 6371.23 km (List, 1966). The thickness of an atmospheric spherical shell of about 30.32 km was included as part of the spherical E-A system considered. More than 99% of the total atmosphere is contained within this shell (House, 1965). Then, the radius R of the spherical E-A system is 6401.55 km which yields a surface area A of 514,967,887 km^2.

2. The surface area of each hemisphere of the E-A system is divided into 1029 ΔA's distributed among 20 latitudinal bands and a polar elemental area ΔA_p. One hemisphere is the mirror image of the other. The areas of each of the 1029 ΔA's is 250,000 km^2, and that of the ΔA_p is 233,900 km^2 which yields an area for the hemisphere of 257,483,900 km^2. Thus, the total surface of the spherical E-A system is 514,967,800 km^2 according to this division.

3. Each latitudinal band contains an integral number of identical elemental areas ΔA. Although the areas of all ΔA's are equal, their shape varies from one band to the next. The northern and southern latitudinal boundaries of the jth band are given, respectively, by the latitudes ϕ_j and ϕ_{j+1}.

4. The common longitudinal width ΔLON_j^d (in degrees) of the ΔA's in the jth band is obtained by dividing the 360 degrees in the circumference by n_j, the number of ΔA's in the jth band. The value of ΔLON_j^k (in km) is determined by dividing the value of the latitudinal circumference C_j^o (in km) by n_j. C_j^o is computed for the central latitude ϕ_j^c of the jth band which is given by $\phi_j^c = (\phi_j + \phi_{j+1})/2$. The value of C_j^o (in km) is then given by $C_j^o = 2\pi R \cos \phi_j^c$, and the ΔLON_j^k (in km) is given by $\Delta LON_j^k = C_j^o/n_j$. The first ΔA of each band is assumed to be west of the Greenwich meridian, that is, this meridian is the eastern longitudinal boundary of the first ΔA in each band. This meridian is also the western longitudinal boundary of the last ΔA in each band.

5. The longtitudes of the centroids of the ΔA's in the jth band are $(\Delta LON_j^d)/2$ for the first ΔA, $3(\Delta LON_j^d)/2$ for the second, and so on; $(n_j-1/2)(\Delta LON_j^d)$ is that of the last ΔA in the jth band.

6. The latitudinal width of the jth band ΔLAT_j^d (in degrees) is given by $\Delta LAT_j^d = \phi_j - \phi_{j+1}$, where ϕ_j and ϕ_{j+1} are the higher and lower latitudinal boundaries, respectively, of the jth band. The common latitudinal width ΔLAT_j^k (in km) of all the ΔA's in the jth band is given by the product $\Delta LAT_j^k = \Delta LAT_j^d$ x 111.728 (km/deg).

7. The common latitude of the centroids of all the ΔA's in the jth band is given by $\phi_j^c = (\phi_j + \phi_{j+1})/2$.

8. The 2060 elemental areas are identified by a sequential numbering system which begins with #1 for the ΔA_p of the north pole and ends with #2060 for the ΔA_p of the south pole. The #2 elemental area is the first ΔA in the j=1 band. The first ΔA in each band is adjacent to, and to the west of the Greenwich meridian. The ΔA's in each band are numbered consecutively westward.

Table A-1 lists the 1030 elemental areas of the northern hemisphere: the polar cap ΔA_p of the north pole and the 1029 ΔA's distributed among the 20 latitudinal bands. The data for ΔA_p appears in the first row of the table, its longitudinal width ΔLON and latitudinal width ΔLAT in km are not shown since these quantities have no meaning for the polar cap. n_j is the number of ΔA's in the jth band, and N_j is the total number of elemental areas in all bands 0 through j.

Table A-1. Division of the northern hemisphere of the E-A system's surface into 1030 elemental areas.

jth band	n_j	N_j	Identification number range	ϕ_j deg	ϕ_{j+1} deg	Δ LON km	Δ LAT km	CENTROID(j,1) Lon (deg)	CENTROID(j,1) Lat (deg)
0	1	1	1	90.00	87.56	--	(Radius) 272.62	--	90.00
1	4	5	2 - 5	87.56	84.39	706.2	354.1	45.00	85.97
2	11	16	6 - 16	84.39	79.91	499.5	500.6	16.36	82.15
3	16	32	17 - 32	79.91	75.69	531.2	470.7	11.25	77.80
4	23	55	33 - 55	75.69	71.20	498.2	501.9	7.83	73.45
5	28	83	56 - 83	71.20	66.85	514.2	489.3	6.43	69.03
6	34	117	84 - 117	66.85	62.43	506.7	493.5	5.29	64.64
7	40	157	118 - 157	62.43	57.95	499.8	500.3	4.50	60.19
8	45	202	158 - 202	57.95	53.51	503.3	496.9	4.00	55.73
9	50	252	203 - 252	53.51	49.06	503.2	497.0	3.60	51.28
10	55	307	253 - 307	49.06	44.59	500.4	499.7	3.27	46.82
11	59	366	308 - 366	44.59	40.14	503.7	496.4	3.05	42.36
12	63	429	367 - 429	40.14	35.70	503.6	496.5	2.86	37.92
13	67	496	430 - 496	35.70	31.23	500.8	499.3	2.69	33.46
14	70	566	497 - 566	31.23	26.78	502.5	497.6	2.57	29.00
15	73	639	567 - 639	26.78	22.31	501.2	498.9	2.47	24.54
16	75	714	640 - 714	22.31	17.87	503.7	496.5	2.40	20.09
17	77	791	715 - 791	17.87	13.42	503.0	497.1	2.34	15.64
18	79	870	792 - 870	13.42	8.94	499.5	500.6	2.28	11.18
19	80	950	871 - 950	8.94	4.45	499.3	500.8	2.25	6.70
20	80	1030	951 - 1030	4.45	0.00	502.4	497.7	2.25	2.23

The j = 0 band is defined as the band containing the north polar cap. The assignment of the identification numbers of the elemental areas was described previously. ΔA_p is no.1, and the ΔA's are numbered westward within each band. The lowest number in each band is assigned to the ΔA west of the Greenwich meridian, and the highest number in the band is that of the ΔA east of this meridian. ϕ_j and ϕ_{j+1} are the upper and lower latitudinal boundaries of the jth band. CENTROID (j,1) refers to the centroid of the first ΔA in the jth band. The longitude and latitude in degrees of CENTROID(j,1), for all j values, are given in the last two columns of the table.

The numbering system shown in Table A-1 continues south of the equator in the same fashion. For example, ΔA#951 which is the first elemental area of the j = 20 band (the last band in the northern hemisphere) has as its mirror image the elemental area ΔA#1031 which is the first ΔA in the j = 21 band (the first band in the southern hemisphere). Hence, the longitudes of the boundaries and centroid of ΔA#1031 are the same as those of ΔA#951. The corresponding latitudes of the boundaries and centroids of these two elemental areas have the same magnitude but different sign. Thus, from the latitudes of the upper and lower boundaries and centroid given for ΔA#951 in Table A-1, the corresponding values of these quantities for ΔA#1031 are, 0.00°, -4.45°, and -2.23°, respectively.

Since the area ΔA_p = 233,900 km^2 is somewhat smaller than ΔA = 250,000 km^2, one must decide how the ΔA_p's are to be treated whenever one of them appears within the FOV of the radiometer. Two possible approaches are here considered: (a) assign the correct area to ΔA_p whenever it is observed and no error is introduced, and (b) assume

ΔA_p to have an area equal to ΔA and introduce a small error into the computations.

The fractional error introduced when ΔA_p is assigned the area of ΔA is computed as follows:

$$\frac{\Delta A - \Delta A_p}{A_{FOV}} = \frac{250{,}000 - 233{,}000}{28{,}606{,}466} = 0.00056$$

or about 0.056% of A_{FOV} which is the area of the FOV. This error is insignificant and approach (b) is considered acceptable.

Figure A-1 displays most of the elemental areas into which the earth-atmosphere system was divided for performing the numerical integrations required in the two techniques developed to determine We and Wr.

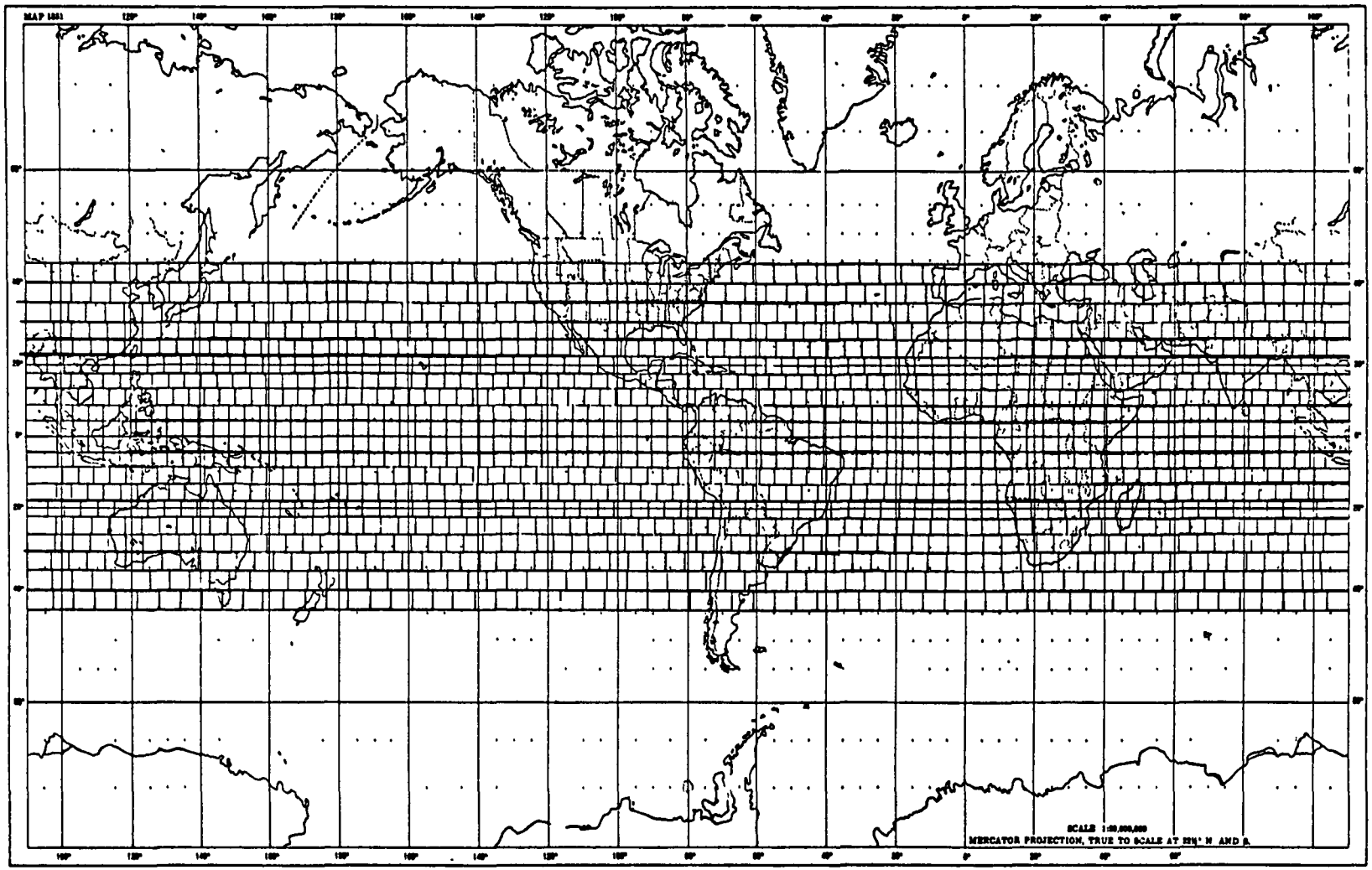

Figure A-1. Division of the Earth-Atmosphere System into Elemental Areas.

APPENDIX B

DERIVATIONS OF THE MAIN EXPRESSIONS USED IN COMPUTATIONS OF THE RADIANT REFLECTANCE

APPENDIX B

DERIVATIONS OF THE MAIN EXPRESSIONS USED IN COMPUTATIONS OF THE RADIANT REFLECTANCE

Equations (B-1), (B-2) and (B-3) below are used by Raschke, et al. (1973). These equations are derived here in complete detail.

$$\zeta = \cos^{-1}[\cos\phi\cos\delta\cos(\lambda_G - \lambda) + \sin\phi\sin\delta] \tag{B-1}$$

$$\psi = \cos^{-1}\left[\frac{\cos\zeta\cos\theta - \cos\Gamma}{\sin\zeta\sin\theta}\right] \tag{B-2}$$

where

$$\cos\Gamma = \frac{1}{D}\{[K\cos\phi_s\cos(\lambda_s-\lambda_G)-\cos\phi\cos(\lambda-\lambda_G)]\cos\delta + [K\sin\phi_s - \sin\phi]\sin\delta\} \tag{B-3}$$

The denominator D is given by

$$D = \{K^2 + 1-2K[\cos\phi_s\cos\phi\cos(\lambda-\lambda_s) + \sin\phi_s\sin\phi]\}^{1/2} \tag{B-4}$$

K is defined by

$$K \equiv \frac{R+H}{R} \tag{B-5}$$

where R is the radius of the E-A system and H is the altitude of the satellite.

Figure B-1 is used to give a pictorial definition of the angles entering into the expressions to be derived. The three planes shown in this figure are helpful in giving a precise definition of the angle ψ. These planes are described as follows.

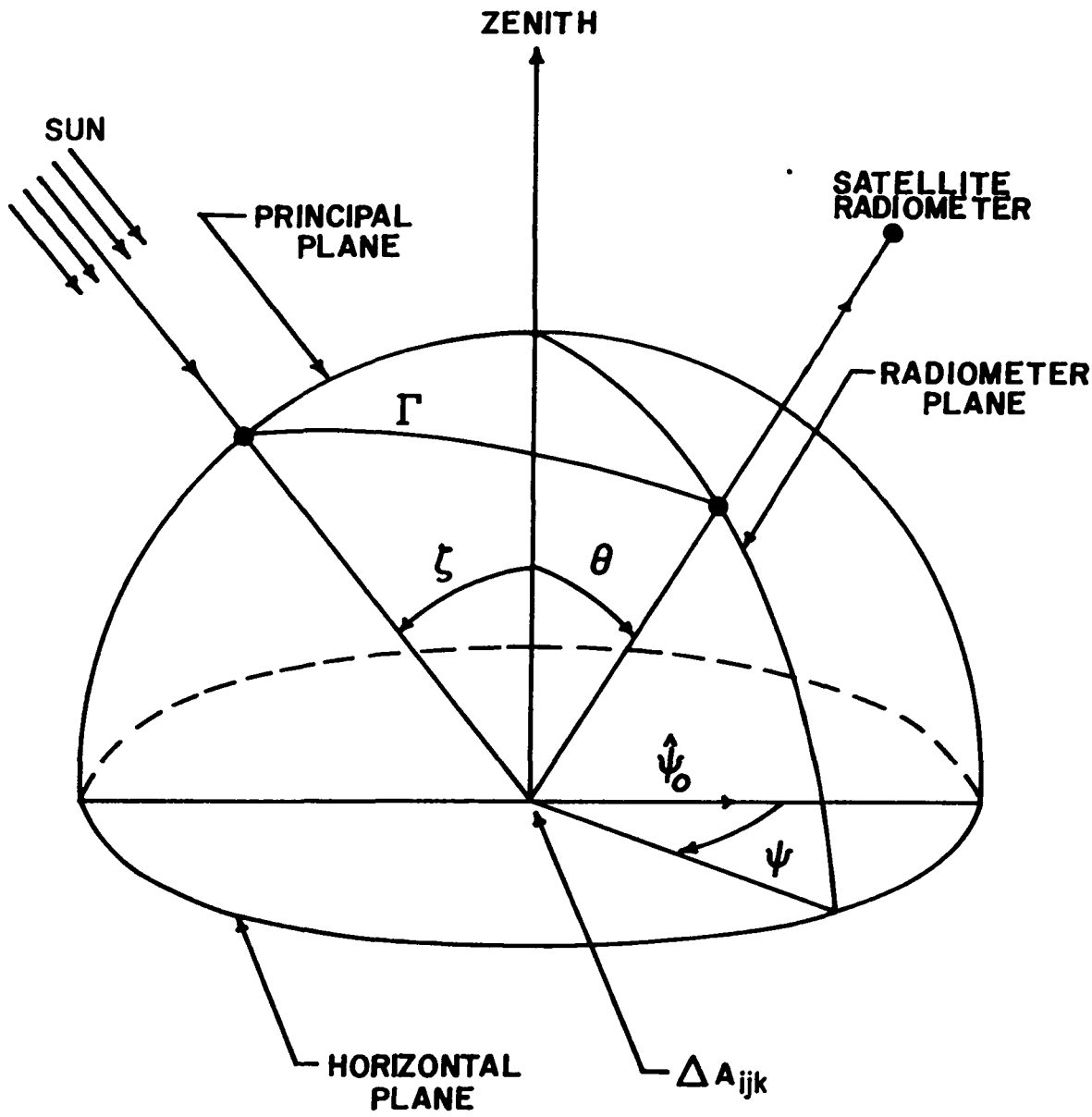

Figure B-1. Pictorial Definition of the Angles Used to Compute the SWR Power Increment ΔP_{ijk} Contributed by the Elemental Area ΔA_{ijk}.

1. Principal plane. The three points used for defining this plane are the center of the sun, the center of the earth, and the centroid of the observed elemental area ΔA_{ijk}. Hence, the zenith-nadir line through this elemental area lies in the principal plane.

2. Horizontal plane. This plane contains the elemental area ΔA_{ijk} and is perpendicular to the zenith-nadir line through the centroid of ΔA_{ijk}.

3. Radiometer plane. The three points used to define this plane are the center of the radiometer, the center of the earth, and the centroid of ΔA_{ijk}.

The unit vector $\hat{\psi}_o$ lies in the intersection of the principal and horizontal planes. Its origin is at the centroid of ΔA_{ijk} and it points in the antisun direction as shown in Figure B-1. The angle ψ is the angle between the radiometer plane and $\hat{\psi}_o$. It is measured on the horizontal plane as shown in Figure B-1. The angle Γ is the angle between the sun and the satellite as measured at ΔA_{ijk}. The angles ζ and θ are the zenith angles of the sun and the satellite as measured at ΔA_{ijk}.

Figure B-2 is formed by making two projections onto the celestial sphere. In one projection, ΔA_{ijk} is considered to be at the center of the celestial sphere and the point SAT' is the projection of the satellite. In the other projection, the celestial sphere is assumed to be geocentric and SAT^c is the projection of the satellite. SUN and ΔA are the projected points of the sun and ΔA_{ijk} in both of

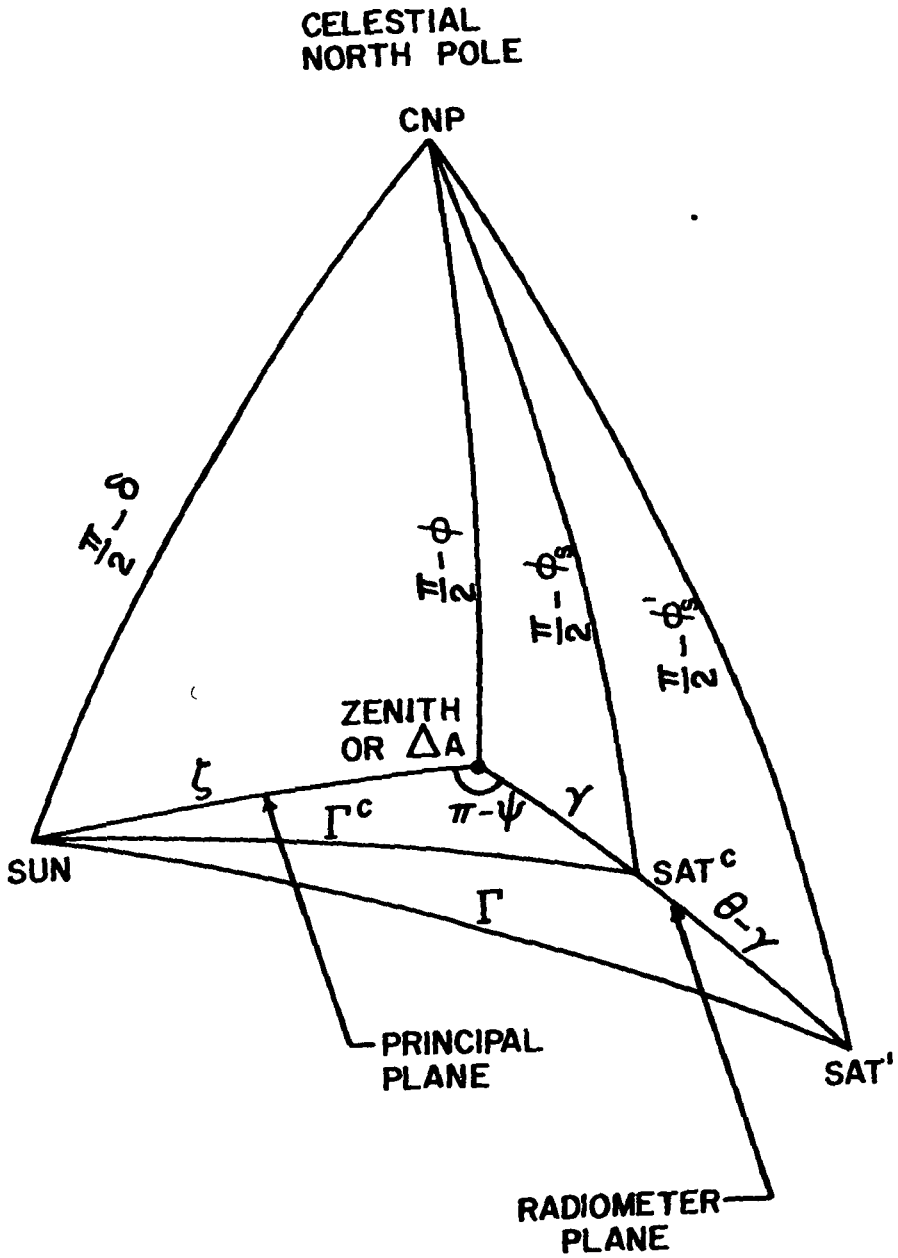

Figure B-2. Projections of the Sun, ΔA, and the Satellite onto a Geocentric Celestial Sphere and onto a Celestial Sphere Centered at ΔA_{ijk}.

the above projections.

From Figure B-1, one can see that the satellite and the two points used as centers of the celestial sphere during the projections (the center of the earth and ΔA_{ijk}) lie in the radiometer plane. Then, the intersection of this plane and the celestial sphere must contain both satellite projections which are denoted by SAT^c and SAT' in Figure B-2. As shown in Figure B-1, θ is the zenith angle of the satellite, that is, the angle between the zenith and the radiometer as seen from ΔA_{ijk}. Hence, it is the angle between ZENITH (or ΔA) and SAT' in Figure B-2. The angle γ, on the other hand, is the angle between the zenith at ΔA_{ijk} and the satellite as seen from the center of the earth. Thus, it is the angle between ZENITH(or ΔA) and SAT^c in Figure B-2. The angle Γ shown in Figure B-1 between the sun and the radiometer as seen from ΔA_{ijk}, is the angle between the SUN and SAT' in Figure B-2. On the other hand, the angle Γ^c between the sun and the radiometer as seen from the center of the earth is the angle between SUN and SAT^c in Figure B-2.

The terrestrial longitudes are considered as the celestial longitudes in Figure B-2, and the terrestrial latitudes and the sun's declination as the celestial latitudes for purposes of this derivation. The latitude of SAT^c is ϕ_s and that of SAT' is defined as ϕ_s'. CNP is the celestial north pole.

It should be noted that only the satellite is projected onto two different points when the center of the celestial sphere is shifted from ΔA_{ijk} to the earth's center. This is due to the finite height of the satellite. The sun, however, is assumed to be infinitely distant from the earth and hence both of its projections coincide.

Derivation of Eq.(B-1) is as follows. Consider the spherical triangle defined by the three points SUN, ΔA, and CNP in Figure B-2. Apply to this triangle the law of cosines for spherical triangles and obtain

$$\cos \zeta = \cos(\tfrac{\pi}{2} - \delta)\cos(\tfrac{\pi}{2} - \phi)+\sin(\tfrac{\pi}{2} - \delta)\sin(\tfrac{\pi}{2} - \phi)\cos(\lambda_G - \lambda)$$

or

$$\cos \zeta = \cos \phi \cos \delta \cos (\lambda_G - \lambda) + \sin \phi \sin \delta$$

or

$$\zeta = \cos^{-1}[\cos \phi \cos \delta \cos(\lambda_G - \lambda) + \sin \phi \sin \delta] \qquad \text{(B-7)}$$

which is Eq.(B-1) that was to be derived.

In order to derive Eq.(B-2), consider the spherical triangle defined by the three points SUN, ΔA, and SAT' in Figure B-2. Again, by applying the law of cosines for spherical triangles to this triangle one obtains

$$\cos \Gamma = \cos \zeta \cos \theta + \sin \zeta \sin \theta \cos (\pi - \psi)$$

but since $\cos(\pi-\psi) = - \cos \psi$, the above equation can be written as

$$\cos \Gamma = \cos \zeta \cos \theta - \sin \zeta \sin \theta \cos \psi \qquad \text{(B-8)}$$

or

$$\psi = \cos^{-1} \left[\frac{\cos \zeta \cos \theta - \cos \Gamma}{\sin \zeta \sin \theta} \right] \qquad \text{(B-9)}$$

which is Eq.(B-2) that was to be shown.

Derivation of Eq.(B-3) is as follows. Apply the cosine law to the spherical triangle defined by SUN, ΔA, and SAT^c in Figure B-2

and obtain

$$\cos \Gamma^c = \cos \zeta \cos \gamma + \sin \zeta \sin \gamma \cos(\pi-\psi)$$

or

$$\cos \Gamma^c = \cos \zeta \cos \gamma - \sin \zeta \sin \gamma \cos \psi \tag{B-10}$$

From Eqs.(B-8) and (B-10), respectively, one obtains

$$\sin \zeta \cos \psi = \frac{\cos \zeta \cos \theta - \cos \Gamma}{\sin \theta} \tag{B-11}$$

$$\sin \zeta \cos \psi = \frac{\cos \zeta \cos \gamma - \cos \Gamma^c}{\sin \gamma} \tag{B-12}$$

Equating these two expressions, the result is

$$\sin \theta \cos \zeta \cos \gamma - \sin \theta \cos \Gamma^c = \sin \gamma \cos \zeta \cos \theta - \sin \gamma \cos \Gamma$$

or

$$\cos \Gamma = \frac{1}{\sin\gamma} [\, \sin \theta \cos \Gamma^c - \cos \zeta(\sin \theta \cos \gamma - \cos \theta \sin \gamma)]$$

or

$$\cos \Gamma = \frac{1}{\sin\gamma} [\, \sin \theta \cos \Gamma^c - \cos \zeta \sin(\theta-\gamma)] \tag{B-13}$$

From Figure B-3, the following relationships are obtained

$$\theta = \alpha + \gamma \tag{B-14}$$

$$R \sin \theta = (R + H) \sin \alpha \tag{B-15}$$

$$R \sin \gamma = r \sin \alpha \tag{B-16}$$

$$r^2 = R^2 + (R+H)^2 - 2R(R+H) \cos \gamma \tag{B-17}$$

Eliminating $\sin\alpha$ between Eqs.(B-15) and (B-16) results in

$$r \sin \theta = (R+H) \sin \gamma \tag{B-18}$$

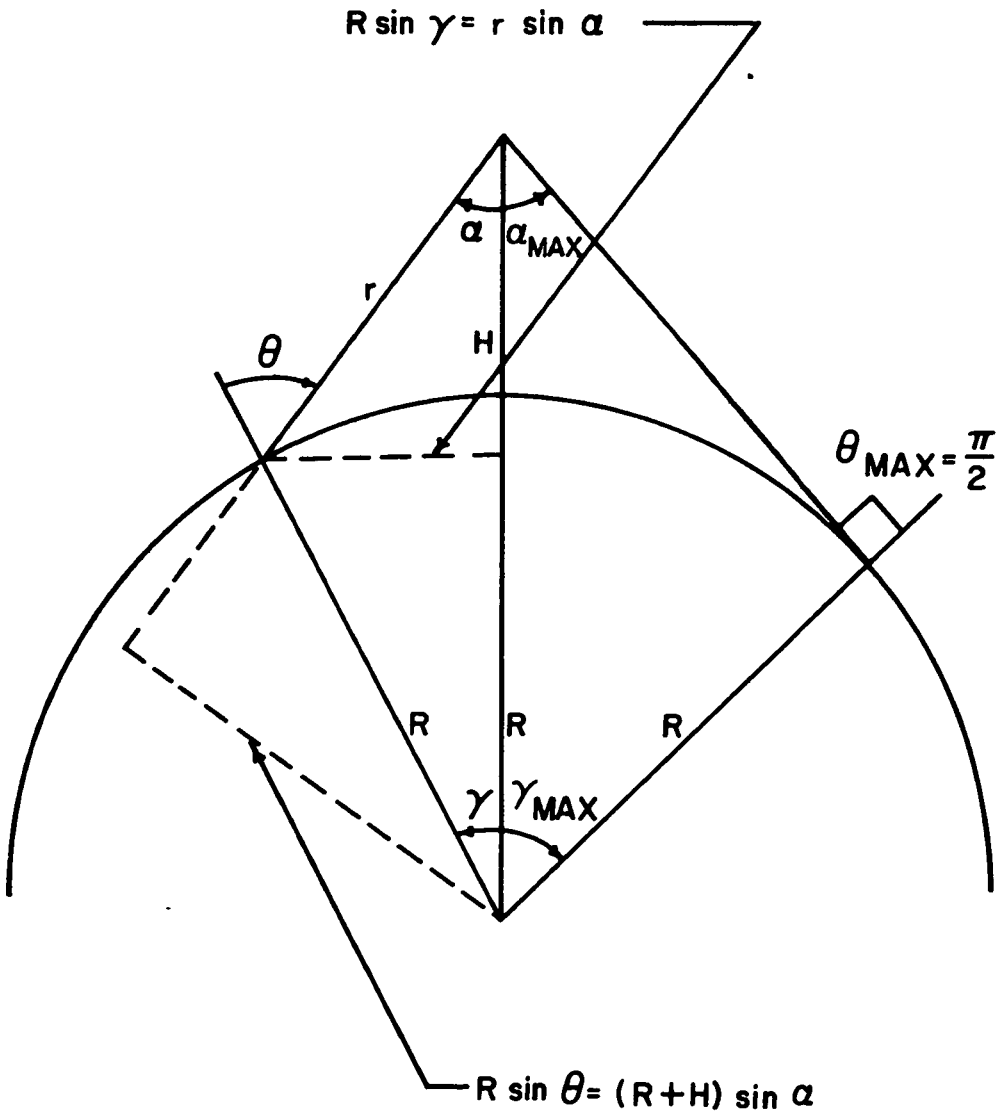

Figure B-3. Pictorial Definition of Some of the Geometrical Parameters Used in Measuring We and Wr by a WFOV Satellite Radiometer.

From Eq.(B-14)

$$\sin(\theta-\gamma) = \sin \alpha \tag{B-19}$$

Substituting Eq.(B-19) into Eq.(B-13), one has

$$\cos \Gamma = \frac{1}{\sin\gamma} [\sin \theta \cos \Gamma^c - \cos \zeta \sin \alpha] \tag{B-20}$$

Applying the cosine law to the spherical triangle defined by SUN, SAT^c, and CNP in Figure B-2 one obtains

$$\cos \Gamma^c = \sin \delta \sin \phi_s + \cos \delta \cos \phi_s \cos(\lambda_G - \lambda_s) \tag{B-21}$$

Similarly, the triangle SUN, Δ A, CNP in the same figure yields

$$\cos \zeta = \sin \delta \sin \phi + \cos \delta \cos \phi \cos (\lambda_G - \lambda) \tag{B-22}$$

Substituting the values of $\cos \Gamma^c$ and $\cos \zeta$ given by Eqs.(B-21) and (B-22) into Eq.(B-20), one obtains

$$\cos \Gamma = \frac{\sin\theta}{\sin\gamma} \sin \phi_s \sin \delta + \frac{\sin\theta}{\sin\gamma} \cos \phi_s \cos (\lambda_G-\lambda_s) \cos\delta -$$

$$\frac{\sin\alpha}{\sin\gamma} \sin \phi \sin \delta - \frac{\sin\alpha}{\sin\gamma} \cos \phi \cos (\lambda_G-\lambda) \cos \delta \tag{B-23}$$

But from Eqs.(B-16) and (B-18), respectively, one obtains

$$\frac{\sin\alpha}{\sin\gamma} = \frac{R}{r} \tag{B-24}$$

$$\frac{\sin\theta}{\sin\gamma} = \frac{R+H}{r} \tag{B-25}$$

Substituting these results into Eq.(B-23) and rearranging,

$$\cos \Gamma = \left[\frac{R+H}{r} \sin \phi_s - \frac{R}{r} \sin \phi\right] \sin \delta +$$

$$\left[\frac{R+H}{r} \cos \phi_s \cos(\lambda_G-\lambda_s) - \frac{R}{r}\cos \phi \cos(\lambda_G-\lambda)\right]\cos \delta \quad \text{(B-26)}$$

Multiplying top and bottom by R and using the definition of K given by Eq.(B-5) results in

$$\cos \Gamma = \frac{R}{r}\{[K \sin \phi_s - \sin \phi] \sin \delta +$$

$$[K \cos \phi_s \cos(\lambda_G-\lambda_s)-\cos \phi \cos(\lambda_G-\lambda)] \cos \delta\} \quad \text{(B-27)}$$

Using Eq.(B-17) for r, one obtains for r/R

$$\frac{r}{R} = [K^2 + 1 - 2 K \cos \gamma]^{1/2} \quad \text{(B-28)}$$

From the spherical triangle Δ A, SAT^c, CNP, in Figure B-2, one obtains

$$\cos \gamma = \sin \phi_s \sin \phi + \cos \phi_s \cos \phi \cos(\lambda-\lambda_s)$$

Substituting this value for cos γ into Eq.(B-28) one obtains the expression for D given by Eq.(B-4), namely

$$D= \frac{r}{R} = \{K^2+1-2 K[\cos \phi_s \cos \phi \cos (\lambda-\lambda_s)+\sin \phi_s \sin \phi]\}^{1/2} \quad \text{(B-29)}$$

Then, using this value of r/R and the fact that cos $(\lambda_G-\lambda_s)$ = cos$(\lambda_s-\lambda_G)$ and cos$(\lambda_G-\lambda)$ = cos$(\lambda-\lambda_G)$,one obtains from Eq.(B-27) the final expression for cos Γ, that is

$$\cos \Gamma = \frac{1}{D} \{[K \cos \phi_s \cos(\lambda_s-\lambda_G)-\cos \phi \cos(\lambda-\lambda_G)]\cos \delta +$$

$$[K \sin \phi_s - \sin \phi] \sin \delta\} \quad \text{(B-30)}$$

which is the same as Eq.(B-3) that was to be derived.

APPENDIX C

ABBREVIATIONS, ACRONYMS, AND SYMBOLS

APPENDIX C

ABBREVIATIONS, ACRONYMS, AND SYMBOLS

A	Albedo defined as Wr/Hs.
ΔA	Elemental area of the earth-atmosphere system equal to 250,000 km^2.
ΔA_{ijk}	The ith elemental area of the kth region within the field of view of the jth observation.
ΔA_p	Polar cap elemental area of the earth-atmosphere system equal to 233,900 km^2.
APT	Automatic picture transmission .
AVCS	Advanced vidicon camera system.
α	Nadir angle of ΔA as seen from the satellite.
α_{max}	Maximum value that α can attain.
BRM	Bidirectional reflectance model. It depends on the directions of the sun and the satellite as seen from ΔA.
BRM/BRM	Bidirectional reflectance model SWR field interpreted as such.
BRM/DIF	Bidirectional reflectance model SWR field interpreted as a diffuse reflection field.
C_j^o	Latitudinal circumference measured at the central latitude ϕ_j^c of the jth band, (km).
DIF	Diffuse reflection model.

DIF/DIF	Diffuse reflection SWR field interpreted as such.
E-A	Earth-atmosphere.
EP	Evaluation parameter defined by $EP=[\sum_{\ell=1}^{L} \varepsilon_\ell^2]^{\frac{1}{2}}$
ε_k	Defined by $\overline{We_k} - We_k''$.
F	Configuration factor matrix.
F_{ijk}	Shape factor of ΔA_{ijk}.
F_{jj}	Diagonal element of the jth row (jth measurement) of the configuration factor matrix.
F_{jk}	Element of matrix F. It is the shape factor of the kth region and jth observation.
F_{wc}	Well-conditioned matrix F.
F^T	Transpose of matrix F.
F^{-1}	Inverse of matrix F.
F_{wc}^{-1}	Inverse of well-conditioned matrix F_{wc}.
$\overline{F_\ell F_n}$	Defined by $\sum_{j=1}^{J} F_{j\ell} F_{jn}$.
FOV	Field of view.
H	Irradiance (W/m^2).
H_o	Solar irradiance of an area normal to the sun's rays; hence, it is given by Hs(0). (W/m^2).
$Hs(\zeta)$	Solar irradiance given by $H_o \cos \zeta$. (W/m^2).
HRIR	High resolution infrared radiometer.
IGY	International Geophysical Year.
ISO	Isotropic.
ISO/ISO	Isotropic LWR field interpreted as such.

j	The jth row of the configuration factor matrix which corresponds to the jth satellite radiometer observation.
J	Total number of satellite radiometer observations.
k	The kth column of the configuration factor matrix, which corresponds to the kth region of the set of K regions under investigation.
K	Total number of regions under study.
LDF	Limb darkening function.
LDF/ISO	Limb darkening function field interpreted as isotropic.
LDF-ISO/ISO	Partially limb darkening function and partially isotropic field interpreted as isotropic.
LDF/LDF	Limb darkening function field interpreted as such.
LSR	Low spatial resolution.
LWR	Longwave radiation (5 to 100μ).
ΔLAT_j^d	The latitudinal width in degrees of the jth band.
ΔLAT_j^k	The latitudinal width in kilometers of the jth band.
ΔLON_j^d	The common longitudinal width in degrees of the ΔA's in the jth latitudinal band.
ΔLON_j^k	The common longitudinal width in kilometers of the ΔA's in the jth latitudinal band.
m	Meter.
MFOV	Medium field of view.
MRIR	Medium resolution infrared radiometer.
N	Radiance; used for LWR and expressed in terms of the zenith angle θ and the azimuthal angle ψ of the satellite as seen from ΔA. ($W/(m^2 - sr)$).

N'	Radiance; used for LWR and expressed in terms of the nadir angle α and the azimuthal angle ψ' of ΔA as seen from the satellite. $(W/(m^2 - sr))$.
N^{iso}	Radiance for isotropic LWR fields. $(W/(m^2 - sr))$.
N^z	Radiance in the zenith direction; used for LWR. $(W/(m^2 - sr))$.
Nr	Radiance; used for reflected SWR and expressed in terms of the zenith angle θ and azimuthal angle ψ of the satellite as seen from ΔA. $(W/(m^2 - sr))$.
NFOV	Narrow field of view.
P	Longwave (or shortwave) radiation (exact) power measured by a satellite radiometer of unit area (W).
P'	Perturbed power recorded by a satellite radiometer of unit area; it is equal to the exact power P plus the instrumental uncertainty δP.
δP	Instrumental error included in the power measurement P'.
ΔP_{ijk}	Power increment contributed by ΔA_{ijk}.
P_{jk}	Power contributed by the kth region to the jth observation.
$\overline{PF_\ell}$	Defined by $\sum_{j=1}^{J} P_j F_{j\ell}$.
PP	Prediction parameter defined by $(S_\kappa F_{jj}/\Sigma_j) \times 1000$.
ϕ_j	Northern latitudinal boundary of the jth band.
ϕ_{j+1}	Southern latitudinal boundary of the jth band.
ϕ_j^c	Central latitude of the jth latitudinal band.

ψ	Azimuthal angle of the satellite as seen from ΔA.
ψ'	Azimuthal angle of ΔA as seen from the satellite.
Q	Net radiation or radiation balance defined by Hs - Wr - We, (W/m^2).
r	Distance from ΔA to the satellite.
$r(\zeta)$	Directional reflectance given by $Wr(\zeta)/Hs(\zeta)$.
$R_1(\zeta)$	Defined by $r(\zeta)/r(0)$.
$R_2(\theta,\psi,\zeta)$	Defined by $r(\zeta)/\pi\rho(\theta,\psi,\zeta)$.
$\rho(\theta,\psi,\zeta)$	Defined by $Nr(\theta,\psi,\zeta)/Hs(\zeta)$.
RFOV	Restricted field of view.
S_k	Sum of the elements in the kth column of the configuration factor matrix. It is the sum of the shape factors contributed by the kth region to the total number of observations made.
SIRS	Satellite infrared spectrometer.
SSP	Subsatellite point.
SWR	Shortwave radiation (0.2 to 5μ).
Σ_j	Sum of the matrix elements in the jth row of the configuration factor matrix. It is the shape factor of the total area within the field of view of the jth observation.
TIROS	Television and infrared observation satellite.
W	Watts (joules/sec).
We	Radiant emittance value assigned to a region, (W/m^2).
We'	Radiant emittance value obtained with the inverse of the original matrix from perturbed powers, (W/m^2).

We'' Radiant emittance value obtained with the stabilized matrix from perturbed powers, (W/m^2).

$We^{(1)}$ Radiant emittance value obtained with the stabilized matrix from exact powers, (W/m^2).

$\overline{We}_k$ Defined by P_j/Σ_j for $j = k$, that is, for the region whose kth value equals j

$$\overline{We}_k = \overline{We}_j = P_j/\Sigma_j \ .$$

ΔWe Difference between the We values of the two sub-regions into which a region has been split to investigate inhomogeneity.

δWe Uncertainty in the value of We obtained with the original matrix, (W/m^2).

$\delta We'$ Uncertainty in the value of $We^{(1)}$ obtained with the stabilized matrix from exact powers, (W/m^2).

$\delta We''$ Uncertainty in the value of We'' obtained with the stabilized matrix from perturbed powers, (W/m^2).

Wro Radiant reflectance for solar zenith angle equal to zero, Wr(0). It has a uniform value throughout a region, (W/m^2).

Wro' Radiant reflectance value obtained with the inverse of the original matrix from perturbed powers, (W/m^2).

Wro'' Radiant reflectance value obtained with the stabilized matrix from perturbed powers, (W/m^2).

$Wro^{(1)}$ Radiant reflectance value obtained with the stabilized matrix from exact powers, (W/m^2).

$Wr(\zeta)$	Radiant reflectance for solar zenith angle equal to ζ, (W/m^2).
$\langle Wr(\zeta)\rangle_k$	Weighted average of $Wr(\zeta)$ within the kth region and given by $S_k\ Wro_k/St_k$, (W/m^2).
$\langle Wr''(\zeta)\rangle_k$	Defined by $S_k\ Wro''_k/St_k$, (W/m^2).
δWro	Uncertainty in the value of Wro' obtained with the original matrix, (W/m^2).
$\delta Wro'$	Uncertainty in the value of $Wro^{(1)}$ obtained with the stabilized matrix from exact powers, (W/m^2).
$\delta Wro''$	Uncertainty in the value of Wro" obtained with the stabilized matrix from perturbed powers, (W/m^2).
$\delta Wr''(\zeta)$	Uncertainty in the value of $\langle Wr''(\zeta)\rangle$.
WFOV	Wide field of view.
ζ	Zenith angle of the sun at the ΔA considered.